# Development of Passive and Active Integrated Silicon Nitride Photonics

Ontwikkeling van passieve en actieve geïntegreerde fotonische structuren in silicumnitride

Weiqiang Xie

Promotoren: prof. dr. ir. D. Van Thourhout, prof. dr. ir. Z. Hens
Proefschrift ingediend tot het behalen van de graad van
Doctor in de ingenieurswetenschappen: fotonica

Vakgroep Informatietechnologie
Voorzitter: prof. dr. ir. D. De Zutter
Faculteit Ingenieurswetenschappen en Architectuur

Vakgroep Anorganische en Fysische Chemie
Voorzitter: prof. dr. I. Van Driessche
Faculteit Wetenschappen

UNIVERSITEIT
GENT

Academiejaar 2016 - 2017

ISBN 978-90-8578-941-3
NUR 965, 971
Wettelijk depot: D/2016/10.500/73

Universiteit Gent
Faculteit Ingenieurswetenschappen en Architectuur
Vakgroep Informatietechnologie

**Promotor:**

Prof. dr. ir. Dries Van Thourhout
Prof. dr. ir. Zeger Hens

**Examencommissie:**

| | |
|---|---|
| Prof. dr. ir. Patrick De Baets (voorzitter) | Universiteit Gent |
| Prof. dr. ir. Dries Van Thourhout (Promotor) | Universiteit Gent |
| Prof. dr. ir. Zeger Hens (Promotor) | Universiteit Gent |
| Prof. dr. ir. Roel Baets | Universiteit Gent |
| Prof. dr. ir. Kristiaan Neyts | Universiteit Gent |
| Prof. dr. ir. Sonia García Blanco | Twente University |
| Dr. ir. Thilo Stöferle | IBM Research in Zurich |

Universiteit Gent
Faculteit Ingenieurswetenschappen en Architectuur

Vakgroep Informatietechnologie
Technologiepark-Zwijnaarde 15, B-9052 Gent, België

Tel.: +32-9-264.33.30
Fax.: +32-9-331.35.93

Proefschrift tot het bekomen van de graad van
Doctor in de ingenieurswetenschappen: fotonica
Academiejaar 2016-2017

# Dankwoord

Pursing a PhD degree is one of the most important choices in my life, which will definitely exercise lasting influence on my future career. The path towards the degree is full of ups and downs. The ambitious blueprint drafted in the beginning of the PhD is always invigorating, yet it often boils down to mundane or even boring daily tasks of repeating experiments, writing progress reports, convincing your colleagues and editors of the significance of your work. It is more than often that we have to live up with inexplicable results, impossible outcomes and uncertain directions, which all result in fading enthusiasm and wobbling faith in research. Fortunately, with the support from my promoters, colleagues, friends, and family, I have finally been through this rough road. I am extremely grateful to all your help and encouragement.

Firstly, I would like to thank my supervisor, Prof. Dries Van Thourhout, for providing me with the opportunity to work on integrated photonics in the Photonics Research Group. Without his continuous guidance and stimulating discussions, I could have hardly leapt over the hurdles lying on the difficult path to the PhD. I am so impressed by his insight in integrated photonics from academia to industry, which is of great value on my future career beyond the PhD. Moreover, he is not only an excellent mentor but also a wonderful friend always sharing his curiosities and ideas about interesting areas. I am always encouraged to try out these new ideas and I especially appreciate such freedom in my research. It is my great pleasure to work with him.

I would also like to express my gratitude to my supervisor, Prof. Zeger Hens, from the group of Physics and Chemistry of Nanostructures in Ghent University, for his inspiring discussions and encouragements. His rich knowledge in nanomaterials and chemistry has enlightened me on many problems in experiment and is precious to my work. I would also like to express my thanks to my collaborators Prof. Edouard Brainis from the group of Physics and Chemistry of Nanostructures, and Dr. Thilo Stöferle, Dr. Gabriele Rainò, and Dr. Rainer F. Mahrt, from IBM Research in Zurich, for all their helpful discussions and support in measurement. I really enjoyed the two-week stay in Zurich where my disk laser has been proven to function. Frankly, I was astonished by Thilo's fantastic setup as well as his deep understanding of physics.

My special thanks go to the jury members of my PhD defense, Prof. Roel Baets, Prof. Kristiaan Neyts, Prof. Sonia García Blanco, and Dr. Thilo Stöferle, for their careful review of my thesis and insightful comments and questions.

As cleanroom life constitutes the majority of my PhD work, I want to express my sincere appreciation to Katarzyna Komorowska, Liesbet Van Landschoot, and Steven Verstuyft, for their hands-on instruction on cleanroom processing in the initial phase of my PhD. It is quite impressive that Steven can always come up with quick and efficient solutions to all problems in cleanroom.

I am very happy to work in this group with you all, and I would like to acknowledge the help from Prof. Roel Baets, Prof. Wim Bogaerts, Prof. Peter Bienstman, Prof. Geert Morthier, Prof. Gunther Roelkens, Prof. Nicolas Le Thomas, and Prof. Bart Kuyken. I am also grateful to the supporting and administrative staff in our group, Kristien, Ilse, Ilse, Mike, Michael, Jelle, Bert, Jeroen, and Richard, for all their time and help. I owe my gratitude to my colleagues, Yanlu, Zhechao, Ananth, Bin, Ashim, Yunpeng, Pieter, Tangi, Suzanne, Martin, Shankar, Cristina, Thijs, Muhammad, Haolan, Lianyan, Yingtao, Qiangsheng, for their help and fruitful discussions.

I wish to thank Yanlu, Zhechao, Bin, Chen, Yunpeng, Haolan, Yufei, Ang, Ruijun, and Jing. Because of you, my life in Ghent is filled with pleasure and happiness.

Lastly, I would like to thank my parents, brother and sister of my family. Your never-failing love and support are always the most important motivation and inspiration for my life.

*Ghent, October 2016*
*Weiqiang Xie*

# Table of Contents

# List of Figures

# List of Tables

# List of Acronyms

| | |
|---|---|
| **A** | |
| ASE | Amplified Spontaneous Emission |
| **C** | |
| CMOS | Complementary Metal-Oxide-Semiconductor |
| CMP | Chemical Mechanical Planarization |
| CW | Continuous-Wave |
| **E** | |
| EM | Electromagnetic |
| EBL | Electron-Beam Lithography |
| FWHM | Full-Width at Half-Maximum |
| **F** | |
| FDTD | Finite-Difference Time-Domain |
| FIB | Focused Ion Beam |
| FSR | Free Spectral Range |
| **L** | |
| LPCVD | Low-Pressure Chemical Vapor Deposition |
| LB | Langmuir-Blodgett |
| **P** | |
| PICs | Photonic Integrated Circuits |
| PR | Photoresist |
| PECVD | Plasma-Enhanced Chemical Vapor Deposition |

| | |
|---|---|
| PL | Photoluminescence |

**Q**

| | |
|---|---|
| Q | Quality factor |
| QDs | Quantum Dots |

**R**

| | |
|---|---|
| RIE | Reactive-Ion Etching |

**S**

| | |
|---|---|
| SiN | Silicon Nitride |
| SOI | Silicon on Insulator |
| SEM | Scanning Electron Microscope |

**T**

| | |
|---|---|
| TE | Transverse-Electric |
| TM | Transverse-Magnetic |
| TEM | Transmission Electron Microscope |

**W**

| | |
|---|---|
| WGMs | Whispering Gallery Modes |

# Nederlandse samenvatting –Summary in Dutch–

In geïntegreerde fotonische circuits worden fotonen geleid en gecontroleerd op een tijds en spatiale schaal in structuren met afmetingen van de orde van de golflengte. Dit vereist een geleidend medium met lage verliezen dat compatibel is met technieken voor nanofabricage. Gegeven zijn hoge brekingsindex en transparantie over een breed golflengtebereik vormt silicium nitride (SiN) daartoe een uitstekend materiaal. Het is compatibel met klassieke fabricagetechnieken gebruikt in de microelectronicawereld en laat toe om passieve optische structuren in hoge volumes en met hoge performantie te realiseren. Dit materiaal krijgt op dit moment dan ook veel aandacht. Gezien het een diëlektricum is het echter niet evident licht direct in SiN structuren te genereren. Daarom zijn inspanningen om actieve functies zoals lichtbronnen te integreren met het SiN platform van hoog wetenschappelijk en technologisch belang. Een mogelijke aanpak bestaat erin passieve SiN structuren te combineren met optisch actieve materialen gebruikmakend van hybride integratietechnieken. Een nieuw type van actieve materialen, colloïdale halfgeleider kristallen of kwantumdots (quantum dots, QDs), hebben rijke en aanpasbare optische en elektrische eigenschappen waarbij de sterke kwantumopsluiting van elektronen benut wordt. In het bijzonder beschikken ze over een breed afstembaar emissiespectrum en optische winst voor golflengtes die kunnen worden gevarieerd van het zichtbaar tot het infrarood gebruikmakend van kwantisatie en materiaalkeuze. Daarmee vormen ze een perfecte match voor SiN dat ook een breed transparantie spectrum vertoont. Daarom bieden halfgeleider QDs unieke mogelijkheden wat betreft hybride integratie met een SiN fotonisch IC platform, bv. voor de ontwikkeling van geïntegreerde lichtbronnen zoals efficiënte diodes, afstembare lasers en kwantumbronnen.

Gezien het platform vrij nieuw is, is er nog veel ruimte voor het verbeteren van de fabricagetechnologie en de ontwikkeling van hoog-performante bouwblokken zoals golfgeleiders met lage verliezen en on-chip resonatoren met hoge kwaliteitsfactor. Colloïdale QDs, die gesynthetiseerd worden in oplossing gebruikmakend van chemische technieken vertonen echter inherente verschillen met SiN waveguides, leidend tot 2 uitdagingen. Ten eerste worden fotonische circuits typisch gefabriceerd gebruikmakend van top-down processen zoals depositie, lithografie, etsen en substraatreiniging. Deze processen vereisen vaak hoge temperaturen, een hoog-reactieve plasma omgeving, organische contaminatie en mechanisch contact die elk op zich de kwaliteit van de QDs negatief kunnen beïnvloeden. Anderzijds kan de introductie van de QDs het ganse proces bemoeilijken en leiden tot minder performante fotonische componenten. Om deze problemen op te lossen is nood aan een technologieplatform dat toelaat QDs te integreren met SiN-golfgeleiders zonder kun respectieve performantie te degraderen.

Deze thesis is gewijd aan het ontwikkelen van een technologieplatform dat hoog-performante passieve SiN bouwblokken combineert met lichtbronnen gerealiseerd door de integratie van colloidale QDs in SiN resonatoren via een hybride techniek. Eerst en vooral werd een passief SiN platform ontwikkeld, gebruikmakend van planaire procestechnieken. Gebaseerd op een doorgedreven onderzoek van de benodigde processtappen – filmdepositie, lithografie en etsen – konden we golfgeleiderverliezen van ~1dB/cm demonsteren voor golflengtes variërend over het volledige gebied 600 nm tot 1360 nm, gebaseerd op lagen gedeponeerd met PECVD in een proces met lage temperatuur (120 °C en 270 °C). Gebruikmakend van dit platform ontwierpen en realiseerden we vrijstaande mikrodisk resonatoren verticaal gekoppeld naar onderliggende busgolfgeleiders. Hoge Q-factoren ($2.5\times10^5$ @ 1310 nm) en finesses (2300 @ 1310 nm) werden aangetoond zowel voor zichtbaar light als voor telecomgolflengtes. Bovendien hebben we aangetoond dat ons ontwerp en de fabricagemethodologie ook kan worden uitgevoerd met LPCVD SiN films. Dit opent een route om resonatoren met nog hogere Q-factor en nog breder transparantiegebied te realiseren. De nu gedemonstreerde devices gerealiseerd gebruikmakend van lab-based procestechnieken bieden daarom perspectief voor verdere ontwikkeling van SiN bouwblokken die kunnen gebruikt worden in diverse applicaties zoals optische interconnects, niet-lineaire optica en optomechanica.

Voor de realisatie van actieve componenten gebaseerd op colloïdale QDs is het vaak nodig die QDs precies te kunnen deponeren in een vooraf gedefinieerd patroon. Daarom hebben een versatiele techniek ontwikkeld voor het definiëren van QDs op vlakke substraten in patronen met nanoschaal afmetingen. Startend van hoge kwaliteitsfilms gedeponeerd gebruikmakend van de Langmuir-Blodget techniek en een uniek lift-off proces konden we experimenteel zulke patronen demonstreren, zelfs tot op het niveau van unieke QDs. Afmetingen tot 30 nm voor uniforme films en een yield van 40% voor single-dot patterning werden bereikt. Bovendien is een theoretisch model voorgesteld dat toelaat het experimentele proces te beschrijven en dat goede overeenkomst vertoont met de experimentele resultaten. Deze techniek opent mogelijkheden voor de studie van nieuwe devices waarbij de QDs precies gelocaliseed zijn, bv. binnen een optische caviteit. Meer in het bijzonder wordt deze techniek nu gebruikt bij de ontwikkeling van single-QD emitters.

Eens het passieve SiN-platform en de technieken voor de structurering van QDs ontwikkeld waren focusseerden we ons op hybride integratie van SiN golfgeleiders en QDs, gebruikmakend van planaire procestechnieken. Eerst en vooral demonstreerden we hybride SiN-QD golfgeleiders met lage verliezen en toonden aan dat de QD emissie behouden werd in deze structuren. Daarna ontwierpen en fabriceerden we vrijstaande hybride SiN-QD microdisks verticaal gekoppeld met onderliggende passieve golfgeleiders. Gedetailleerde karakterisatie van deze devices liet toe hun hoge performantie te demonsteren: hoge Q-factoren en grote FSR, efficiënte koppeling van de QD-emissie naar de disk modes en uiteindelijk naar de onderliggende golfgeleider.

Op de basis van al deze resultaten focusseerden we ons vervolgens op de demonstratie van on-chip QD-SiN microlasers. Eerst bestudeerden we de winst van QDs ingebed in SiN golfgeleiders. Een modale winst van meer dan 100 $cm^{-1}$ in (100/55/100 nm) SiN/QD/SiN structuren werd bekomen. Een identieke lagenstack werd dan gebruikt voor de fabricage van microdisks. Eerst toonde een kwantitatieve studie van de disk modes en hun verliezen aan dat lasing in principe mogelijk moest zijn, gezien de haalbare winst in deze stack. Wanneer we de disk pompten met een picoseconde laser konden we dan ook effectief laserwerking demonsteren, bij kamertemperatuur en met heel lage drempel (27 $\mu J \cdot cm^{-2}$ voor 7 μm diameter disk). Een uitgebreide karakterisatie van de spectrale, temporele en coherentie eigenschappen werd uitgevoerd. De resultaten tonen aan dat golflengteafstembare colloïdale QDs de basis kunnen vormen voor een versatiel SiN-golfgeleiderplatform. Dit opent perspectieven voor zowel praktische applicaties als fundamenteel onderzoek in kwantumemitters en kwantum elektrodynamica.

# English summary

The subject of integrated photonics is to miniaturize as many as possible optical functions on a chip and in essence it deals with two fundamental issues – generation of photons and their manipulation on a chip. The latter consists of transmission and control of light on a temporal and a spatial scale within wavelength-scale structures and requires a guiding medium with low loss that can be realized using nanofabrication. Silicon nitride (SiN), a complementary metal-oxide-semiconductor (CMOS) compatible material, given its high optical index and broad optical transparency, allows for high-volume integration of high-quality passive photonic components operating over a wide wavelength range and therefore is currently attracting a lot of attention. On the other hand, because of its dielectric nature it is hard to generate light in SiN and efforts to bring active functionalities such as light sources into the passive SiN platform are of high scientific and technological interest. An approach could be to combine passive SiN photonics with optically active materials through hybrid integration. As a novel type of matter, colloidal semiconductor nanocrystals or quantum dots (QDs) possess rich and adjustable optical and electrical properties due to strong quantum confinement of electrons and have been extensively studied in recent decades. In particular, they exhibit widely tunable emission spectra and more importantly optical gain at wavelengths that can be readily adjusted from infrared to visible wavelengths through size quantization and material choice, providing for a perfect match with broadband SiN photonics. Therefore, semiconductor QDs offer unique opportunities for hybrid integration with the SiN photonics platform, potentially enabling the development of integrated light sources such as low-cost and highly efficient light emitting diodes, tunable lasers, and controlled quantum emitters. In return, the combination of photonic building blocks and QDs provide a powerful tool for fundamental studies of light-matter interaction and quantum optics experiments.

As a newly emerging photonic platform, there still remains a lot of room for improvement in aspects of fabrication technology and development of high-performance building blocks such as low-loss waveguides operating over a broad wavelength range and high quality (Q) factor on-chip microresonators.

For active devices, the solution-based QDs however have inherent differences from SiN photonics in terms of materials and processing, resulting in two issues. First, photonics fabrication is usually carried out using planar top-down CMOS-like processes such as deposition, lithography, etching, and cleaning and those procedures often involve high temperature, a plasma environment, organic contamination, and mechanical contact, which would impair the quality of QDs. On the other hand, the introduction of QDs may increase the difficulty of the fabrication process and weaken the control of the qualities of photonic components. To solve all above problems, an enabling technique for integrating QDs and SiN photonics without degradation and incompatibility is required yet remains a challenge and attempts and efforts to develop it need to be undertaken.

This thesis is devoted to develop a passive integrated photonics platform in a lab environment, based on plasma-enhanced chemical vapor deposition (PECVD) SiN and furthermore to realize light sources by incorporating colloidal QDs into SiN building blocks via a hybrid integration technique.

First, a SiN photonics platform has been developed using a CMOS compatible technology. By thoroughly investigating the fabrication processes including film deposition, optical contact lithography, planarization, and in particular the dry etching of SiN, we have demonstrated waveguide losses of ~1 dB/cm for the wavelengths ranging from 600 nm to 1360 nm in PECVD SiN deposited in a relatively low-temperature process from 120 °C to 270 °C. Relying on this platform, we further designed and realized vertically waveguide-coupled free-standing SiN microdisks by using a unique design and optimized processes. High Q factors ($2.5\times10^5$ at 1310 nm) and large finesses (2300 at 1310 nm) have been achieved in these compact on-chip microresonators from the visible to telecom wavelengths. Moreover, we have demonstrated that our design scheme and fabrication technology for integrated free-standing SiN disks can be carried out also with low-pressure chemical vapor deposition (LPCVD) SiN films, thus potentially allowing for the realization of ultra-high-Q, ultra-high-finesse, and low-mode-volume integrated SiN microresonators operating over even broader spectral bands. The current in-house developed techniques for SiN processing will provide valuable and universal guidance for future development of SiN-based photonics. The demonstrated high-performance SiN-photonics building blocks can be used in various applications such as optical interconnect, nonlinear optics, optomechanics and others.

To develop active photonics devices using QDs, a patterning technique is often required for registering QDs in defined active regions. Therefore, we aimed for developing a versatile and straightforward technique of pattering solution-processible QDs on solid substrates in nanoscale and single-dot levels. Using high quality Langmuir–Blodgett deposition and a unique lift-off process, we experimentally demonstrated both nanoscale and single-dot patterning of colloidal QD-films. Feature sizes down to ~30 nm for a continuous and uniform film of QDs and a yield up to 40% for single-QD positioning have been obtained. Furthermore, a theoretical model was proposed to describe the process, which agrees well with experimental results. This patterning technique allows for further applicability in the context both of fundamental studies and development of novel on-chip optoelectronic devices using QDs, for instance, precisely and efficiently locating a single QD for optical or electrical excitation and integrating with photonic building blocks. In particular, in our own case, this technique is carried out in an ongoing effort to realize single-QD emitters whereby a single QD can be localized in photonic components for exploring on-chip single-photon emission.

Having established a SiN photonics platform and processing technique for QDs, we further created a versatile technique that enables hybrid integration of solution-processable QDs embedded within SiN photonics via CMOS-like fabrication technology and demonstrated low-loss QD-SiN waveguides with the preservation of QD emission. We designed and fabricated free-standing waveguide-coupled SiN microdisks with embedded QDs. The detailed characterization of the fabricated devices has revealed both high performance – high Q factors together with large free spectral ranges – and an efficient coupling of QD emission to disk resonance modes and eventually to the on-chip waveguide. On the basis of all previous achievements, we then aimed to demonstrate on-chip QD-SiN microlasers. First, we studied the optical gain of QDs embedded in SiN waveguide and obtained a net modal gain of more than 100 $\text{cm}^{-1}$ in a (100/55/100 nm) SiN/QD/SiN layer stack. The same layer stack was then used to fabricate microdisks coupled to bus waveguides and a quantitative analysis of the disk modes indicated the possibility of lasing with the measured optical gain. We observed lasing action in these disks pumped with picosecond laser pulse at room temperature, revealing an extremely low optical pump threshold of 27 $\mu\text{J}\cdot\text{cm}^{-2}$ in a disk with only 7 μm diameter. A comprehensive characterization covering spectroscopic, temporal and coherence properties of these ultra-compact microlasers was also performed for colloidal QD-based lasers for the first time. These results constitute a clear demonstration that wavelength-tunable, colloidal QDs can pave the way not only for versatile active SiN photonics but also for on-chip cavity quantum electrodynamics and quantum optics based on QD emitters.

In conclusion, this thesis created various usable technologies for SiN photonics and nanomaterials and successfully demonstrated high-performance SiN photonics and hybrid laser sources on it, thus opening up prospects for development of QD-based integrated optoelectronic devices in SiN photonics platform.

# 1

# Introduction

## 1.1 Introduction of research background

Playing with light, basically high-frequency electromagnetic (EM) waves, in essence deals with two fundamental issues – light generation and propagation. For low-frequency EM waves these were successfully addressed by moving free electrons in conductive matter, eventually leading to the era of electronics. In contrast, for light this largely remained unexplored until the foundations of quantum physics were defined from which we attained the required understanding of light-matter or more precisely photon-electron interactions including scattering, absorption, and emission. Later, new physics and applications associated with light appeared, with in particular optical communication technology. The latter directly resulted from the emergence of lasers and low-loss optical fibers which fulfill the fundamental requirements for generation and transmission of light.

Today, the goal of integrated photonics is to miniaturize optical functions as much as possible on a chip. To realize this, again two basic problems need to be resolved: generating and transmitting photons in a medium on chip. Furthermore, nowadays integrated photonics has been implemented in radically new applications such as information processing or sensing technology as well as for fundamental optics research in various fields such as nonlinear optics, cavity quantum electrodynamics and quantum optics, in which new light sources and more sophisticated manipulation of light are necessary, requiring high-performance photonic building blocks. Taking all of this into account, this work is devoted to develop a low-loss passive integrated photonics platform as well as light sources integrated on it.

### 1.1.1 Integrated photonics

The concept of integrated photonics was first introduced by Stewart E. Miller in 1969 [1], who outlined a proposal for a miniature form of laser beam circuitry. The idea was, no doubt, initially driven by the development of lasers. Miller's proposal, with the original purpose of providing a solution for a more stable optical system, however indicated more ambitious prospect of constructing complex integrated optical circuits which would interconnect a laser, modulator, coupler, and filter by planar waveguides using photolithographic techniques. In this way, optical functions in bulky components could potentially be realized in a single substrate, resulting in improved system stability and ultimately economical benefits. Clearly the objective of today's integrated photonics remains similar to the early concept. But more emphasis is placed on high-speed and high-capacity optical communication, on-chip interconnecting and data processing at low-power consumption. Another distinct feature of current photonic integrated circuits (PICs) is the more complex hybrid co-integration of photonics and electronics required for multiple functionalities.

As mentioned before, given an existing laser source, a material for efficiently guiding photons is a prerequisite since now we are playing with light on a planar chip instead of free space. Therefore, optical waveguides are, of course, key elements for building a photonic system. In general there are two types of planar waveguides – slab and channel waveguides, and here only the channel waveguide is under consideration due to its ability of confining light in both transverse directions and applicability for planar integration. The basic parameters and requirements for waveguides are:

1. **Propagation loss.** Like superconductivity for electrons, a low-loss optical waveguide is an eternal pursuit in the photonics community. It can not only relax the power requirements of light sources but also allow for constructing more complex building blocks with advanced functions. The losses in a line waveguide stem from three main different sources: absorption loss, modal radiation, and scattering loss due to heterogeneities. Absorption can occur in bulk matter and at interfaces between the waveguide core and its surroundings (cladding). In most cases the former is the main contribution, although absorption at

interfaces sometimes becomes important. Since it is an intrinsic property of bulk matter, absorption highly depends on wavelength. Dielectric materials, such as silicon dioxide ($SiO_2$ or silica) and silicon nitride (SiN), due to their large electronic band gap naturally exhibit transparency over a broad wavelength range ranging from the visible to the infrared (e.g., 0.4 to 2.0 μm) and hence are preferred candidates for transmitting light. Crystalline silicon (Si) with a band gap at 1.12 μm, is a promising candidate for the telecom wavelength range of 1.3 to 1.6 μm. Another loss mechanism is modal radiation in an idealized waveguide geometry, which can be determined by theory or numerical simulation, and this loss can be negligible in a well-designed waveguide structure. The last loss factor is scattering by volume and interface heterogeneities. Most waveguide materials exhibit excellent homogeneity and the volume scattering can be neglected. The scattering losses at interfaces can be due to any imperfections during waveguide formation and among them the sidewall roughness is the main factor. It is proportional to the square of the roughness size ($\sigma$), $\alpha \propto \sigma^2$ [2]. In a relatively small dimension waveguide with high optical confinement, the scattering loss can be large and a main limitation for realizing higher performance photonic devices. The reduction of this loss rests on further improvement of fabrication technology which remains challenging, especially when the dimensions of the photonic components are becoming ever smaller.

2. **Dimensions.** The critical geometrical parameters for a waveguide are its cross-sectional size and bending radius, which, to some extent, also determine the size of the final photonic chip. For a single mode integrated waveguide, these quantities are ultimately determined by the difference in optical refractive index between the waveguide core and cladding. The core with a high index can provide tight optical confinement and thus the waveguide mode can be constrained in a very small cross section with dimensions comparable to the photon wavelength in the medium. For example, in a waveguide with a rectangular cross section, the dimension ($d$) (width or height) required for single mode operation is approximately determined by $d \approx \lambda/(2\sqrt{n_1^2 - n_0^2})$, with $\lambda$ – the wavelength in vacuum, $n_1$ – the index of the core, and $n_0$ – the index of the cladding. The acceptable minimum bending radius $R_{\min}$ can be related to the waveguide dimensions as $R_{\min} \propto d^3/\lambda^2$ [3]. Clearly, a higher index for the guiding medium is critical to build more complex structures and eventually to achieve a compact and dense integration in a photonic chip, these features now being important requirements in today's photonics.

3. **Fabrication process.** A practical photonic system based on a certain waveguide platform should be realized using a fabrication technology with good repeatability and reliability. The techniques widely used in the microelectronics industry provide powerful tools for fabricating photonic devices and most photonic platforms have been achieved using these techniques. With the development of photonic research and applications, however, compared to conventional photonics there are two new trends for today's photonics: from microphotonics to nanophotonics and from optics to optoelectronics integration. In nanophotonics, first the size of photonic components is measured in a few tens to hundred nanometers and therefore more advanced lithography techniques with high resolution are required. In addition to the traditional means, new nanotechnologies are needed to achieve well-defined integration with novel functions for the targeted applications. On the other hand, modern photonics integration tends to combine photonic and electronic circuits on a single chip. Thus, the compatibility of PIC fabrication with existing electronics integration processing technology is desired for enabling high-volume and low-cost.

To fulfill above requirements for a waveguide photonic platform, both waveguide material and structural configuration should be chosen appropriately. Since Miller's proposal of integrated optics in 1969, extensive studies were undertaken on a variety of waveguide materials such as dielectric materials [4-8], deposited semiconductor films with large band gap [9], and polymers [10, 11]. Early demonstrations focused merely on waveguide loss and remained far from realizing a complex system. Among all these material options, due to its extreme low loss and high thermal stability, silica based photonic integration attracted tremendous attention and a complete passive platform has subsequently been established [12, 13]. Because of its broad band operation, silica photonics has also been considered as a platform for visible and near infrared photonic devices, for instance, the quantum circuits using ~800 nm light source [14].

Nevertheless, due to the very low index contrast between waveguide core and cladding, the waveguide cross section usually measures several micrometers, and the bending radius is typically a few millimeters, thus preventing dense integration with ultra-small footprint. Moreover, the low optical confinement in silica fundamentally inhibits the attempts to construct advanced photonic components such as high quality (Q) resonators and photonic crystal structures allowing for the versatile manipulation of photons. To enable this, the key solution is to use high index waveguide materials allowing for tight light confinement in sub-wavelength dimensions. As the most widely explored material in integrated electronics, Si offers the desired high index and exhibits low optical transmission loss at telecom wavelengths and thus can serve as the waveguide medium for photonics. More importantly, the use of Si potentially allows for monolithic integration of Si electronic and photonic circuits using mature complementary metal-oxide-semiconductor (CMOS) processing technology. However, this investigation was not carried out until 1986. The first implementation of Si as a waveguide operating at the 1.3 and 1.6 μm wavelengths consisted of a heavily doped Si substrate and a lightly doped Si guiding layer [15]. The width of the final waveguide was 10 μm. It exhibited up to 20 dB/cm loss, due to the low index contrast and large leakage loss to the substrate.

Later, the Si waveguide geometry with a thin layer of crystalline Si on top of an oxide layer − so-called silicon on insulator (SOI) − was proposed. Low optical loss was theoretically predicted for a slab-type waveguide with only 0.2 μm top Si layer and 0.5 μm buried oxide between the guiding layer and the Si substrate [16]. The slab waveguide is less useful for integration and subsequently a library of optical components based on rib waveguides in SOI has been developed [17-19]. However the single-mode rib waveguide still possessed micrometer dimension (e.g., width × height = 3 μm × 2 μm cross section and millimeters bending radius in Ref. 19). To make full use of the high index of Si, a stripe waveguide structure is needed allowing to reduce the cross-sectional dimensions to a few hundred nanometers, and the minimum bending radius to a few micrometers. The biggest limitation to achieve such waveguide was the low accuracy of the available lithography. With the help of high-resolution electron-beam lithography (EBL), various Si photonic building blocks were realized nevertheless, including low-loss waveguides [20, 21], high-Q photonic crystal cavities [22], and high-speed modulators [23]. More significant progress in Si photonics however has been made using standard CMOS processes and passive and active Si photonic components with high performance were demonstrated, including low-loss waveguides [24-28], grating couplers [29], spectral filters [30], high-Q photonic crystal cavities [31], optical modulators [32], photodetectors [33], and laser sources [34] on the Si platform. The successful implementation of CMOS technology in Si photonics paves the way toward ultra-compact and large-scale integration of Si PICs, bringing exciting benefits to practical applications particularly in optical communication, on-chip interconnection, and information processing.

Despite the great promises of Si photonics, there is still continued interest and real efforts in pursuing other materials for realizing a photonic platform as reinforcement or even replacement of the existing platforms. The momentum of this activity originates not only from the poor light-emission efficiency in Si due to its indirect band gap nature, but also from its limitation in usable wavelength range, intrinsically preventing photonic-based research and applications in the wavelength range below the Si band gap. Integrated photonics at short wavelength range, e.g., in the near infrared and visible, have gained increasing attention recently in both fundamental research and application development including nonlinear optics, quantum optics, and sensing technology. Even at telecom wavelengths, despite a low linear loss, Si actually has large nonlinear loss due to its small band gap, a fundamental limitation for applications in nonlinear optics. In addition, the current technology platform in Si photonics restricts the optical layer only to a single Si layer on a SOI substrate, making it difficult to construct multiple-layer or even three-dimensional photonic chips. Last, though mature in manufacturing, the SOI substrate is not that cost-efficient, another drawback in particular for mass application requiring low cost. Therefore, an appropriate wave-guiding material should be considered and based on it a passive and active platform can be built up. In this thesis, we will choose SiN – another CMOS-compatible material – as waveguide material and develop a low-loss passive SiN photonics platform operating from visible to infrared wavelengths by using CMOS-like processes in a lab environment. Furthermore, light sources integrated in SiN photonics will be demonstrated exploiting hybrid integration of semiconductor nanocrystals as efficient light-emitters.

### 1.1.2 Semiconductor nanocrystals

Semiconductor nanocrystals are nanometer-sized crystalline particles which comprise tens to thousands atoms. Their size ranges from ~1 nm to ~10 nm. These nanoparticles retain the lattice structure of bulk crystals but their electronic properties differ often showing a behavior intermediate between macroscopic solids and atoms. This can be attributed to the physical confinement of electrons in all three spatial dimensions, and the associated quantum confinement effects. As such these nanocrystals are also called semiconductor quantum dots (QDs). For simplicity, hereafter the term QDs will be used to refer to semiconductor QDs. When the spatial size of the solid shrinks down, the motion of electrons evolves from a free to a confined situation. This spatial confinement results in a dramatic change of the electron state density and concomitantly electronic energy quantization in QDs, compared to continuous energy bands of a bulk material, as schematically illustrated in Figure 1.1(a) and (b). For a QD with a radius of $R$, the electrons can be regarded to be placed in an infinite spherical potential well and by solving the Schrödinger equation one can obtain a set of discrete electronic energy levels that will be proportional to $R^{-2}$.

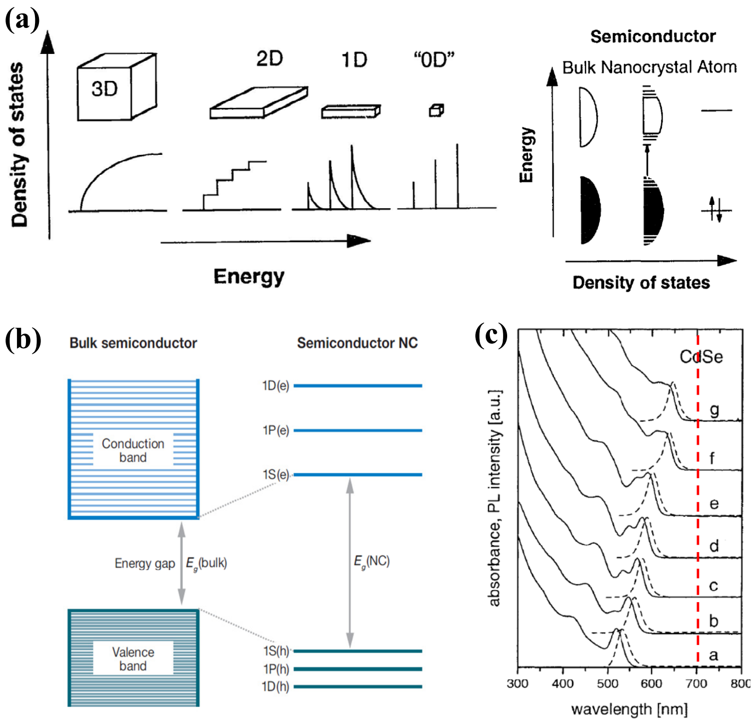

**Figure 1.1:** (a) Evolution of density of states in semiconductor as a function of dimension. Adapted from [48]. (b) Sketches of electronic structures in bulk semiconductors and QDs. Adapted from [49]. (c) Absorption (solid curves) and emission (dashed curves) spectra of CdSe QDs with increasing QD size from bottom to top. The dashed red line indicates the band gap of bulk CdSe of ~712 nm. Adapted from [50].

In real QDs, the situation is more complex. Their research began in the early 1980s initiated by Ekimov [35-39], Efros [40-43], and Brus [44-47], with the purpose of understanding the size dependence of QD optical absorption in a glass matrix or a colloidal solution. The size-dependent optical properties of QDs fundamentally arise from their electronic structure, and for this analysis, according to the ratio of QD radius $R$, to the Bohr radius $a_\mathrm{B}$ of the bulk exciton one can identify three different regimes: weak confinement in the limit $R > a_\mathrm{B}$, intermediate confinement for $R \sim a_\mathrm{B}$, and strong confinement when $R < a_\mathrm{B}$ [43]. In the strong confinement regime, if we neglect Coulomb interaction between the electron and hole, the size-dependent energy gap $E_\mathrm{g}(\mathrm{QD})$ of QDs (lowest excited electronic state) relates to the bulk semiconductor energy gap $E_g(\mathrm{bulk})$ simply as $E_\mathrm{g}(\mathrm{QD}) = E_\mathrm{g}(\mathrm{bulk}) + \hbar^2\pi^2/(2m^*R^2)$, where $1/m^* = 1/m_\mathrm{e} + 1/m_\mathrm{h}$, and $m_\mathrm{e}$ and $m_\mathrm{h}$ are the electron and hole effective masses, respectively [46]. From this expression, clearly, the band gap of a QD compared to the bulk one will blue shift and show a distinct size dependence. This has been experimentally demonstrated in absorption and emission spectra of QDs, as nicely shown in Figure 1.1(c).

Although unique electrical and optical properties were predicted theoretically in this new class of materials, for practical utilization of such tiny QDs, the possibility for preparing QDs with desired properties is a prerequisite. Generally, there are two main routes to the formation of QDs: top-down and bottom-up approaches. The latter one appears to be the mainstream in today's QD research, and mainly includes two different methods: epitaxial growth on suitable solid substrates and wet-chemical synthesis typically in solution. QDs chemically synthesized in solution are also known as colloidal nanoparticles and it is this type QDs that is employed in this thesis. However, it is not a trivial task to synthesize high-quality QDs with good control of QD composition, size, shape, monodispersity, and size distribution. A significant progress of fabrication of QDs was made by Murray *et al* who introduced a simple synthesis technique for the fabrication of high-quality II-VI semiconductor QDs through the pyrolysis of organometallic reagents in wet chemical reaction [51]. This method was applied to produce a variety of semiconductor QDs including III-V and IV-VI QDs [52]. Later, QDs with more complex shapes and various structures were achieved [53-56]. In particular, core-shell type QDs provides a level of stability that is of essential importance in biology applications [57-59]. Moreover, it allows for effective passivation of the QD surface, bringing us additional ways for engineering QD electronic structures and hence electrical and optical properties such as tuning the band gaps, improving luminescence quantum yields, and enabling efficient optical gains. Today, the availability of nanotechnology for QDs makes them appealing as platforms in nanoscience for manipulating electrons in mesoscopic scale and also as material building blocks for optoelectronic device applications [60], such as photovoltaic energy conversion [61-63], photodetectors [64, 65], light-emitting diodes [66-69], and laser sources [70-72].

As highly luminescent emitters, obviously QDs have great potential for the use in passive photonics as light-generating media. Via hybrid integration of QDs with photonic components it might be possible to develop integrated light sources, a major bottleneck in most photonic platforms. Such a hybrid approach, combining an active material with a passive platform, in fact has been widely explored in Si photonics, e.g. by means of wafer bonding techniques or through direct growing III-V semiconductors lasers on Si PICs, and various laser devices operating at telecom wavelengths have been demonstrated. In the case of SiN photonics, there are two main driving forces for the marriage of QDs with SiN PICs. First the emission and optical gain bands in QDs can be easily adjusted by size quantization and material choice within a broad spectral range covering from the visible to mid-infrared wavelengths, as shown in Figure 1.2. Such wide spectral tunability perfectly matches the broad operation window of SiN photonics. Second, the solution processability of QDs together with depositable SiN film provides flexibilities in design and fabrication, potentially allowing for integrating either an ensemble or single QDs deterministically in SiN PICs for laser or single photon emitter devices.

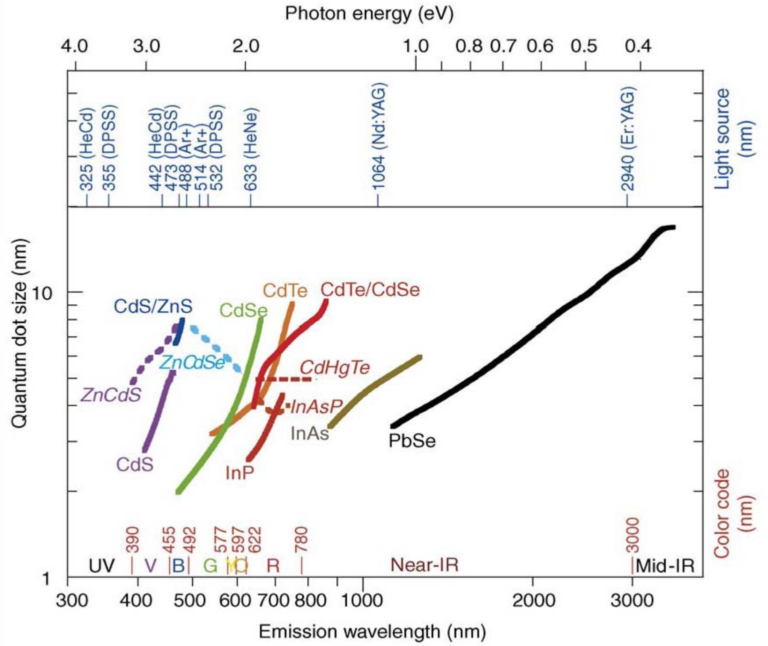

**Figure 1.2:** Size-dependent emission of QDs fabricated with various types of semiconductor materials. The bottom indicates the ranges for the various colors and the top panel indicates commonly available laser sources. Adapted from [73].

On the other hand, solution based QDs have inherent differences from SiN photonics in terms of material and processing techniques, resulting in two issues. On the one hand, photonics fabrication is usually carried out using planar top-down CMOS-like processes such as deposition, lithography, etching, and cleaning. Those procedures often involve high temperature (e.g., up to ~300 °C), a plasma environment, organic contamination, and mechanical contact, which all could impair the quality of the QDs. In return, the presence of QDs will certainly increase the difficulty of fabricating high quality integrated circuits, resulting e.g. in imperfections of the geometrical shape and increased etching roughness. To solve all above problems, an enabling technique for coherently integrating QDs and SiN photonics without degradation and incompatibility is required.

## 1.2 Definition of research objectives

Given above considerations, we defined two objectives for this thesis. First, we will develop a low-loss passive SiN photonics platform. By systematical optimization of the fabrication processes, in particular, the optical lithography and dry etching, we aim for low-loss waveguides operating from 600 nm to 1360 nm. Based on this platform, we will further design and demonstrate free-standing SiN microdisk resonators vertically coupled with on-chip waveguides aiming for high-Q and high-finesse integrated microresonators.

The second objective is the development of light sources on SiN photonics. A powerful technique for pattering QDs on a solid substrate at nanoscale or single-dot level will be first developed. This technique can in the future be used in deterministic coupling of QDs with SiN devices e.g. for the investigation of single-photon sources based on QDs. Afterwards, a hybrid integration technology will be developed for embedding QDs in SiN photonics and low-loss QD-SiN waveguides and optically active microdisks are demonstrated. Furthermore, on-chip integrated QD-SiN microdisk lasers will be investigated and demonstrated by performing comprehensive characterization for laser devices. The successes of low-loss SiN photonics and integrated QD laser sources on it will pave the way for development of QD-based integrated optoelectronic devices in SiN photonics and thus provide new opportunities for both practical applications and fundamental research.

The research is carried out in a close collaboration between the Ghent University research groups Photonics Research Group (PRG) and Physics and Chemistry of Nanostructures (PCN), which have ample expertise in respectively integrated photonic devices and the synthesis and characterization of colloidal QDs. Additionally, a collaboration with IBM Research in Zurich, Switzerland, was set up particularly on high speed device characterization.

## 1.3 Structure of thesis

In this Chapter, we reviewed the background of integrated photonics and semiconductor nanocrystals. On the basis of this, we aim for the development of a SiN passive photonics platform and propose the concept of hybrid integration of QDs with SiN photonics with the purpose of developing light sources. Both opportunities and challenges for accomplishing such integration technology were discussed. Then appropriate goals of the thesis were defined.

In Chapter 2, we will focus on the process development of a laboratory scale SiN photonics platform and the experimental demonstration of low-loss waveguides and high-Q microdisk resonators operating from visible to infrared wavelengths.

Chapter 3 deals with a pattering technique for QDs. Using an optimized lift-off process we develop a technique for both nanoscale and single-dot patterning of QD films, demonstrating feature sizes down to ~30 nm for uniform films and a yield of 40% for single-dot positioning. While first of all presenting a unique tool for studying physics of single QDs, the process also provides a pathway towards practical QD-based optoelectronic devices.

In Chapter 4, we develop a platform for the hybrid integration of SiN photonics with QDs. Based on this platform, SiN waveguides with a monolayer of embedded QDs are fabricated. Both the preservation of QD luminescence and low waveguide loss are demonstrated. This fabrication technology is further used for developing waveguide-coupled free-standing SiN microdisks hybridly integrated with embedded colloidal QDs. The detailed photoluminescence characterization of the fabricated devices reveals both high performance in disk resonators and efficient coupling of QD emission to disk resonance modes and eventually to the on-chip waveguide.

Relying on all the previous achievements, Chapter 5 aims for demonstration of lasing in a QD-SiN microdisk. Prior to this, first we study the optical gain in QD-SiN waveguides and demonstrate a high modal gain with only a ~55 nm thick QD layer. Then lasing is demonstrated in a high-Q QD-SiN microdisk under femtosecond optical pumping. A pronounced power increase and reduced lifetime of the waveguide coupled emission concurring with a spectral narrowing and enhanced temporal coherence are observed. With a lasing threshold as low as 27 $\mu J\cdot cm^{-2}$ for a 7 μm disk, these ultra-compact waveguide-coupled QD-SiN microdisks open the prospect of integrated photonics based on QDs.

Chapter 6 finally summarizes the work of this thesis and also brings forward proposals for further work.

## 1.4 Publications

### Publications in international journals

1. **W. Q. Xie**, T. Stöferle, G. Rainò, T. Aubert, S. Bisschop, Y. Zhu, R. F. Mahrt, E. Brainis, P. Geiregat, Z. Hens, and D. Van Thourhout, “On-chip integrated quantum-dot silicon-nitride microdisk lasers,” (submitted).

2. **W. Q. Xie**, Y. P. Zhu, T. Aubert, Z. Hens, E. Brainis, and D. Van Thourhout, “Fabrication and characterization of on-chip silicon nitride microdisk integrated with colloidal quantum dots,” Opt. Express **24**(2), A114-A122 (2016).

3. **W. Q. Xie**, R. Gomes, T. Aubert, S. Bisschop, Y. P. Zhu, Z. Hens, E. Brainis, and D. Van Thourhout, “Nanoscale and Single-Dot Patterning of Colloidal Quantum Dots,” Nano Lett. **15**(11), 7481-7487 (2015).
4. **W. Q. Xie**, Y. P. Zhu, T. Aubert, S. Verstuyft, Z. Hens, and D. Van Thourhout, “Low-loss silicon nitride waveguide hybridly integrated with colloidal quantum dots,” Opt. Express **23**(9), 12152-12160 (2015).
5. **W. Q. Xie**, M. Fiers, S. Selvaraja, P. Bienstman, J. Van Campenhout, P. Absil, and D. Van Thourhout, “High-Q Photonic Crystal Nanocavities on 300 mm SOI Substrate Fabricated With 193 nm Immersion Lithography,” J. Lightwave Technol. **32**(8), 1457-1462 (2014).
6. Q. S. Huang, Y. C. Wu, K. Q. Ma, J. H. Zhang, **W. Q. Xie**, X. Fu, Y. C. Shi, K. X. Chen, J. J. He, D. Van Thourhout, G. Roelkens, L. Liu, and S. L. He, “Low driving voltage band-filling-based III-V-on-silicon electroabsorption modulator,” Appl. Phys. Lett. **108**, 141104 (2016).
7. A. Z. Subramanian, E. Ryckeboer, A. Dhakal, F. Peyskens, A. Malik, B. Kuyken, H. L. Zhao, S. Pathak, A. Ruocco, A. De Groote, P. Wuytens, D. Martens, F. Leo, **W. Q. Xie**, U. D. Dave, M. Muneeb, P. Van Dorpe, J. Van Campenhout, W. Bogaerts, P. Bienstman, N. Le Thomas, D. Van Thourhout, Z. Hens, G. Roelkens, and R. Baets, “Silicon and silicon nitride photonic circuits for spectroscopic sensing on-a-chip,” Photonics Research **3**(5), B47-B59 (2015).
8. X. Fu, J. X. Cheng, Q. S. Huang, Y. T. Hu, **W. Q. Xie**, M. Tassaert, J. Verbist, K. Q. Ma, J. H. Zhang, K. X. Chen, C. Z. Zhang, Y. C. Shi, J. Bauwelinck, G. Roelkens, L. Liu, and S. L. He, “5 x 20 Gb/s heterogeneously integrated III-V on silicon electro-absorption modulator array with arrayed waveguide grating multiplexer,” Opt. Express **23**(14), 18686-18693 (2015).
9. A. Omari, **W. Q. Xie**, P. Geiregat, D. Van Thourhout, and Z. Hens, “Modeling the Optical Properties of Low-Cost Colloidal Quantum Dot Functionalized Strip SOI Waveguides,” IEEE J. Sel. Top. Quantum Electron. **20**(4) (2014).

## Publications in international conferences

1. **W. Q. Xie**, T. Stöferle, G. Rainò, T. Aubert, Y. Zhu, R. F. Mahrt, E. Brainis, Z. Hens, and D. Van Thourhout, “Integrated Silicon Nitride Microdisk Lasers Based on Quantum Dots,” 2016 Conference on Lasers and Electro-Optics (CLEO), United States, (2016). (postdeadline paper).

2. **W. Q. Xie**, Y. Zhu, T. Aubert, Z. Hens, E. Brainis, and D. Van. Thourhout, “On-chip hybrid integration of silicon nitride microdisk with colloidal quantum dots,” 12th International Conference on Group IV Photonics, Canada, 159-160 (2015).
3. **W. Q. Xie**, D. Van Thourhout, “Fabrication of high-Q silicon nitride microdisk resonator coupled with on-chip waveguide,” Proceedings of the 19th Annual Symposium of the IEEE Photonics Society Benelux Chapter, Netherlands, 145-148 (2014).
4. **W. Q. Xie** and D. Van Thourhout, “High-Q Free-standing Silicon Nitride Micordisk Vertically Coupled with On-chip Waveguide,” 2014 Conference on Lasers and Electro-Optics (CLEO), United States, (2014).
5. **W. Q. Xie**, M. Fiers, S. Selvaraja, J. Van Campenhout, P. Absil, D. Van Thourhout, “High-Q photonic crystal nanocavities on 300 mm SOI substrate fabricated by 193 nm immersion lithography,” Proceedings of the 2012 Annual Symposium of the IEEE Photonics Society Benelux Chapter, Belgium, 183-186 (2012).
6. Y. Zhu, **W. Q. Xie**, P. Geiregat, S. Bisschop, T. Aubert, Edouard Brainis, Zeger Hens, D. Van Thourhout, “Hybrid Colloidal Quantum Dot Silicon Nitride Waveguide Gain Measurement Based on Variable Stripe Length Method,” 2016 Conference on Lasers and Electro-Optics (CLEO), United States, (2016).
7. Y. Zhu, Yuqing Jiao, **W. Q. Xie**, J. Wang, B. Tian, Edouard Brainis, D. Van Thourhout, “Ultra-compact silicon nitride grating coupler for on-chip single photon source,” accepted for publication in EMRS Spring Meeting, France, (2016).
8. Y. Zhu, Yuqing Jiao, Jie Wang, **W. Q. Xie**, B. Tian, D. Van Thourhout, “Ultra-compact silicon nitride grating coupler for microscopy system,” Proceedings of the 20th Annual Symposium of the IEEE Photonics Benelux Chapter, Belgium, (2015).
9. S. Bisschop, Y. P. Zhu, **W. Q. Xie**, A. Guille, Z. Hens, D. Van Thourhout, and E. Brainis, “Progress Towards On-chip Single Photon Sources Based on Colloidal Quantum Dots in Silicon Nitride Devices,” 2014 Conference on Lasers and Electro-Optics (CLEO), United States, (2014).
10. S. K. Selvaraja, G. Winroth, S. Locorotondo, G. Murdoch, A. Milenin, C. Delvaux, P. Ong, S. Pathak, **W. Q. Xie**, G. Sterckx, G. Lepage, D. Van Thourhout, W. Bogaerts, J. Van Campenhout, and P. Absil, “193nm

immersion lithography for high performance silicon photonic circuits," Optical Microlithography XXVII **90520F** (2014).

11. Y. Zhu, **W. Q. Xie**, S. Verstuyft, Tangi Aubert, Zeger Hens, D. Van Thourhout, "Colloidal quantum dot silicon nitride platform," Proceedings of the 2013 Annual Symposium of the IEEE Photonics Society Belenux Chapter, Netherlands, 175-178 (2013).

## Publications in national conferences

1. **W. Q. Xie**, "On-chip Light Sources Based on Quantum Dots," 14th FEA PhD Symposium (2013).

# References

[1] S. E. Miller, “Integrated Optics - an Introduction,” Bell System Technical Journal **48**(7), 2059(1969).

[2] P. K. Tien, “Light Waves in Thin Films and Integrated Optics,” Appl. Opt. **10**(11), 2395(1971).

[3] E. A. J. Marcatili, “Bends in Optical Dielectric Guides,” Bell System Technical Journal **48**(7), 2103 (1969).

[4] J. E. Goell and R. D. Standley, “Sputtered Glass Waveguide for Integrated Optical Circuits,” Bell System Technical Journal **48**(10), 3445 (1969).

[5] S. Takada, M. Ohnishi, H. Hayakawa, and Mikoshib.N, “Optical-Waveguides of Single-Crystal $LiNbO_3$ Film Deposited by Rf Sputtering,” Appl. Phys. Lett. **24**(10), 490-492 (1974).

[6] P. K. Tien, “Integrated-Optics and New Wave Phenomena in Optical-Waveguides,” Rev. Mod. Phys. **49**(2), 361-420 (1977).

[7] W. Stutius and W. Streifer, “Silicon-Nitride Films on Silicon for Optical-Waveguides,” Appl. Opt. **16**(12), 3218-3222 (1977).

[8] S. Dutta, H. E. Jackson, J. T. Boyd, R. L. Davis, and F. S. Hickernell, “$CO_2$-Laser Annealing of $Si_3N_4$, $Nb_2O_5$, and $Ta_2O_5$ Thin-Film Optical-Waveguides to Achieve Scattering Loss Reduction,” IEEE J. Quantum Electron. **18**(4), 800-806 (1982).

[9] P. K. Tien, R. Ulrich, and R. J. Martin, “Modes of Propagating Light Waves in Thin Deposited Semiconductor Films,” Appl. Phys. Lett. **14**(9), 291(1969).

[10] J. T. Boyd and C. L. Chen, “Integrated Optical Silicon Photodiode Array,” Appl. Opt. **15**(6), 1389-1393 (1976).

[11] H. Ma, A. K. Y. Jen, and L. R. Dalton, “Polymer-based optical waveguides: Materials, processing, and devices,” Adv. Mater. **14**(19), 1339-1365 (2002).

[12] N. Takato, K. Jinguji, M. Yasu, H. Toba, and M. Kawachi, “Silica-based single-mode waveguides on silicon and their application to guided-wave optical interferometers,” J. Lightwave Technol. **6**(6), 1003-1010 (1988).

[13] M. Kawachi, “Silica waveguides on silicon and their application to integrated-optic components,” Opt. Quantum Electron. **22**(5), 391-416 (1990).

[14] A. Politi, M. J. Cryan, J. G. Rarity, S. Y. Yu, and J. L. O'Brien, “Silica-on-silicon waveguide quantum circuits,” Science **320**(5876), 646-649 (2008).

[15] R. A. Soref and J. P. Lorenzo, “All-Silicon Active and Passive Guided-Wave Components for λ=1.3 and 1.6 μm,” IEEE J. Quantum Electron. **22**(6), 873-879 (1986).

[16] B. N. Kurdi and D. G. Hall, “Optical waveguides in oxygen-implanted buried-oxide silicon-on-insulator structures,” Opt. Lett. **13**(2), 175-177 (1988).

[17] R. A. Soref, J. Schmidtchen, and K. Petermann, “Large single-mode rib waveguides in GeSi-Si and Si-on-$SiO_2$,” IEEE J. Quantum Electron. **27**(8), 1971-1974 (1991).

[18] J. Schmidtchen, A. Splett, B. Schüppert, K. Petermann, and G. Burbach, “Low loss singlemode optical waveguides with large cross-section in silicon-on-insulator,” Electron. Lett **27**(16), 1486-1488 (1991).

[19] B. Jalali, P. D. Trinh, S. Yegnanarayanan, and F. Coppinger, “Guided-wave optics in silicon-on-insulator technology,” IEE Proceedings-Optoelectronics **143**(5), 307-311 (1996).

[20] S. J. McNab, N. Moll, and Y. A. Vlasov, “Ultra-low loss photonic integrated circuit with membrane-type photonic crystal waveguides,” Opt. Express **11**(22), 2927-2939 (2003).

[21] Y. A. Vlasov and S. J. McNab, “Losses in single-mode silicon-on-insulator strip waveguides and bends,” Opt. Express **12**(8), 1622-1631 (2004).

[22] Y. Akahane, T. Asano, B. S. Song, and S. Noda, “High-Q photonic nanocavity in a two-dimensional photonic crystal,” Nature **425**(6961), 944-947 (2003)

[23] Q. F. Xu, B. Schmidt, S. Pradhan, and M. Lipson, “Micrometre-scale silicon electro-optic modulator,” Nature **435**(7040), 325-327 (2005).

[24] K. K. Lee, D. R. Lim, L. C. Kimerling, J. Shin, and F. Cerrina, “Fabrication of ultralow-loss Si/SiO2 waveguides by roughness reduction,” Opt. Lett. **26**(23), 1888-1890 (2001).

[25] W. Bogaerts, V. Wiaux, D. Taillaert, S. Beckx, B. Luyssaert, P. Bienstman, and R. Baets, “Fabrication of photonic crystals in silicon-on-insulator using 248-nm deep UV lithography,” IEEE J. Sel. Top. Quantum Electron. **8**(4), 928-934 (2002).

[26] W. Bogaerts, R. Baets, P. Dumon, V. Wiaux, S. Beckx, D. Taillaert, B. Luyssaert, J. Van Campenhout, P. Bienstman, and D. Van Thourhout,

"Nanophotonic waveguides in silicon-on-insulator fabricated with CMOS technology," J. Lightwave Technol. **23**(1), 401-412 (2005).

[27] P. Dumon, W. Bogaerts, V. Wiaux, J. Wouters, S. Beckx, J. Van Campenhout, D. Taillaert, B. Luyssaert, P. Bienstman, D. Van Thourhout, and R. Baets, "Low-loss SOI photonic wires and ring resonators fabricated with deep UV lithography," IEEE Photonics Technol. Lett. **16**(5), 1328-1330 (2004).

[28] S. K. Selvaraja, G. Winroth, S. Locorotondo, G. Murdoch, A. Milenin, C. Delvaux, P. Ong, S. Pathak, W. Q. Xie, G. Sterckx, G. Lepage, D. Van Thourhout, W. Bogaerts, J. Van Campenhout, and P. Absil, "193nm immersion lithography for high performance silicon photonic circuits," Optical Microlithography XXVII **90520F**(2014).

[29] D. Taillaert, W. Bogaerts, P. Bienstman, T. F. Krauss, P. Van Daele, I. Moerman, S. Verstuyft, K. De Mesel, and R. Baets, "An out-of-plane grating coupler for efficient butt-coupling between compact planar waveguides and single-mode fibers," IEEE J. Quantum Electron. **38**(7), 949-955 (2002).

[30] W. Bogaerts, S. K. Selvaraja, P. Dumon, J. Brouckaert, K. De Vos, D. Van Thourhout, and R. Baets, "Silicon-on-Insulator Spectral Filters Fabricated With CMOS Technology," IEEE J. Sel. Top. Quantum Electron. **16**(1), 33-44 (2010).

[31] W. Q. Xie, M. Fiers, S. Selvaraja, P. Bienstman, J. Van Campenhout, P. Absil, and D. Van Thourhout, "High-Q Photonic Crystal Nanocavities on 300 mm SOI Substrate Fabricated With 193 nm Immersion Lithography," J. Lightwave Technol. **32**(8), 1457-1462 (2014).

[32] A. S. Liu, R. Jones, L. Liao, D. Samara-Rubio, D. Rubin, O. Cohen, R. Nicolaescu, and M. Paniccia, "A high-speed silicon optical modulator based on a metal-oxide-semiconductor capacitor," Nature **427**(6975), 615-618 (2004).

[33] D. Ahn, C. Y. Hong, J. F. Liu, W. Giziewicz, M. Beals, L. C. Kimerling, J. Michel, J. Chen, and F. X. Kartner, "High performance, waveguide integrated Ge photodetectors," Opt. Express **15**(7), 3916-3921 (2007).

[34] D. Liang and J. E. Bowers, "Recent progress in lasers on silicon," Nat. Photonics **4**(8), 511-517 (2010).

[35] A. I. Ekimov and A. A. Onushchenko, "Quantum Size Effect in 3-Dimensional Microscopic Semiconductor Crystals," JETP Lett. **34**(6), 345-349 (1981).

[36] A. I. Ekimov and A. A. Onushchenko, “Quantum Size Effect in the Optical-Spectra of Semiconductor Micro-Crystals,” Soviet Physics Semiconductors-Ussr **16**(7), 775-778 (1982).

[37] A. I. Ekimov, A. L. Efros, and A. A. Onushchenko, “Quantum Size Effect in Semiconductor Microcrystals,” Solid State Commun. **56**(11), 921-924 (1985).

[38] A. I. Ekimov, “Optical-Properties of Semiconductor Quantum Dots in Glass Matrix,” Phys. Scr. **T39**, 217-222 (1991).

[39] A. I. Ekimov, F. Hache, M. C. Schanneklein, D. Ricard, C. Flytzanis, I. A. Kudryavtsev, T. V. Yazeva, A. V. Rodina, and A. L. Efros, “Absorption and Intensity-Dependent Photoluminescence Measurements on Cdse Quantum Dots - Assignment of the 1st Electronic-Transitions,” Journal of the Optical Society of America B-Optical Physics **10**(1), 100-107 (1993).

[40] A. L. Efros and A. L. Efros, “Interband Absorption of Light in a Semiconductor Sphere,” Soviet Physics Semiconductors-Ussr **16**(7), 772-775 (1982).

[41] A. L. Efros, V. A. Kharchenko, and M. Rosen, “Breaking the Phonon Bottleneck in Nanometer Quantum Dots - Role of Auger-Like Processes,” Solid State Commun. **93**(4), 281-284 (1995).

[42] A. L. Efros, M. Rosen, M. Kuno, M. Nirmal, D. J. Norris, and M. Bawendi, “Band-edge exciton in quantum dots of semiconductors with a degenerate valence band: Dark and bright exciton states,” Phys. Rev. B **54**(7), 4843-4856 (1996).

[43] A. L. Efros and M. Rosen, “The electronic structure of semiconductor nanocrystals,” Annu. Rev. Mater. Sci. **30**, 475-521 (2000).

[44] L. E. Brus, “A Simple-Model for the Ionization-Potential, Electron-Affinity, and Aqueous Redox Potentials of Small Semiconductor Crystallites,” J. Chem. Phys. **79**(11), 5566-5571 (1983).

[45] R. Rossetti, S. Nakahara, and L. E. Brus, “Quantum Size Effects in the Redox Potentials, Resonance Raman-Spectra, and Electronic-Spectra of Cds Crystallites in Aqueous-Solution,” J. Chem. Phys. **79**(2), 1086-1088 (1983).

[46] L. E. Brus, “Electron Electron and Electron-Hole Interactions in Small Semiconductor Crystallites - the Size Dependence of the Lowest Excited Electronic State,” J. Chem. Phys. **80**(9), 4403-4409 (1984).

[47] M. G. Bawendi, M. L. Steigerwald, and L. E. Brus, “The Quantum-Mechanics of Larger Semiconductor Clusters (Quantum Dots),” Annu. Rev. Phys. Chem. **41**, 477-496 (1990).

[48] A. P. Alivisatos, “Semiconductor clusters, nanocrystals, and quantum dots,” Science **271**(5251), 933-937 (1996).

[49] V. I. Klimov, “Spectral and dynamical properties of multilexcitons in semiconductor nanocrystals,” Annu. Rev. Phys. Chem. **58**, 635-673 (2007).

[50] D. V. Talapin, A. L. Rogach, A. Kornowski, M. Haase, and H. Weller, “Highly luminescent monodisperse CdSe and CdSe/ZnS nanocrystals synthesized in a hexadecylamine-trioctylphosphine oxide-trioctylphospine mixture,” Nano Lett. **1**(4), 207-211 (2001).

[51] C. B. Murray, D. J. Norris, and M. G. Bawendi, “Synthesis and Characterization of Nearly Monodisperse Cde (E = S, Se, Te) Semiconductor Nanocrystallites,” J. Am. Chem. Soc. **115**(19), 8706-8715 (1993).

[52] G. Schmid, ed. *Nanoparticles: from theory to application* (John Wiley & Sons, 2011).

[53] L. Manna, E. C. Scher, and A. P. Alivisatos, “Synthesis of soluble and processable rod-, arrow-, teardrop-, and tetrapod-shaped CdSe nanocrystals,” J. Am. Chem. Soc. **122**(51), 12700-12706 (2000).

[54] M. A. Hines and P. Guyot-Sionnest, “Synthesis and characterization of strongly luminescing ZnS-Capped CdSe nanocrystals,” J. Phys. Chem. **100**(2), 468-471 (1996).

[55] B. O. Dabbousi, J. Rodriguez-Viejo, F. V. Mikulec, J. R. Heine, H. Mattoussi, R. Ober, K. F. Jensen, and M. G. Bawendi, “(CdSe)ZnS Core−Shell Quantum Dots: Synthesis and Characterization of a Size Series of Highly Luminescent Nanocrystallites,” The Journal of Physical Chemistry B **101**(46), 9463-9475 (1997).

[56] X. G. Peng, M. C. Schlamp, A. V. Kadavanich, and A. P. Alivisatos, “Epitaxial growth of highly luminescent CdSe/CdS core/shell nanocrystals with photostability and electronic accessibility,” J. Am. Chem. Soc. **119**(30), 7019-7029 (1997).

[57] M. Bruchez, M. Moronne, P. Gin, S. Weiss, and A. P. Alivisatos, “Semiconductor nanocrystals as fluorescent biological labels,” Science **281**(5385), 2013-2016 (1998).

[58] I. L. Medintz, H. T. Uyeda, E. R. Goldman, and H. Mattoussi, “Quantum dot bioconjugates for imaging, labelling and sensing,” Nat. Mater. **4**(6), 435-446 (2005)..

[59] X. Michalet, F. F. Pinaud, L. A. Bentolila, J. M. Tsay, S. Doose, J. J. Li, G. Sundaresan, A. M. Wu, S. S. Gambhir, and S. Weiss, "Quantum dots for live cells, in vivo imaging, and diagnostics," Science **307**(5709), 538-544 (2005).

[60] D. V. Talapin, J. S. Lee, M. V. Kovalenko, and E. V. Shevchenko, "Prospects of Colloidal Nanocrystals for Electronic and Optoelectronic Applications," Chem. Rev. **110**(1), 389-458 (2010).

[61] A. J. Nozik, "Quantum dot solar cells," Physica E-Low-Dimensional Systems & Nanostructures **14**(1-2), 115-120 (2002).

[62] R. D. Schaller and V. I. Klimov, "High efficiency carrier multiplication in PbSe nanocrystals: Implications for solar energy conversion," Phys. Rev. Lett. **92**(18)(2004).

[63] P. V. Kamat, "Quantum Dot Solar Cells. Semiconductor Nanocrystals as Light Harvesters," J. Phys. Chem. C **112**(48), 18737-18753 (2008).

[64] S. A. McDonald, G. Konstantatos, S. G. Zhang, P. W. Cyr, E. J. D. Klem, L. Levina, and E. H. Sargent, "Solution-processed PbS quantum dot infrared photodetectors and photovoltaics," Nat. Mater. **4**(2), 138-142 (2005).

[65] G. Konstantatos, I. Howard, A. Fischer, S. Hoogland, J. Clifford, E. Klem, L. Levina, and E. H. Sargent, "Ultrasensitive solution-cast quantum dot photodetectors," Nature **442**(7099), 180-183 (2006).

[66] J. M. Caruge, J. E. Halpert, V. Wood, V. Bulovic, and M. G. Bawendi, "Colloidal quantum-dot light-emitting diodes with metal-oxide charge transport layers," Nat. Photonics **2**(4), 247-250 (2008).

[67] B. S. Mashford, M. Stevenson, Z. Popovic, C. Hamilton, Z. Q. Zhou, C. Breen, J. Steckel, V. Bulovic, M. Bawendi, S. Coe-Sullivan, and P. T. Kazlas, "High-efficiency quantum-dot light-emitting devices with enhanced charge injection," Nat. Photonics **7**(5), 407-412 (2013).

[68] Y. Shirasaki, G. J. Supran, M. G. Bawendi, and V. Bulovic, "Emergence of colloidal quantum-dot light-emitting technologies," Nat. Photonics **7**(1), 13-23 (2013).

[69] X. L. Dai, Z. X. Zhang, Y. Z. Jin, Y. Niu, H. J. Cao, X. Y. Liang, L. W. Chen, J. P. Wang, and X. G. Peng, "Solution-processed, high-performance light-emitting diodes based on quantum dots," Nature **515**(7525), 96-99 (2014).

[70] V. I. Klimov, A. A. Mikhailovsky, S. Xu, A. Malko, J. A. Hollingsworth, C. A. Leatherdale, H. J. Eisler, and M. G. Bawendi, "Optical gain and

stimulated emission in nanocrystal quantum dots," Science **290**(5490), 314-317 (2000).

[71] H. J. Eisler, V. C. Sundar, M. G. Bawendi, M. Walsh, H. I. Smith, and V. Klimov, "Color-selective semiconductor nanocrystal laser," Appl. Phys. Lett. **80**(24), 4614-4616 (2002).

[72] A. L. Efros, D. J. Lockwood, and L. Tsybeskov, eds. *Semiconductor nanocrystals: from basic principles to applications* (Springer Science & Business Media, 2013).

[73] S. K. Shin, H. J. Yoon, Y. J. Jung, and J. W. Park, "Nanoscale controlled self-assembled monolayers and quantum dots," Curr. Opin. Chem. Biol. **10**(5), 423-429 (2006).

# 2

# Development of passive SiN photonics

## 2.1 Silicon nitride integrated photonics

Silicon nitride (SiN), a dielectric materal with a large band gap of ~5 eV [1], exhibits transparency from the visible to the infrared. Compared with silica it has a fairly high optical index of ~2.0 [2] and allows making low-loss waveguides over a broad wavelength range while permitting a reasonable level of integration density. More importantly, SiN has been widely used in the microelectronics industry and well developed techniques for SiN material preparation and processing are available. This compatibility with complementary metal-oxide-semiconductor (CMOS) technology potentially allows for large-scale integration and cost efficiency. Hence SiN could be a promising candidate for building an integrated photonics platform. Before continuing, it is worth mentioning the methods for preparing SiN. There are several ways for the preparation of SiN [3] and the most extensively used technologies are plasma-enhanced chemical vapor deposition (PECVD) and low-pressure chemical vapor deposition (LPCVD), with both deposited SiN films amorphous in nature. Note that CVD-based techniques can produce nitride films with composition ranging from silicon nitride to silicon oxynitrides and with optical index varying from ~1.5 to 2.0 and that here we restrict our attention only to silicon nitride. LPCVD can deposit nearly stoichiometric nitride ($Si_3N_4$) with high purity and normally involves high temperatures (~700–900 °C) with a slow growth rate of 1–10 nm/min [4]. In addition, LPCVD SiN films typically exhibit high tensile stress limiting the film thickness to 400 nm if cracks need to be avoided. For thicker films multiple depositions in sequence are needed. PECVD on the other hand can be performed at relatively low temperatures (less than 500 °C), gives faster deposition rate and allows for large film thickness (up to 1 μm) in a single run [3]. With respect to optical properties, SiN formed by both methods always contains a certain amount of hydrogen bonded to silicon (Si-H) and nitrogen (N-H) [5-10] and these bonds lead to considerable absorption in the infrared. Particularly there is a prominent absorption peak around 1520 nm due to the second overtone absorption of the N-H stretching vibration [11-14]. Especially, SiN prepared by PECVD at relatively low temperatures has much higher hydrogen concentration (over one order of magnitude) than LPCVD SiN and hence exhibits higher optical loss around the 1550 nm telecom wavelength [9, 13]. The hydrogen content in both types of SiN can be minimized by optimizing the deposition conditions [9]. On the other hand, it can also be substantially reduced by an annealing process at a higher temperature (above 1000 °C) [9-14]. Nonetheless for PECVD SiN there appears to be a lower bound for the material loss around 1550 nm in the order of 1.0 dB/cm [13, 15]. For LPCVD SiN on the other hand a loss as low as 0.01 dB/cm [16, 17] has been reported.

The early work exploiting SiN as a light guiding medium focused on the visible and demonstrated losses of 0.1 dB/cm for LPCVD [18, 19] and 1.14 dB/cm for PECVD [20] at 632.8 nm in SiN slab waveguides with a $SiO_2$ buffer layer as optical insulator deposited on a Si wafer. Then a LPCVD SiN rib waveguide was fabricated via wet etching by Henry et al. who demonstrated waveguide losses less than 0.3 dB/cm in the 1.3–1.6 μm range after an annealing procedure [11]. The material loss of the PECVD SiN from visible to infrared was also examined and revealed losses of 0.1–0.3 dB/cm in the 0.63–1.35 μm wavelength range. In the 1.4–1.6 μm range higher losses were measured which subsequently could be decreased to 0.6 dB/cm by annealing out hydrogen [13].

In the field of integrated photonics, SiN has received growing attention over the past decade. Low-loss (~0.1 dB/cm) channel waveguides with a thin core layer (150–200 nm) of LPCVD SiN and large lateral dimensions (4–18 μm) fabricated via CMOS techniques have been realized in the visible [21, 22]. In the telecom wavelength range, waveguide structures with a multi-layer SiN core [23] or buried in a thick oxide cladding [24] have been investigated and a loss of 0.1 dB/cm was achieved at 1550 nm. In particular, low-confinement waveguides of ultra-low loss with TriPleX$^{TM}$ technology [16, 25] have been demonstrated and state-of-the-art waveguide losses of ~$10^{-3}$ dB/cm were reported [26, 27]. High-confinement strip waveguides with very low losses have recently been demonstrated [17, 28]. For PECVD SiN, a great effort has also been undertaken for the development of low-loss waveguides from the visible to the infrared [15, 29]. In particular, SiN photonic integrated circuits (PICs) with high performance have been accomplished completely within a CMOS pilot line [30, 31] and this platform has been proposed as a solution for multi-layer photonics, for instance back-end integration [32]. Apart from waveguide platform development, a variety of fundamental studies and applications based on SiN photonics have been undertaken. This includes the demonstration of integrated high quality (Q) resonators [17, 33-40], nonlinear optics [41-45], optomechanics [46-48], optical interconnect and communication [49, 50], and on-chip optical sensing [51-53].

As a newly emerging photonics platform, it is believed that there still remains a lot of room for improvement in aspects of fabrication technology and development of high performance building blocks like high-Q resonators and even light sources. In this chapter, relying on an optimized etching process, we will independently establish a low-loss SiN platform working from 600 nm to 1360 nm relying on a low temperature PECVD process and standard contact mask lithography. Then waveguide-coupled free-standing microdisk resonators with compact size and high-Q will be realized. These technologies form the base for later development of active SiN devices and undoubtedly provide valuable and universal guidance for future investigation on SiN photonics.

## 2.2 Fabrication technologies

The SiN photonic components are fabricated on silicon wafers with a 3 μm thermal $SiO_2$ box layer to isolate optical modes from the bottom silicon substrate. All fabrication is carried out using planar processes running on conventional fabrication tools in our clean room, including deposition, patterning, etching, and planarization. Since the performance of a photonic device is very sensitive to geometry, especially when the feature size of the structure is reduced to a few hundred nanometers, stringent dimensional is critical and fabrication with very high accuracy and reproducibility is desired to minimize the discrepancy between designed and resulting devices. Therefore, optimization of all processes is necessary. In this section, we introduce the main fabrication technologies developed leading to optimized procedures for patterning and etching of SiN photonic devices.

## Deposition

The SiN films are deposited in an Advanced Vacuum Vision 310 PECVD tool equipped with different RF frequency sources: a 13.56 MHz high frequency (H-f) and a 100–460 kHz low frequency (L-f) source. Thus the system can be operated in three modes: H-f, L-f, and mixed frequency (M-f). The temperature of the chamber plate can be varied from 120–270 °C. A gas mixture of $SiH_4$, $NH_3$, and $N_2$ is used to generate reactive plasma species and the gas ratio is optimized to realize SiN films with refractive index close to 2.0. The RF power and chamber pressure are fixed at medium levels to maintain a moderate deposition rate of 10–15 nm/min. SiN films deposited at both H-f and L-f (~100 kHz) and at temperatures of 120 °C and 270 °C are investigated for waveguide fabrication. In addition to SiN, the same system is also used to deposit $SiO_2$ and amorphous Si (aSi) in the disk fabrication process.

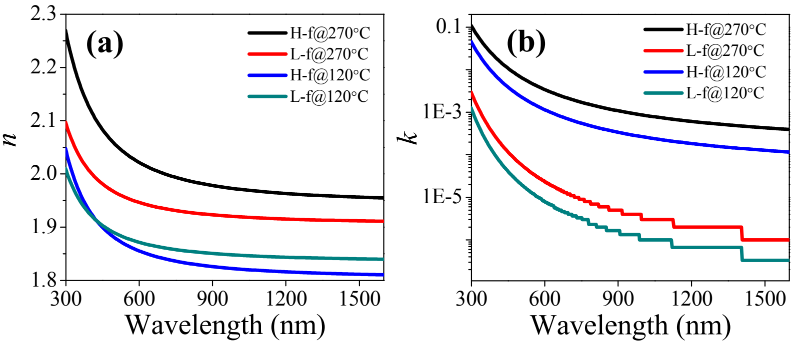

**Figure 2.1:** (a) Measured refractive indices *n* of SiN films deposited under different conditions. (b) The extinction coefficients *k*.

Figure 2.1 shows the complex refractive indices of different SiN films measured by ellipsometry. In Figure 2.1(a), it is clear that the high-temperature SiN has higher index than the low-temperature SiN. For instance, the index of H-f SiN changes from 1.978 to 1.826 with decreasing the temperature from 270 °C to 120 °C, indicating a reduction in the material density probably due to higher hydrogen content. Compared to the deposition temperature, the RF frequency only has a small effect on the index. On the contrary, from Figure 2.1(b) the RF frequency has a dramatic effect on the extinction coefficient with values for L-f SiN over two orders of magnitude lower than for H-f SiN, implying higher optical loss in H-f SiN films. Note that the absorption in the infrared due to hydrogen bonds is not reflected in the extinction coefficient curves of Figure 2.1b since Cauchy models were used for fitting the data. Therefore, we fabricated waveguides with all these SiN films and examined the losses to find the best material for photonics.

## Pattering

Patterning is the process of defining the designed image on a substrate and subsequently transferring this image on the substrate by deposition, etching, etc. Several techniques have been invented for patterning and among them the major one is optical lithography commonly utilized for mass fabrication in CMOS manufacturing. In this thesis, all SiN photonic structures are defined with contact lithography on a Karl Süss MA6 Mask Aligner using a 320 nm exposure source with a power density of 5.0 mW/cm$^2$. Since the patterned photoresist (PR) is further used as dry etching mask we selected AZ® MiR™ 701 as a positive resist specially designed for high-resolution lithography together with AZ® 726 (MIF) as developer. Figure 2.2 schematically shows the basic process flow for contact lithography. First, we prepare the substrate through deposition of a SiN film and apply PR on it by spin-coating. Then the sample with the PR layer is brought in contact with a photomask consisting of a patterned chrome film on a quartz plate and subsequently exposed to UV light. For a positive resist, the illuminated regions (those not blocked by the chrome film) will become soluble in a suitable solvent (developer) and then washed away after development. For negative resists the situation is opposite and in that cased unexposed areas will be dissolved.

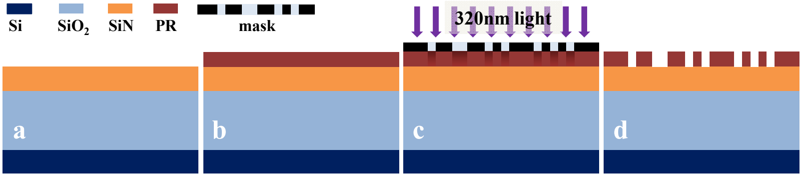

**Figure 2.2:** The lithography process flow for a positive resist. (a) Prepare substrate, (b) apply resist, (c) exposure, (d) after development.

Given its ease of operation and acceptable resolution, contact lithography is widely used for chip-scale proof-of-concept demonstrations in research where typically a several hundred-nanometer tolerance is acceptable. In the context of nanophotonics fabrication, however, the accepted fabrication imperfection should be below ten nanometers or even less for minimizing scattering losses caused by any distortion of structure. Furthermore, the ideal PR mask for dry etching exhibits steep and smooth sidewalls to ensure a vertical pattern transfer, although this requirement can be relaxed by optimizing the etch process. In Figure 2.3, we show scanning electron microscope (SEM) images of experimental results where the influence of lithography imperfections on the final structure can be clearly seen. The effect of the PR sidewall profile on the SiN pattern is illustrated in Figure 2.4. Therefore, the lithography process needs to be carefully optimized with the goal to attain a stable process with high reproducibility and good size definition as well as keeping steep sidewalls with minimal roughness. Here we strongly recommend the readers to refer to online application notes for details about lithography processes, e.g. from the resist supplier MicroChemicals [54].

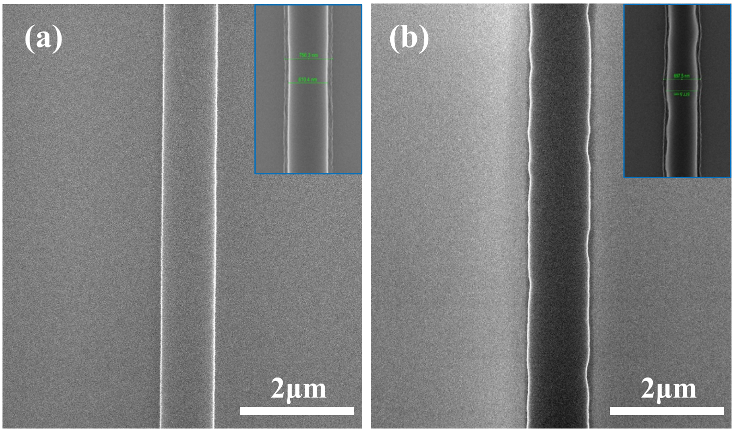

**Figure 2.3:** The etched SiN waveguide patterns with different lithography of (a) less distortion and defect and (b) clear wave-shape distortion along waveguide. The insets show associated lithography before etching.

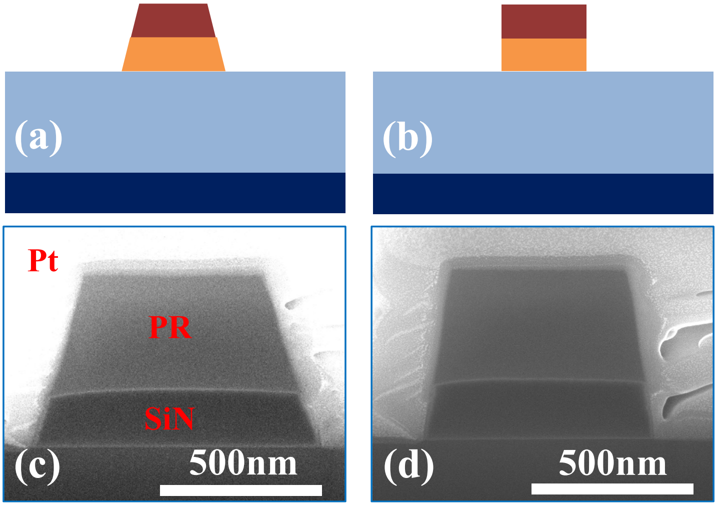

**Figure 2.4:** The effect of the PR mask on etched SiN patterns. Schematic etch results with a sloped PR sidewall (a) and with an ideally vertical sidewall (b). The real etched cross-sectional profiles under the same etching conditions but with different PR sidewall slopes in (c) and (d). The images are taken by means of focused ion beam (FIB).

The optimization of high-resolution AZ-701 resist involves various process steps including spin-coating, soft bake, exposure, post exposure bake, and development. The key is to attain a maximized contrast between development rate (dissolution rate of exposed resist in developer) and dark erosion rate (dissolution rate of unexposed resist), thus minimizing the deterioration for smallest features [54]. This dissolution contrast is mainly determined by exposure dose (i.e., exposure time) and concentration of developer, and a maximum contrast can be achieved under a moderate developer concentration and an optimum exposure dose. The latter can be obtained with an exposure-series test with a fixed developer and from the resultant dose-dependent curve the development rate (time) starts to saturate at a certain dose where the optimum exposure dose is nearby. In Figure 2.5 we show the exposure-development time curves in AZ-726 developers with different concentrations. It is obvious that development time at the beginning decreases sharply with increasing exposure time and then quickly saturates at a certain exposure time. The saturation times for development are ~14 sec at 60 sec exposure and ~55 sec at 90 sec exposure for undiluted and diluted AZ 726, respectively. Since the dark erosion grows faster than the development rate with increasing developer concentration, a moderate concentration is preferable to obtain highest dissolution selectivity. From a practical viewpoint, the diluted developer allows for a somewhat longer and easier to control development time and thus relaxes the process window. With those considerations in mind, we use ~100 sec exposure time and the developer of AZ-726 diluted with $H_2O$ at a ratio of 2:1. Additionally, the other parameters are also optimized. We summarize the optimal procedure for high-resolution AZ 701 resist under 320 nm and 5mW/cm$^2$ exposure as follows:

**a.** Clean substrate and bake at 120 °C for 3 min on hotplate
**b.** If necessary, apply adhesion promoter, e.g., TI Prime with a bake at 120 °C for 3 min on hotplate
**c.** Apply AZ 701 by a one-step spinning at 4000 rpm for 40 sec with an acceleration of ~4000 rpm/min (thickness ~800 nm)
**d.** Soft bake at 100 °C for ~60 sec on hotplate
**e.** Expose ~100 sec at vacuum contact mode
**f.** Post exposure bake at 110 °C for ~60 sec on hotplate
**g.** Develop by immersing in AZ-726:$H_2O$ = 2:1 for ~60 sec
**h.** Rinse with DI water for ~60 sec.

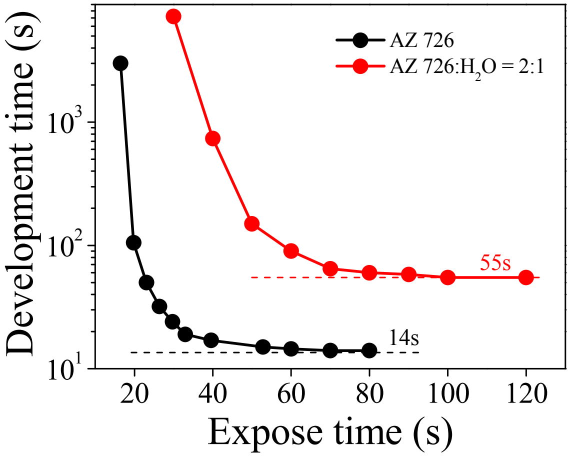

**Figure 2.5:** The development time of AZ-701 resist with a thickness of ~800 nm as a function of expose time in different developers of undiluted and diluted AZ-726. The dilution rate is [AZ-726]:[$H_2O$] = 2:1 in volume. The soft bake is 100 °C for ~60 sec and the post bake is 110 °C for ~60 sec and the exposure power density is 5mW/cm$^2$.

The lithography process described above allows a 500 nm lines-and-spaces resolution and individual waveguide patterns with a width down to 0.4 μm. This process aims to achieve a good mask for dry etching and the dimensions of patterns designed on the mask can be faithfully transferred to the target substrate assuming no undercut etching occurs. The current process is able to guarantee feature sizes above 1.0 μm with acceptable imperfection density and good reliability, while below 1.0 μm the degree of fabrication imperfection may increase. It is important to add that a successful lithography depends on precise control of the whole process and it could be further improved in several ways, for example by removing edge bead and using an antireflective layer especially when requiring large-area uniformity. Finally, we show the SEM images of a lines-and-spaces pattern and waveguide pattern before and after etching, proving that the optimized contact lithography process can resolve these features almost down to the theoretical resolution limit[1].

---

[1] The resolution of contact lithography is governed by near-field diffraction and the minimum period of line-space pattern can be expressed as $2W_{\min}\sim 3\sqrt{\lambda z/2}$, where $\lambda$ is the wavelength of exposure light and $z$ is the thickness of resist. For 320 nm light and 750 nm thick resist, it gives ~1.0 μm period.

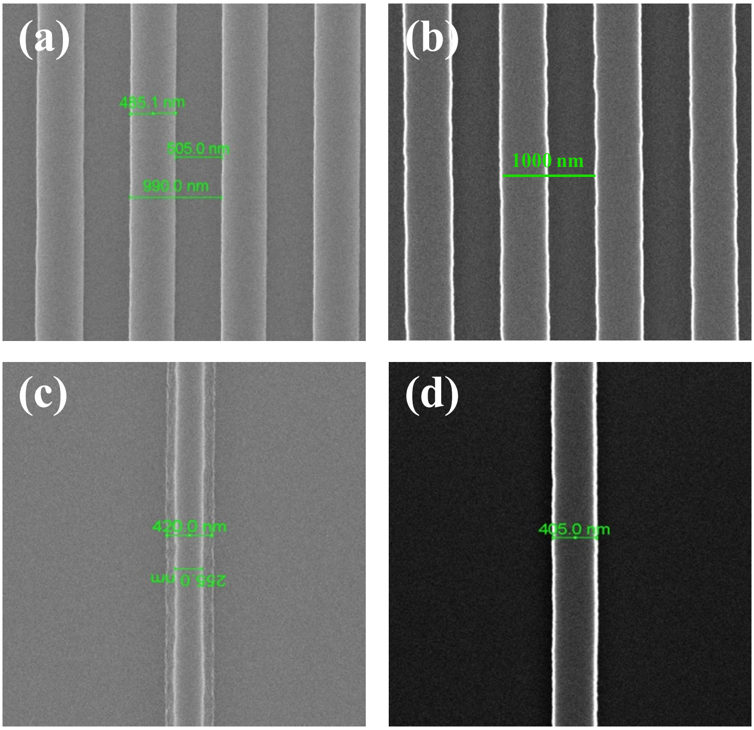

**Figure 2.6:** The lines-and-spaces design with 1.0 μm period of (a) photoresist pattern and (b) SiN pattern after etching. Waveguide with 400 nm design width in (c) resist pattern and (d) etched pattern.

## Etching

Etching is another important process for transferring pre-defined patterns into substrate layers in planar micro-fabrication technology. Two main etching approaches can be distinguished: wet chemical and dry plasma etching, the former performed usually in a reactive solution while the latter mostly in a plasma gas reactor. Briefly, for a plasma etching process, a plasma generator creates etchant species (atoms, molecular radicals and ions), and the material to be etched is removed by chemical reactions of those reactive radicals along with volatile products formed and evaporated (chemical etching), and/or by direct physical sputtering due to ion bombardment on the material (physical etching). In general, physical etching is directional and shows less material dependence, while chemical etching is sensitive to material properties and usually nondirectional. All plasma conditions including excitation power, pressure, and gas chemistries can affect the etching process and results. For more fundamentals of plasma etching, the reader is referred to some excellent books

[55, 56]. In this thesis, dry etching, more specifically reactive-ion etching (RIE), will be used for structuring the SiN layers. A resist pattern is used as mask in an Advanced Vacuum Vison 320 RIE tool equipped with 13.56 MHz RF excitation and a cooling system to maintain the sample plate temperature at ~20 °C.

The most important aspect for dry etching is directionality, particularly in the context of defining submicron structures. The directionality refers to different etch rates in horizontal and vertical directions with respect to the sample surface, resulting in two typical etched sidewalls – anisotropic and isotropic profiles – as illustrated in Figure 2.7. For an ideal anisotropic process, etching takes place only in vertical direction, leading to faithful pattern transfer and vertical sidewalls; while in an isotropic process, etching has no preferential direction, resulting in characteristic undercutting of the mask and circular profiles. We can define the degree of anisotropy $A$ as $A$=1-$d_H/d_V$, where $d_H$ is the horizontal undercut distance and $d_V$ is the vertical etch depth, and thus for totally isotropic and anisotropic etch we have $A$=0 and $A$=1, respectively. In the case of waveguide definition, obviously an anisotropic etch is desired to achieve a rectangle waveguide with controlled dimensions, especially when the line width of the waveguide is comparable to the film thickness. In general, plasma etching gives only partially anisotropic profiles due to the chemical etching component involved. But almost pure anisotropic etching can be attained by control of the physical and chemical processes occurring during plasma etching and thus the etch rate ratio of vertical to horizontal components could be significantly increased by boosting the vertical etch rate and/or suppressing the horizontal rate. Two phenomenological mechanisms of etching have been proposed to achieve such enhanced directional etching: ion-enhanced vertical etching and inhibitor-induced anisotropic etching [56], as schematically shown in Figure 2.8. During the first process, ion impact damages the surface of the material to some extent and makes it more chemically reactive to the neutral radicals and thus accelerates the chemical etching in the vertical direction. Meantime, the etching of the sidewalls proceeds at a normal and relatively slow chemical etch rate, since the ion flux mainly moves perpendicular to the surface and has no essential bombardment on the lateral surface, thereby leading to an anisotropic etch profile. In the second mechanism, the formation of inhibitor materials (e.g., polymers) occurs under some plasma circumstances and an inhibitor film can be deposited on lateral sidewalls that see little or no ion bombardment. This film then can act as a passivation barrier to completely inhibit sidewall etching, as depicted in Figure 2.8. By contrast, on horizontal surfaces the ion attack can prevent formation of the inhibitor film and makes these areas continuously subject to chemical radicals and thus keeps the etching proceeding, thereby making the total etch anisotropic. In practice, obviously, the maximum anisotropy can be obtained by combining above two mechanisms.

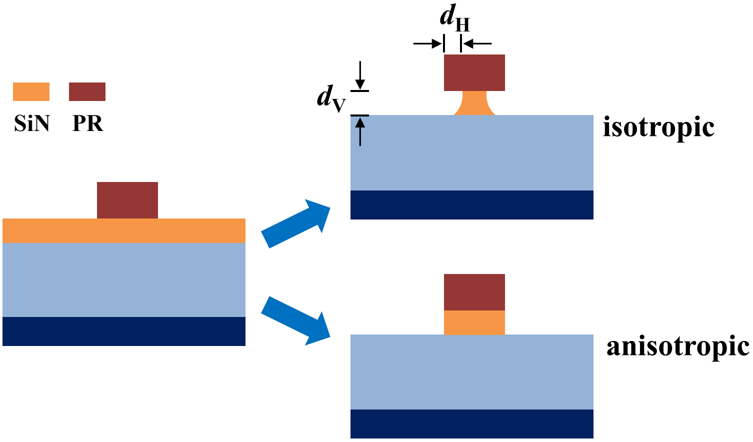

**Figure 2.7:** Illustration of isotropic and anisotropic etching profiles with PR as mask.

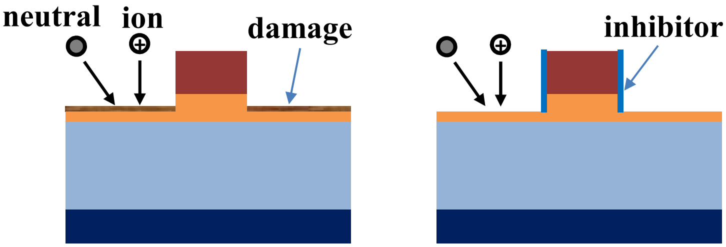

**Figure 2.8:** Two mechanisms responsible for anisotropic etching: ion-enhanced vertical etching (left) and inhibitor-induced anisotropic etching (right).

In our study, we choose fluorocarbon $CF_4$ as the basic gas for SiN etching. Additional gases ($O_2$, $H_2$, $SF_6$) are also used to adjust the etch conditions. In the fluorocarbon plasma system, the fluorine to carbon (F/C) ratio is a key factor to determine the boundary between polymer inhibitor formation and etching and this ratio can be readily adjusted by additives such as $O_2$ and $H_2$, as illustrated in Figure 2.9. Since the conditions of either pure polymer formation or pure etching cannot result in effective anisotropic etching, we need precise control of the plasma conditions to balance the protective and etching processes and to maximize the anisotropy. Moreover, in photonic devices a smooth etched surface with less roughness is desired and the etching process should also fulfill this requirement. Last, since SiN films deposited at different temperature are used for further integration, our etching should allow for an anisotropic profile starting from such mixed SiN layers with considerable differences in material density and hence in the etching behavior between those SiN films. For simplicity, hereafter the terms H-SiN and L-SiN will be used to refer to SiN deposited at high temperature (~270 °C) and at low temperature (~120 °C) respectively. It should be mentioned that the PECVD frequency shows negligible effect on the etching and we distinguish SiN only according to deposition temperature.

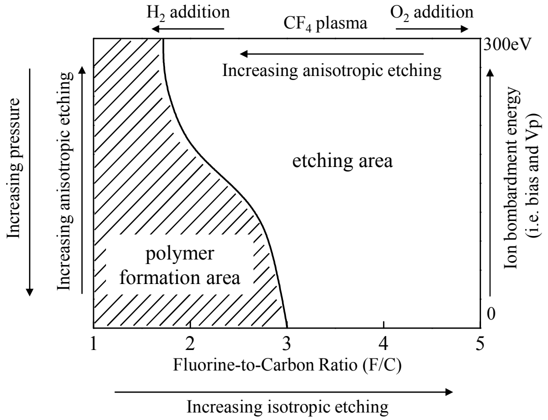

**Figure 2.9:** Etching and polymerizing regimes in $CF_4$ plasma as influenced by various plasma conditions. Adapted from [55, 57].

As a good starting point for optimization of the etching process, first we examine the influence of general plasma conditions on the etch rate and experimentally obtain the overall effect of these conditions in the etching process, similarly as shown in Figure 2.9. The etch rate is measured for both H-SiN and L-SiN films. First we add $H_2$ or $O_2$ to $CF_4$ and show the results in Figure 2.10. Clearly, the addition of $H_2$ reduces the etch rate and eventually stops the etching. This is attributed to the inhibitor formation exceeding the etching rate. The etch rate selectivity of L-SiN to H-SiN is also reduced, implying the transition of the dominant etching process from chemical to physical etching, as we expect less material dependence in a physical etching process. These effects associated with the increasing $H_2$ to $CF_4$ ratio arise from the reduction of fluorine radical concentration via H-F combination and H-assisted inhibitor formation. The function of $H_2$ is potentially useful to realize an anisotropic etching, as will be discussed later. Oppositely, initial addition of $O_2$ increase the etch rate as well as the selectivity of L-SiN to H-SiN, associated with increasing the concentration of fluorine radicals via C-O combination. Additionally, the presence of $O_2$ can remove the inhibitor polymers and thus favor isotropic etching. Note that at higher $O_2$ content the etch rate does not further increase but declines because of a relatively lower percentage of etchant gas $CF_4$. In Figure 2.11, we show the effect of plasma power and chamber pressure on the etch rate. With increasing the plasma power, the bias voltage for accelerating ions is increased, resulting in enhancement of ion-assisted chemical and physical etching. To maintain a moderate etch rate the plasma power is fixed at 210 W for all of the following experiments, if not specified otherwise. Increase of pressure creates higher density of plasma and enhances the chemical etching, while reducing the mean free paths of ions and thereby decreasing the ion bombardment effect. Nevertheless, the etch rate still increases as long as the ions can maintain moderate attack on the surface.

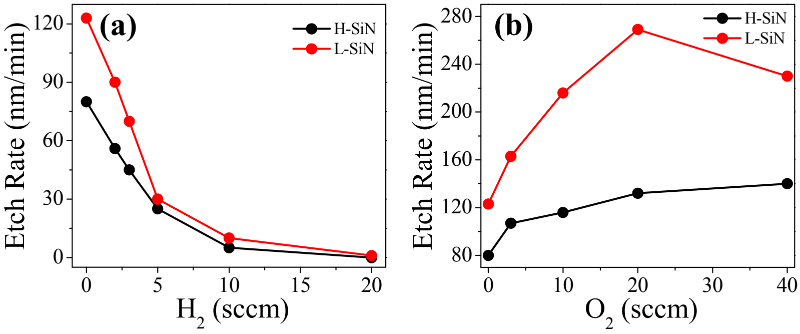

**Figure 2.10:** The etch rate as a function of gas flow rate. (a) Power = 150W, Pressure = 40mTorr, $CF_4/H_2$ = 40sccm/X sccm. (b) Power = 150W, Pressure = 40mTorr, $CF_4/O_2$ = 40sccm/X sccm.

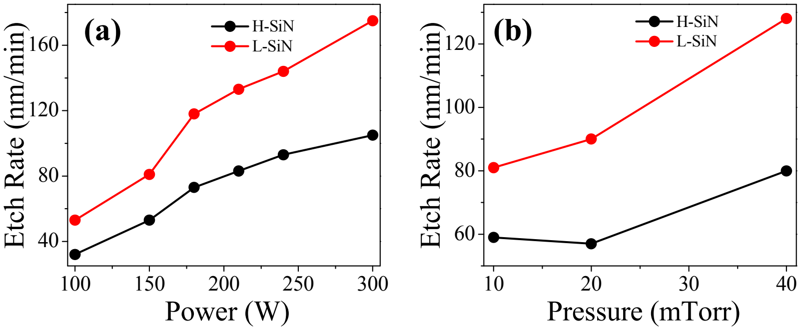

**Figure 2.11:** (a) The etch rate as a function of power. Pressure = 40mTorr, $CF_4/H_2$ = 40sccm/3sccm. (b) The etch rate as a function of pressure. Power = 210W, $CF_4/H_2$ = 40sccm/3sccm.

In the following section, we will comprehensively optimize the etching process by adjusting pressure and gases to obtain vertically etched sidewalls and smooth surfaces. The optimal conditions will be determined by detailed SEM analysis of the etch profiles of structures defined in a SiN film.

## Planarization

Surface planarity is a prerequisite for ensuring high-quality lithography. In general, a photonics fabrication process begins with a flat substrate that is then processed by various planar processes including deposition, patterning, etching, and so on. These processes always introduce surface roughness and topologies, for example, waveguide fabrication creates ridge and trench-like topologies as depicted in Figure 2.12(a), and thereby prohibits further build-up of complex structures in particular for a device with a vertical coupling scheme that will be later used in our integrated waveguide-coupled high-Q microresonator. Planarization is a process that evens out any submicron irregular topographies and smoothes the surface of a substrate. A number of planarization techniques to achieve this goal were developed such as thermal reflow process, etch-back method, and chemical mechanical polishing (CMP). Among these, CMP can attain global planarization across the entire substrate with extremely smooth surface finish and thus will be utilized in our fabrication. A typical CMP process uses an abrasive and corrosive slurry (e.g., silica particle suspension) to remove rough pieces of the substrate surface assisted by both chemical corrosion and mechanical polishing. In practice, a substrate is mounted upside down on a rotating (sometimes also sweeping) carrier and the surface to be planarized is brought into contact with a rotating platen which is covered with a polishing pad, while applying a certain mechanical force on the carrier. During the motions of the carrier and platen, the slurry continuously flows onto the platen. Higher points on the substrate are removed first and faster than the lower areas by small particles, eventually achieving planarization. In this thesis, we use a Mecapol P400 polishing tool from Presi together with a Stacked IC1000/Suba IV polishing pad and a silica slurry (particle size of 30-50 nm).

The aim of planarization is to end up with a smooth surface on top the pre-fabricated components. Therefore, the deposition of a material matrix prior to CMP is needed for protecting fabricated structures and providing removable material, as shown in Figure 2.12(b). In our experiments, either $SiO_2$ or aSi is deposited depending on the targeted end structure. As a rule of thumb, the thickness of the deposited layer is about 2–3 times the initial step of the structures. Depending on the endpoint of the polished surface, we can distinguish between two kinds of polishing results – under polishing and critical polishing – as shown in Figure 2.12(c) and (d) where the polish ends up in the deposited layer and at the very top of the structure, respectively. In a real process, critical polishing is difficult to achieve and usually we obtain an over polishing profile in which the structures are also slightly polished. After optimization of experimental parameters for the polishing tool used in our fabrication, we can achieve the planarization with a local roughness (peak-peak) below 5 nm and a global planarity of ±15 nm thickness variation over a length of 10 mm. In Figure 2.13 we show the SEM results of different CMP steps on a structured Si wafer as an example and it is clearly seen that the developed CMP process can achieve chip-scale planarization.

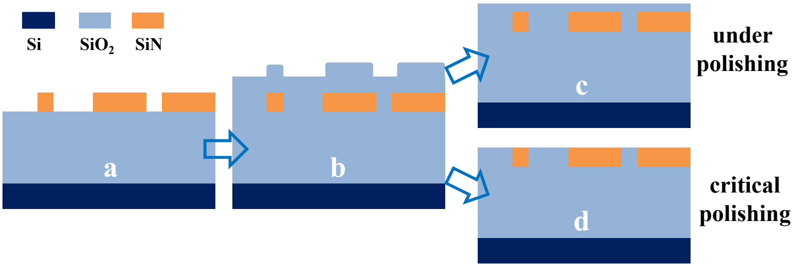

**Figure 2.12:** Schematics of CMP process with $SiO_2$ deposition. (a) Substrate with patterned SiN structures. (b) Over deposition of $SiO_2$ cladding. Two CMP surface finishes of under polishing (c) and critical polishing (d).

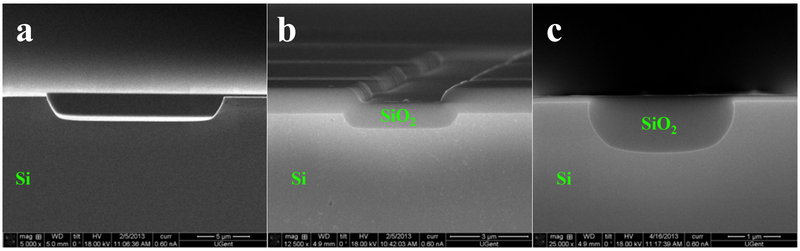

**Figure 2.13:** A real CMP flow: (a) patterned substrate, (b) deposition of $SiO_2$, and (c) result after CMP process.

## 2.3 Low-loss SiN waveguides

In this section, we will explore an optimized dry etching process for SiN photonic fabrication. Based on this technique, we design and fabricate waveguide wires for wavelengths ranging from 630 nm to 1360 nm. The losses for these waveguides are characterized in detail.

### 2.3.1 Optimization of dry etching

As pointed out before, achieving low loss waveguides requires vertical and smooth sidewalls and therefore we need optimization of the RIE conditions. Various plasma chemistries, such as $CHF_3/O_2$ [17], $CF_4$ [34], $C_4F_8/SF_6/H_2$ [37], and $SF_6/CH_4$ [50], have already been used in SiN photonics. In our fabrication, we aim to develop versatile etching recipes that are capable of achieving anisotropic and smooth etching not only for a single SiN layer but also for a SiN film stack deposited at different temperature. However, unlike what is the case for SiN-films deposited in a single step, due to the considerable difference in material density the etching behavior of H-SiN and L-SiN films deposited on top of each other can vary a lot. As a result, the standard etching processes described in literature result in a stepwise transition at the interface, which can lead to uncontrolled waveguide dimensions and additional losses. An optimized process should be sufficiently anisotropic and can passivate the sidewalls such that those are not etched during the process, resulting in topologically united sidewall surfaces. Moreover, the roughness of the etched sidewalls should be minimized to reduce the associated scattering loss of the waveguide. Further, even for etching of composite SiN films integrated with quantum dots which will be discussed in Chapter 4, the process should be capable of achieving vertical sidewalls and reasonably smooth surfaces. Consequently, the understanding of etching behavior of SiN in our plasma system is necessary and detailed analysis of the etching results is needed for evaluating the efficiency of the experimental setting.

Based on previous results of SiN etching in a $CF_4$ plasma, we fixed the RF power at 210 W and focus on the effects of pressure and gas ratios on etching profiles of H-SiN/L-SiN layers. The etched samples are inspected by SEM analysis on FIB milled cross-sections. In order to avoid excessive charging effects, we carried out the initial etching experiments and the corresponding SEM check on SiN-films deposited on bare silicon substrates without the insulating $SiO_2$ buried oxide layer. This resulted in considerably better pictures and allowed inspecting both the etched profile and surface roughness with higher resolution.

The optimization begins with studying the influence of plasma pressure on etched profiles. We etched an H-SiN/L-SiN stack with a fixed gas composition of $CF_4/H_2$ (80sccm/3sccm) but under different pressures. The addition of $H_2$ is expected to facilitate the formation of inhibiting polymers and thus the gas contribution to isotropic etching can be reduced or eliminated from our consideration. In Figure 2.14(a-c) we show FIB-defined cross-sectional images of the H-SiN/L-SiN films etched at 20, 40, and 80mTorr, respectively. When making a cross section, the structure is protected by a Pt layer deposited in situ by electron beam and ion beam. Note that the resist mask was retained during SEM examination for verifying the reliability of the contact lithography process. For a pressure of 20mTorr, the profile exhibits nearly vertical sidewalls without observable steps at the interface of H-SiN and L-SiN. Two reasons can account for this result: either the same lateral etch rates for two SiN layers or no lateral etching at all owing to the formation of an inhibitor layer. However, the measured etch rates for unpatterned H-SiN and L-SiN films are 75 nm/min and

111 nm/min, respectively, implying different etch rates also in the lateral direction, although such difference could be smaller than in the vertical direction. Consequently, under 20mTorr pressure the steep sidewalls are attributed to the formation of a protective polymer that prevents the etching of sidewalls. In Figure 2.14(a), it is also obvious that the resist mask has a steep sidewall and that the dimension of the designed feature is faithfully transferred into the SiN, demonstrating the suitability of our contact optical lithography for defining a dry etching mask. With increasing pressure, however, the sidewalls show a more circular profile with a clearly observable discontinuity at the interface between both SiN layers especially for 80mTorr pressure as shown in Figure 2.14(c). Compared with Figure 2.14(a), there is also a considerable reduction in dimensions, ~55 nm and ~85 nm in bottom width for 40mTorr and 80mTorr, respectively, a clear indication of sidewall etching due to insufficient inhibitor growth. At higher plasma pressure, the density of reactive species proportionally increases and hence chemical etching is promoted. Since the sidewall inhibitor can also be removed by plasma etching and when the removal rate outcompetes the polymer deposition rate, sidewall etching occurs, making the etching less anisotropic. To ensure a satisfying protection of sidewalls, the pressure is kept at 20mTorr for the following experiments.

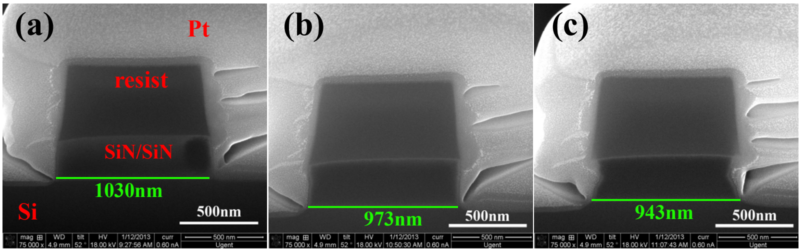

**Figure 2.14:** FIB cross-sectional images of the as-etched H-SiN/L-SiN waveguide with a designed width of 1.0 µm and a total thickness of 300 nm. The etching gases are $CF_4/H_2$ (80sccm/3sccm) and the pressures are (a) 20mTorr, (b) 40mTorr, and (c) 80mTorr.

Next, to investigate the influence of the gas composition on the degree of anisotropy, we etched an H-SiN/L-SiN stack with pure $CF_4$ and then added either $O_2$ or $H_2$ for comparison. In Figure 2.15(a-c) we show cross-sectional images of the H-SiN/L-SiN films etched with $CF_4$ (40sccm), $CF_4/O_2$ (40sccm/3sccm), and $CF_4/H_2$ (40sccm/3sccm), respectively. Pure $CF_4$, as shown in Figure 2.15(a), etches both SiN layers primarily in the vertical direction but there is also considerable lateral etching resulting in a curved profile. To adjust the etched profile, we first added a small amount of $O_2$ to the $CF_4$ flow. The result is shown in Figure 2.15(b), showing that the presence of $O_2$ results in a more isotropic etching of the L-SiN layer with strong undercutting of the resist mask. At the interface between both SiN layers a strong step is visible indicating that the L-SiN and H-SiN exhibit significantly different etch rates in the horizontal direction. This enhanced isotropic etching results from the increasing concentration of fluorine radicals together with the lack of sidewall protection, which is removed in the presence of the $O_2$ plasma [55]. The impact is stronger for the L-SiN layer. As a consequence the horizontal etch rate difference between L-SiN and H-SiN is increased, leading to a step at the interface. The variation in horizontal etching rate between the L-SiN and H-SiN layers is a further manifestation of the distinct change in their material density and of the need for a nearly complete anisotropic etching process for obtaining vertical sidewalls with a continuous surface. In Figure 2.15(c), we present the etched profile when using a gas mixture of $CF_4/H_2$ which shows the desired straight sidewall with a united surface, albeit with a slight slope. This significant improvement can be attributed to a greatly increased anisotropic etching occurring due to the formation of a protective polymer layer on the sidewalls in the presence of $H_2$ [57, 58]. This polymer layer inhibits etching of the lateral surfaces whereas on the bottom surface it is removed by the directional ion bombardment leaving it fully exposed to reactive species. Accordingly the process is dominated by the vertical etching component and there is hardly any lateral etching. Therefore, we adopt the gases of $CF_4/H_2$ for the further experiments.

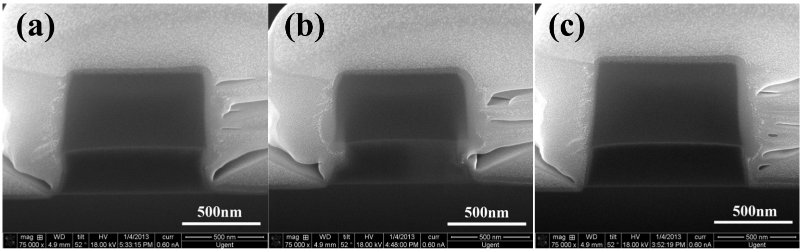

**Figure 2.15:** FIB cross-sectional images of the as-etched H-SiN/L-SiN waveguides. The etching gases are (a) $CF_4$ (40sccm), (b) $CF_4/O_2$ (40sccm/3sccm), and (c) $CF_4/H_2$ (40sccm/3sccm).

In order to further improve the etch profile in terms of sidewall slope and surface roughness, we adjusted the $CF_4/H_2$ ratio in the process using values of 40sccm/3sccm, 60sccm/3sccm, and 80sccm/3sccm for the respective gas flows (Figure 2.16). When increasing the proportion of $CF_4$ in the system, the slope of the etched sidewall is gradually tuned from a positive profile to a vertical one as obvious in Figure 2.16(a-c). More importantly, the roughness of the sidewall is reduced by increasing the ratio of $CF_4$ to $H_2$. The effect of the $CF_4/H_2$ ratio on the sidewall slope originates from the competition between the etching process and the polymer inhibitor deposition [57]. At proportionally higher hydrogen flows ($CF_4/H_2$ ratio of 40sccm/3sccm) there is an excess deposition of the polymer inhibitor on the lateral surface where it is not removed by the vertical ion bombardment, resulting in a sloped profile and a much rougher surface as shown in Figure 2.16(a) and (d). As an extreme example of this effect, when increasing the $H_2$ flow rate to 20sccm no etching at all occurs as shown previously. By reducing the hydrogen content ($CF_4/H_2$ ratio of 80sccm/3sccm) the fine balance between etching and deposition results in a vertical sidewall and an improved surface roughness, as shown in Figure 2.16(c) and (f). When further increasing the $CF_4$ flow the profile tends toward the profile obtained using pure $CF_4$, shown in Figure 2.15(a).

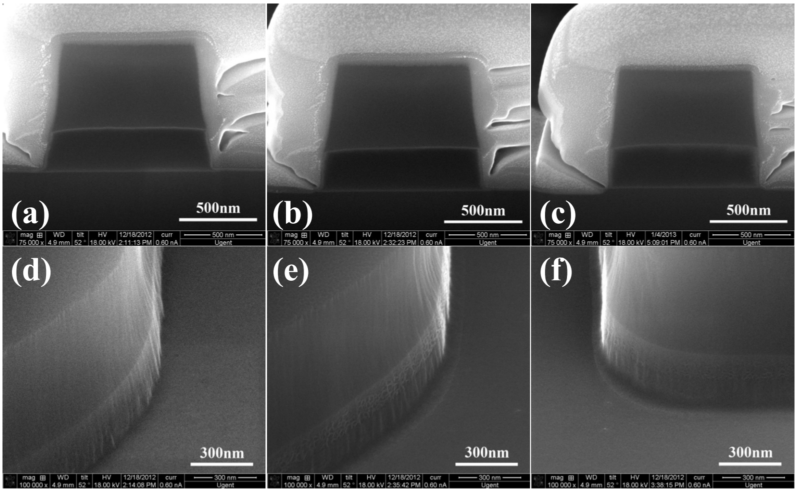

**Figure 2.16:** FIB cross-sectional and sidewall images of the as-etched H-SiN/L-SiN layers. The gas system is $CF_4/H_2$ with different ratios of (a, d) 40sccm/3sccm, (b, e) 60sccm/3sccm, and (c, f) 80sccm/3sccm.

Summarizing, under a critical ratio of $CF_4/H_2$ (80sccm/3sccm), a proper pressure (20mTorr), and a RF power of 210 W, the RIE process is dominated by anisotropic etching featured by nearly vertical sidewalls while at the same time the roughness of surface is reduced. Under these conditions the etch rates are ~70nm/min for H-SiN, ~100nm/min for L-SiN, and ~30nm/min for AZ-701 resist. These conditions are valid for single H-SiN and L-SiN layers or the combination of them. However, we should point out that etching of pure H-SiN films the process could be slightly shifted to the isotropic side by finely adjusting plasma conditions to balance the sidewall profile and surface roughness for minimizing the losses of devices. The same strategy can also be used to obtain the etching recipe for LPCVD SiN. On the other hand, for composite films of SiN with other materials like quantum dots, the etching recipe also needs small modification as will be shown in Chapter 4.

### 2.3.2 Design and fabrication

As the standard waveguide design, we adopt a strip geometry with a rectangular cross section as shown in Figure 2.17. In such a waveguide structure, the optical modes can be classified according to the polarization of the electric (magnetic) field into two types: quasi transverse-electric (quasi-TE) and quasi transverse-magnetic (quasi-TM) modes. In the coordinates of Figure 2.15, the dominant component of the E-field is $E_y$ for quasi-TE modes while $H_y$ is dominant in quasi-TM modes (H-field mainly lies in x-y plane so the name of transverse-magnetic). For simplicity, hereafter these modes will be simply referred to as TE and TM. In our waveguide design and loss analysis, only TE modes will be considered and the loss measurements are carried out at three wavelengths of $\lambda$=638 nm, 900 nm, and 1310 nm. In fact, the waveguide transmission spectra in the ranges of 600–900 nm and 1260–1360 nm (O-band) show no observable intrinsic absorption peaks and thus the losses studied at these wavelengths can represent the loss level of above broad ranges.

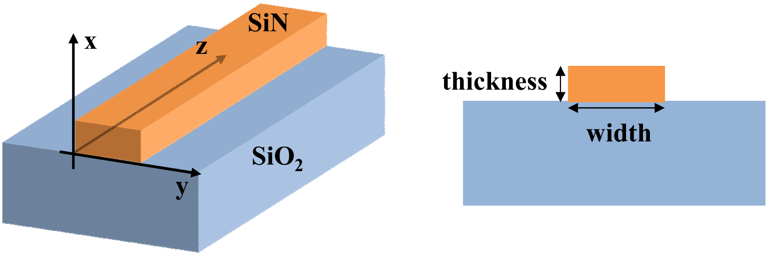

**Figure 2.17:** Geometric configuration of strip SiN waveguide.

We theoretically investigate the loss at $\lambda$=900 nm and the thickness is set at ~ 200 nm so that TM modes cannot be supported in single-mode TE waveguide. By numerically solving Maxwell's equations for the electromagnetic field under given boundary conditions with the finite difference method, we find the optical modes and their properties. In Figure 2.18(a) we plot the calculated effective indices $n_{\mathrm{eff}}$ of the fundamental (the first order) and the second order TE modes in SiN waveguide with different widths. Guided modes exist only when $n_{\mathrm{eff}}$ is larger than the substrate index. Thus for single-mode operation the width can range from 0.5 to 1.2 μm. Above 1.2 μm the 2nd TE mode is also supported. Figure 2.18(b) and (c) present the cross-sectional mode profiles for the 1st and 2nd TE modes in waveguides with a width of 0.8 μm and 1.6 μm, respectively. The mode confinement factor, defined as the fraction of the mode energy density in the waveguide region, is an important parameter for the waveguide and we obtain ~60% confinement factor for TE modes at 200 nm thickness. For integrated photonics, waveguide bends are always necessary and bending loss should be considered in the design. Figure 2.19 shows the calculated bending loss as a function of bend radius for a 0.8 μm-wide waveguide. Here the bending loss refers only to the radiation loss of bending modes and does not include any losses caused by mode mismatch. In practice, the bending loss should be low, for instance below 1.0 dB/cm, and from Figure 2.19 this loss corresponds to a minimum bend radius of ~25 μm with a loss of 0.006 dB/90° turn. By changing the geometry of the waveguide even smaller bend radius can be achieved, for example, a bend radius of 10 μm is practically feasible for a 1.0μm-wide and 0.25μm-thick waveguide.

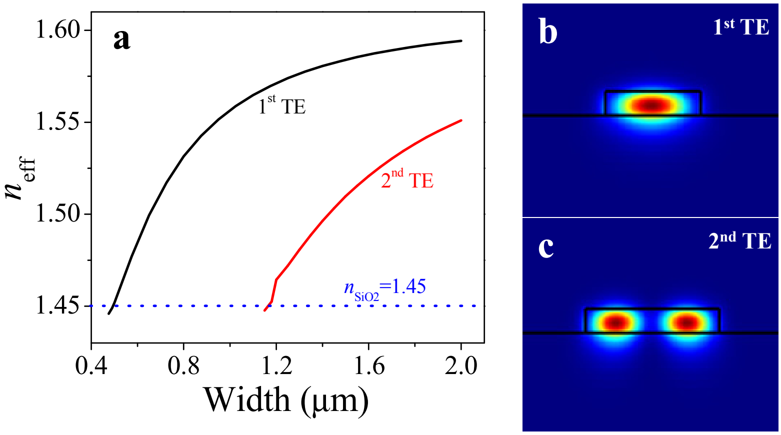

**Figure 2.18:** Optical modes of SiN waveguide with 200 nm thickness at $\lambda$=900 nm. (a) Calculated effective index $n_{eff}$ of the first and second order TE modes as a function of waveguide width. Here we take the index of 1.92 for SiN and 1.45 for oxide. The electric field intensity profiles for the waveguides with a width of 0.8 μm in (b) and 1.6 μm in (c).

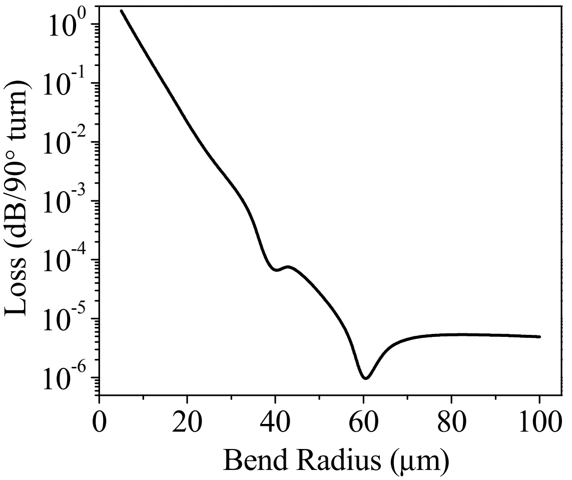

**Figure 2.19:** Calculated bending loss as a function of the radius of bends for 0.8μm-wide and 0.2μm-thick SiN waveguide at $\lambda$=900 nm.

To fabricate the waveguide circuits, we designed a contact mask which contains waveguide wires with widths varying from 0.8 μm to 2.0 μm, taking into consideration the limits of mask manufacturing and lithography. For each width we included a straight reference waveguide and spiral waveguides with a series of lengths of 1, 2, 4, and 8 cm for loss measurements with the cut-back method. The number of bends (90° turn) for all spiral waveguides are the same (32 bends in total) and the bend radius is fixed at 100 μm, for which the bending loss is negligible according to the calculation. Away from the spiral part, both sides of the waveguides are tapered to 3.0 μm to facilitate easier facet cleaving and reproducible coupling to and from the chip. The fabrication starts with a Si (100) wafer with a 3 μm thermal $SiO_2$ box layer, onto which a single PECVD SiN layer (thickness depending on operating wavelength) is deposited. Both H-SiN and L-SiN films prepared under different plasma frequencies are employed to fabricate waveguides to compare the losses between them. After deposition, the whole wafer is diced into about 2.5 cm by 2.5 cm chips along the <110> crystal orientation for further processing. By using the previously optimized lithography process we pattern the chip with AZ-701 resist keeping waveguide lines parallel to the edge of the chip for easy cleaving. The chip is subsequently etched with the optimized RIE recipe described above to transfer the waveguide patterns into the SiN layers and form strip waveguides. Finally, the chip is cleaned in Acetone and then $O_2$ plasma for measurement. In Figure 2.20 we present the SEM pictures of the fabricated SiN waveguides with ~200 nm thickness. The high quality in terms of waveguide sidewall, defect control and large-area uniformity are obvious, indicating the reliability of the fabrication process.

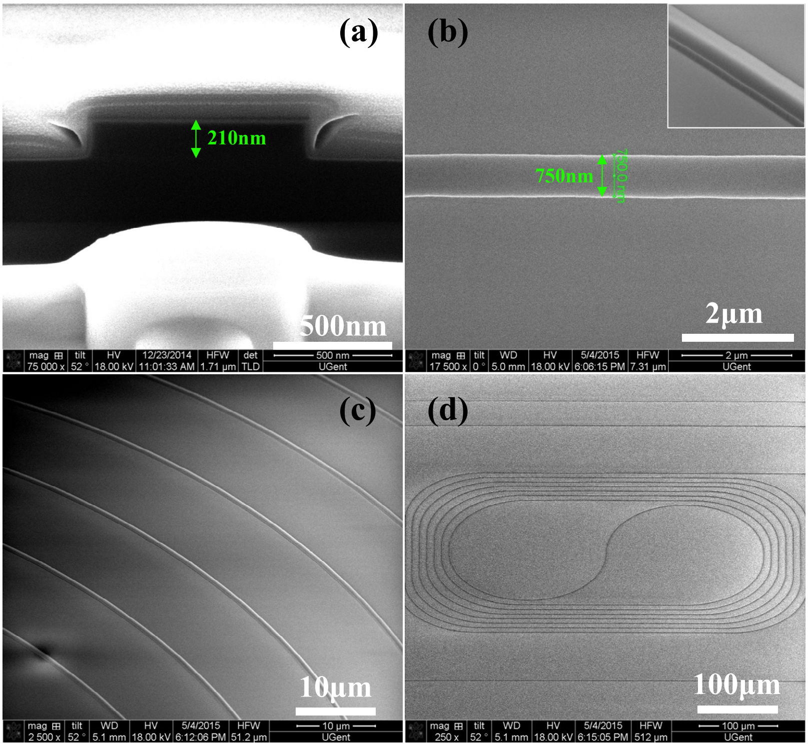

**Figure 2.20:** SEM pictures of fabricated H-SiN waveguides with ~200 nm thickness. (a) Cross section of waveguide, (b) top view image with inset showing tilted sidewall, (c) titled view of spiral waveguide, and (d) overview of 1.0 cm-long spiral waveguide.

### 2.3.3 Waveguide loss characterization

In order to measure the transmission of the waveguides, the two sides of the chip are cleaved perpendicular to the waveguide lines to form facets and enable fiber edge coupling. The waveguide propagation losses are determined with a cut-back method by measuring transmissions of spiral waveguides of different lengths, whereby the losses can simply be extracted by fitting the length-dependent fiber-to-fiber transmission. The measurement is carried out on a horizontal set-up, as shown in Figure 2.21. The set-up uses microlensed fibers to couple light in and out to the cleaved facets of the waveguide and the fibers are horizontally mounted on XYZ translational piezo-stages, which allow for precision alignment of the fiber tip with respect to the waveguide facet. The cut-back method for measurements of propagation losses assumes constant coupling conditions for waveguides with identical design but varying lengths and thus the transmission will be linearly dependent on the length of the waveguides in a dB scale. However, in real measurements the coupling is not identical shifting from waveguide to waveguide. We estimated the coupling uncertainty to be below 1.5 dB. Considering the longest spiral waveguide is 8 cm, this uncertainty results in an upper limit for the error in the measured losses of less than 0.2 dB/cm.

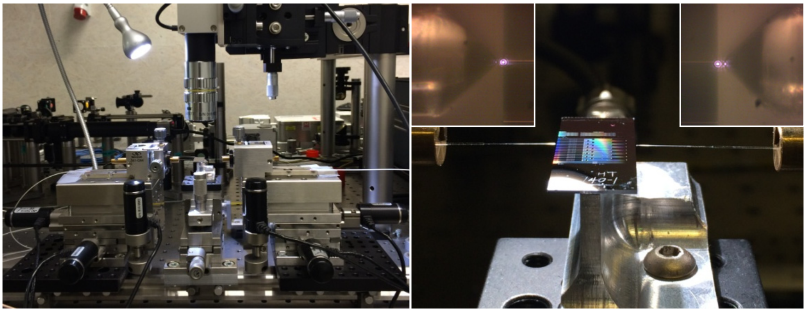

**Figure 2.21:** Photograph of horizontal fiber setup. Left: the overview of the whole setup. Right: the waveguide chip aligned to the fibers. The insets are micrographs of alignment of the lensed fiber to a waveguide.

## I. Waveguide loss @ $\lambda$ = 900 nm

We fabricated waveguides with a thickness of ~200 nm and measured the transmission at $\lambda$=900 nm using a near-infrared tunable laser. The transmitted power is maximized with a polarizer resulting in excitation mainly of the TE modes. We use single-mode lensed fibers designed for 1550 nm, and the measured insertion loss for one waveguide facet is ~2.5-3 dB at 900 nm. Note that for wider waveguides supporting 2nd order TE modes light from the lensed fiber can be coupled into higher order modes (albeit less efficiency given the larger mode matching with the fundamental mode). Therefore the measured loss is in fact the combination of 1st and 2nd order TE mode losses, which will be larger than the loss for a pure 1st order TE mode.

First, we investigate the influence of the deposition temperature on the waveguide loss. The SiN films are deposited at low RF frequency (~100 kHz), as from ellipsometry measurements (see section 2.2) this type SiN is expected to have a lower material absorption loss. We measured the losses for H-SiN and L-SiN waveguides and the results are plotted as function of the designed waveguide width in Figure 2.22(a). For both cases, the losses rapidly decline for widths increasing from 0.8 µm to 1.2 µm and then exhibit a more gradual decrease for widths varying from 1.2 µm to 1.5 µm. The relatively larger losses and fitting errors at widths of 0.8 µm and 0.9 µm for both H-SiN and L-SiN waveguides can be attributed to the fact that the deviation of dimensions and other fabrication imperfections of in our optical lithography become more significant when the feature size decreases below 1.0 µm, resulting in notable scattering losses. For a L-SiN (*n*~1.85) waveguide with a 0.8 µm design width, the fabricated width is 650-700 nm close to the cutoff width of the fundamental TE mode and thus also leakage loss is non-negligible. When increasing the width to 2.0 µm, the losses for H-SiN and L-SiN apparently saturate to 0.94 dB/cm and 1.88 dB/cm, respectively. The inset of Figure 2.22(a) shows the transmission of the 2.0µm-wide waveguides for different lengths and the corresponding linear fits. The small discrepancy between the measured and fitted results clearly demonstrates the uniformity of lithography with a low defect density and the reliability of the cut-back method for determining the waveguide loss. It is interesting to note that for all widths L-SiN waveguides have about two times the loss of the H-SiN waveguides, which can be understood from the differences in material quality and sidewall etching. For smaller widths the effect of sidewall roughness dominates the waveguide loss and the SEM analysis showed this effect is relatively more important in L-SiN, causing the higher losses in L-SiN waveguides. For wider waveguides and in particular for the 2.0µm-wide waveguides, which support also higher order TE modes at the wavelength of 900 nm, the material absorption and the scattering within the waveguide become more important. This leads us to conclude that the L-SiN layer exhibits an intrinsically higher material loss (volume absorption and scattering) by a value of ~0.9 dB/cm than the H-SiN layer deposited at higher temperature. This can be ascribed to high hydrogen concentration associated principally with insufficient reaction during film formation at low deposition temperature [9, 13, 59] and therefore the material absorption and film inhomogeneity increase. Nevertheless, the loss below 2.0 dB/cm for SiN deposited at 120 °C indicates its capability for low temperature photonics, which will be very useful in some situations where low processing temperature is desirable, for example, we will use L-SiN in hybrid integration of SiN with quantum dots, given the fact that the optical quality of the quantum dots is maximally preserved when limiting the process temperature [60].

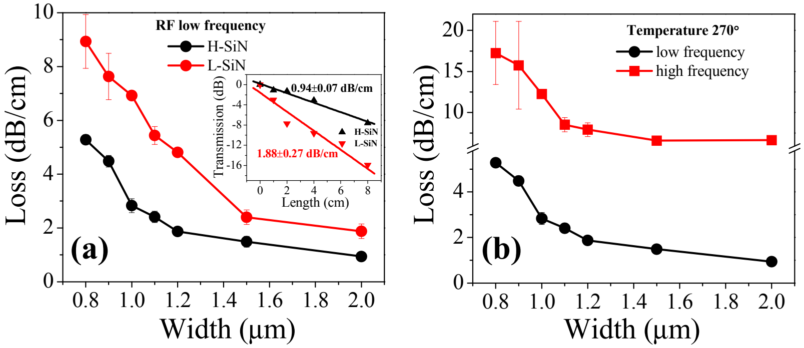

**Figure 2.22:** (a) Waveguide losses at different widths of H-SiN (270 °C) and L-SiN (120 °C) layers deposited at low RF frequency in (a) and of H-SiN (270 °C) layers deposited at different RF frequencies in (b), obtained by linearly fitting waveguide-length dependent transmission. The thickness of all waveguides is ~200 nm. The inset in (a) shows the transmission (normalized to the reference waveguide) of 2μm-wide waveguides at different lengths together with the corresponding linear fits of the slopes for different types of waveguide, indicating a very small discrepancy between the measured and fitted results.

As seen from optical index measurement, the RF frequency is another important parameter that can affect the material properties, particularly in terms of absorption. We measured the losses of waveguides fabricated from H-SiN films deposited at high RF frequency (13.56 MHz) and present the result in Figure 2.22(b). For comparison, the result of low-frequency H-SiN is also re-plotted. It is obvious that the high-frequency SiN exhibits higher losses compared with low-frequency SiN at the same waveguide width and this loss difference, considering similar etching and dimensions in both waveguides, is mainly due to material absorption. In 2.0μm-wide waveguides where the absorption loss is dominant over the scattering loss the measured data gives a good estimate for the material absorption, which at 900 nm is ~5.7 dB/cm larger in high-frequency SiN compared to low-frequency SiN. It is speculated that this higher material absorption coefficient is related to the fact that these films are Si-rich, resulting in a large content of Si-Si bonds in such nitride film possibly along with the formation of Si nanocrystals, those phenomena likely to be favored under high RF frequency but inhibited under low RF frequency [29]. In addition, the effect of RF frequency on material absorption appears to be reduced at low deposition temperature. Nevertheless, from now on, we focus only on low-frequency SiN films in further fabrication except where otherwise mentioned.

For practical applications, the loss of single-mode waveguides is of most interest. From the calculation, the upper cutoff width for single-mode operation is ~1.2 μm, corresponding to a measured loss below 2.0 dB/cm for H-SiN as shown in Figure 2.22. Therefore, we can state that a single-mode loss of ~2.0 dB/cm has been achieved in strip SiN waveguides. Although extensively optimized, the contact lithography used is still the biggest limitation in defining narrow waveguides with less imperfections, given that we are coming close to the theoretical resolution limits. Lower loss single-mode waveguides could be realized by reducing waveguide thickness and increasing the width, thereby relaxing pattering tolerances. In Figure 2.23(a), we show the simulation results for 135nm-thick waveguides and clearly see that the upper cutoff width for single TE mode operation is close to 1.8 μm. The mode in this waveguide is less confined in the SiN region than the mode in the 200nm-thick SiN waveguide. We experimentally verified this and show the measured losses in Figure 2.23(b). At a width of 1.5 μm, well below the cutoff width, we obtain a propagation loss of ~1.0 dB/cm as shown in Figure 2.23(b).

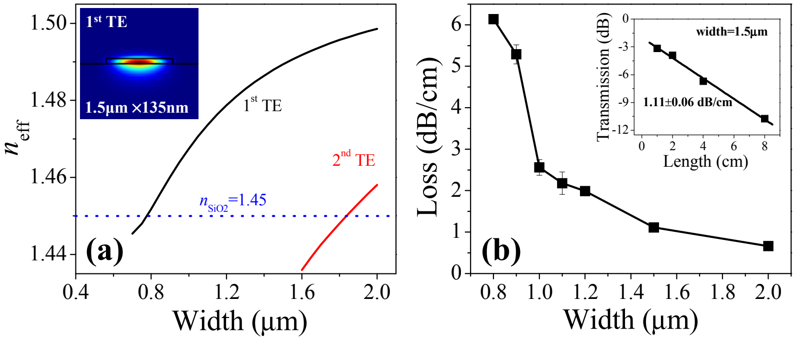

**Figure 2.23:** (a) Calculated effective index $n_{\mathrm{eff}}$ of 1st and 2nd TE modes as a function of waveguide width with $t$=135 nm thickness at λ=900 nm. The inset shows the field profile of the 1st TE mode in a 1.5 μm wide and 135 nm thick waveguide. (b) Measured waveguide losses at different widths with thickness of ~135 nm, obtained by linearly fitting waveguide-length dependent transmission. To cancel out the bending loss the data of the reference straight waveguide doesn't take part in the fit. The inset in (b) shows the transmission of 1.5 μm wide waveguides at different lengths together with the linear fit of the slope.

Nonetheless, a thinner waveguide results in a lower mode confinement factor of ~35% in 135 nm SiN thickness compared with ~60% in 200 nm SiN. As a consequence, the minimum bend radius to ensure low bending loss will significantly increase. For comparison, in a 1.2μm-wide waveguide the bend radius to maintain a ~1.0 dB/cm loss level is 100 μm for 135 nm thickness, whereas it is only 15 μm for 200 nm thickness. In addition to controlling the bending loss, a special design strategy is needed to reduce the scattering loss due to mode mismatch between straight and bend parts, and this often becomes more critical for thinner waveguides. As an experimental proof, we obtained an extra ~2.4 dB loss in 2µm-wide spiral waveguides which include 32 bends compared to that of a straight waveguide. Considering simulations show the bending loss of 2 µm wide waveguides is negligible, this excess loss can be attributed to mode scattering at straight-bend transitions. In 200nm-thick waveguides we do not observe such loss. Therefore, there is a trade-off between waveguide loss and other requirements in integrated photonics and the waveguide design should be carefully optimized for a given application.

## II. Waveguide loss @ $\lambda = 638$ nm

Next we explore the waveguide loss at visible wavelengths. In this case the thickness of the waveguide is set at ~140 nm in order to suppress TM modes and thus to a maximum extent get rid of their reflection in measured losses. To increase the coupling efficiency, we use single-mode lensed fibers designed for operation at ~720 nm. The measured insertion loss for one waveguide facet is ~4 dB. Figure 2.24(a) shows the measured losses for different waveguide widths. For 2.0 µm-wide waveguides we obtain losses as low as 1.16 dB/cm and 2.05 dB/cm for H-SiN and L-SiN waveguides, respectively. From the images in Figure 2.24(a) and (b), it is obvious that in terms of defects the fabrication is quite uniform over the measured area yet that the scattering loss is clearly noticeable. Especially, below 1.0 µm width the scattering related to the reaching the limit of the lithography process rapidly increases and becomes the main contribution to the waveguide loss as shown in Figure 2.24(a). It can be reasonably expected that a loss level of 2.0 dB/cm for H-SiN and 3.0 dB/cm for L-SiN in single-mode waveguides could be achieved by using high-resolution lithography. We should also point out that with the current thickness the bending loss due to mode mismatch is still high and a thicker waveguide design would be beneficial to reduce this loss even without special bend design.

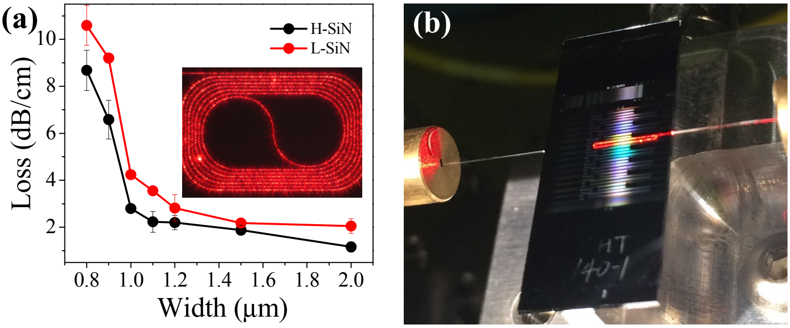

**Figure 2.24:** (a) Waveguide losses at different widths for H-SiN and L-SiN, obtained by linearly fitting waveguide-length dependent transmission. The thickness of all waveguides is ~140 nm and the loss is measured at 638 nm. The inset in (a) shows the camera-recorded image of light propagating in a 1.0 cm-long spiral waveguide. (b) The micrograph of the transmission through a 8.0 cm-long waveguide.

## III. Waveguide loss @ λ = 1310 nm and λ = 1550 nm

Since transparency over a wide wavelength band is one of the main advantages of SiN photonics, it is important to examine the waveguide loss also at telecom wavelengths. We fabricated both H-SiN and L-SiN waveguides and characterize their losses in the 1260–1360nm wavelength range using a tunable laser source. While the designed thickness was ~400 nm, the fabricated samples had thicknesses of ~350 nm for H-SiN and ~450 nm L-SiN. Again we use single-mode lensed fibers optimized for 1550 nm, and the measured insertion loss for a single waveguide facet is ~3-3.5 dB. First we measure the loss for H-SiN and L-SiN films at a fixed wavelength of 1310 nm and show the results in Figure 2.25(a). Note that for H-SiN, the data of the waveguides with 0.8 μm design width is missing: the actual fabricated devices had a reduced width of ~0.65 μm and exhibited very high modal loss. The results show that, compared to the 638 nm or the 900 nm data, the loss decreases more gradually with increasing the width. We believe this can be attributed to the reduced impact of scattering at longer wavelength. At 2.0 μm width, we obtain a loss of 0.95 dB/cm and 1.24 dB/cm for H-SiN and L-SiN films, respectively. The small difference between both types of SiN films indicates that the intrinsic absorption is comparable within the measured spectrum. From numerical calculations, the upper cutoff width for single TE mode waveguide is ~1.5 μm and hence we can state that a loss of ~2.0 dB/cm in a single-mode waveguide for both SiN films has been attained.

We also investigate the waveguide loss over the whole O-band spectrum by sweeping the transmission from 1260-1360 nm. Figure 2.25(b) shows the transmission spectra of 1.5μm-wide waveguides of different lengths whereby the spectra are normalized to the reference waveguide to remove wavelength-dependent laser power and coupling responses. Note that there is a ~2 dB peak-to-peak amplitude variation of the transmission originating from the interference between transmitted and reflected (by cleaved facets and taper sections) beams (mainly 1st TE mode). It is clear that the transmission is almost flat over the whole spectrum and the reduction of transmission with increasing length shows negligible dependence on the wavelength. To illustrate this explicitly, we extract the waveguide loss simply using 1 cm and 8 cm transmission data and plot it versus wavelength in the inset of Figure 2.25(b) showing that the loss over the entire spectrum varies between 2.0–2.5 dB/cm. A similar behavior of waveguide loss versus wavelength is found for L-SiN. These results let us the conclude that there are no intrinsic absorption peaks within the O-band spectrum in our SiN deposited at either high or low temperature, making them suitable for passive integrated photonics at O-band wavelengths.

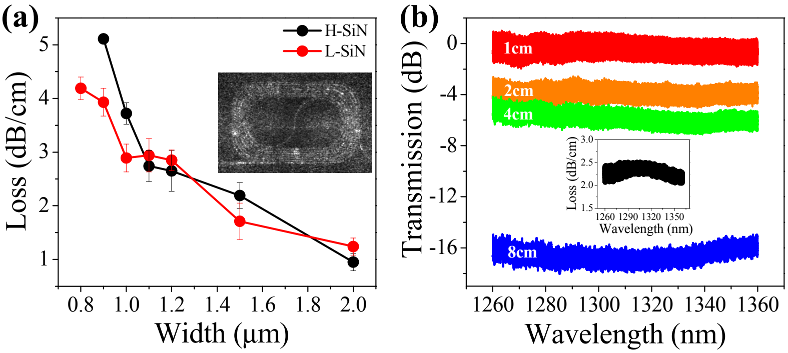

**Figure 2.25:** (a) Waveguide losses at different widths for H-SiN and L-SiN measured at 1310 nm, obtained by linearly fitting waveguide-length dependent transmission. The IR camera-recorded image in the inset illustrates the light propagating in a 1.0 cm long and 1.2 μm wide spiral waveguide. (b) The transmission spectra of 1.5 μm wide H-SiN waveguides of different lengths, normalized to the reference waveguide. The inset shows the wavelength dependent loss extracted from 1 cm and 8 cm waveguide lengths.

Last, we are also interested in the material absorption in PECVD SiN films around 1550 nm and the impact of the earlier mentioned hydrogen content on this absorption. Figure 2.26 presents the spectra of a ~1cm-long H-SiN waveguide before and after an annealing process. The data of an as-deposited SiN waveguide are recorded by using a broad infrared LED source (1450–1700 nm) and a tunable laser (1500–1630 nm) and both give nearly the same results. It is clearly seen that in the as-deposited SiN waveguide there is a prominent intrinsic absorption band with a width more than 70 nm centred at ~1520 nm. This absorption band is attributed to the second overtone absorption of the N-H stretching vibration. This material absorption can result in an additional waveguide loss of ~15 dB/cm. In fact, from the experimental data the loss above 1590 nm in as-deposited waveguide is comparable to that at 1310 nm. Thus the absolute waveguide loss would be around 16 dB/cm at 1520 nm. The material-absorption limited waveguide loss can be partially removed by an annealing process to reduce the content of hydrogen. We carried out two-hour annealing at 1000 °C in a nitrogen ambient for an as-deposited waveguide and record the transmission in Figure 2.26. Obviously, the absorption at the peak position is significantly reduced by a value of ~10 dB/cm, while the annealing doesn't change the properties away from the absorption band, for example from 1590 nm to 1630 nm. Although annealing results in a distinct improvement, the material loss in SiN due to hydrogen cannot be eliminated completely. Besides, annealing at high temperature also increases stress and creates cracks in the SiN film, resulting in low fabrication yields. Lastly, the material loss at ~1520 nm in PECVD SiN film can be reduced by optimizing the deposition conditions but that goes beyond the objectives of this thesis.

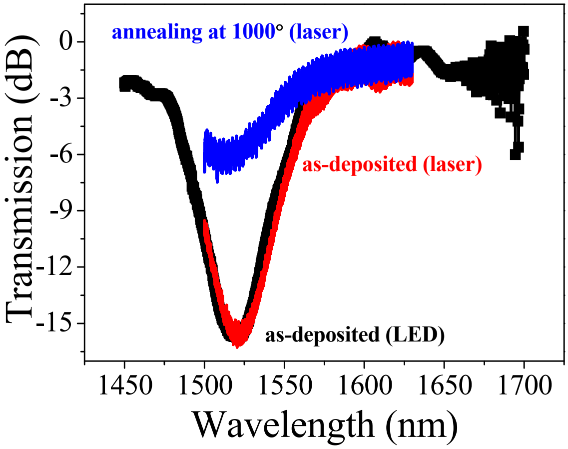

**Figure 2.26:** Transmission spectra of as-deposited and post-annealed 400 nm thick and 2 μm wide SiN waveguide with ~1 cm length. The spectra are recorded with a broad LED source and a tunable laser source and normalized to the associated source spectrum measured by tip-to-tip fiber coupling.

Finally, we summarize the losses for 2 μm wide waveguide measured at three wavelengths both for 270 °C and 120 °C SiN films in Table 2.1. For single TE mode waveguides, the losses are correspondingly ~1–2 dB/cm higher than those in 2 μm width for 900 nm and 1310 nm. It is believed that the loss levels at these wavelengths at least represent the wavelength bands of 600–900 nm and 1260–1360 nm. Further, given no intrinsic absorption mechanism has been reported in PECVD SiN between 900–1260 nm, we believe that low loss waveguides can be obtained from visible to O-band infrared wavelengths. In particular, we demonstrate that the fabrication of those waveguides can be carried out using conventional contact lithography and relatively low-temperature processes.

| Wavelength (nm) | Thickness (nm) | Width (μm) | Waveguide loss (dB/cm) | |
|---|---|---|---|---|
| | | | 270 °C | 120 °C |
| 638 | ~140 | 2 | 1.16 | 2.05 |
| 900 | ~200 | 2 | 0.94 | 1.88 |
| 1310 | 350–450 | 2 | 0.95 | 1.24 |

**Table 2.1:** The summary of waveguide losses at different wavelengths for PECVD SiN films deposited at 270 °C and 120 °C.

## 2.4 On-chip integrated high-Q SiN microdisk resonators

On-chip integrated microresonators like traditional optical cavities internally provide light confinement on a temporal and a spatial scale and potentially allow manipulations of photon lifetime and density. More importantly, the integrated resonators enable a controllable and easy exploitation of these unique properties of a resonator by on-chip coupling via waveguide wires. Because of the possibilities of mass fabrication and high reliability offered by using CMOS technology, on-chip microresonators are attractive for a wide range of fundamental studies and applications including cavity quantum electrodynamics, nonlinear optics, optomechanics, ultra-low threshold lasers, optical interconnect and communication, and optical sensing. In many fields, a high quality factor, an effective mode coupling scheme, and a compact cavity are highly desirable. In the context of SiN photonics, it remains a challenge to achieve these requirements due to the relatively low optical index contrast with respect to the substrate (commonly oxide), processing issues, and material absorption. In fact, by solving some of these problems, as mentioned before, other authors have demonstrated several types of SiN resonators with high Q factors but often required large dimensions.

In this section, on the basis of the previously developed low-loss SiN platform using a PECVD process at a relatively low temperature of 270 °C, we develop SiN waveguide-coupled high-Q SiN microdisks with radii of only a few micrometers by using a free-standing design and a vertical coupling scheme. We experimentally demonstrate an intrinsic Q factor of more than $1.5\times10^5$ together with a finesse of 2300 (free spectral range of ~30 nm) in a disk with only 15 μm diameter operating in the range of 1260–1360 nm and a Q factor of $1.2\times10^5$ in the 730–850 nm wavelength range. Furthermore, it is shown that the coupling strength between the disk resonator and the bus waveguide can be readily changed by tuning the parameters of the geometric configuration. We also show the ability to control the coupling between the bus waveguide and different radial modes of the disk resonator by taking advantage of the vertical coupling strategy. Our fabrication technique can be extended to LPCVD SiN films for the realization of ultra-high-Q and ultra-high-finesse waveguide-coupled microdisks operating over a broad spectrum, and we will also give some preliminary results on such devices.

### 2.4.1 Basics of microdisk resonators

Dielectric microdisks form an important class of optical microresonators and can support high-Q resonances, well-known as whispering gallery modes (WGMs), the name of which originates from the study of acoustic waves. These modes are confined by continuous total internal reflection along the periphery of the disk and can circulate in the cavity for a long time thus leading to high-Q factors. The WGMs can be found in several geometries typically with circular perimeters including microrings, microspheres, microtoroids, and cylinders. Among those microdisk and ring resonators are of great value in integrated cavities due to their compatibility with planar fabrication techniques.

The WGMs are a set of eigenstates of the electromagnetic (EM) field in a resonator system and their properties such as resonance frequency and mode structure can be in principle obtained by solving Maxwell's equations under given boundary conditions. However, in most realistic resonators it is impossible to accomplish this goal analytically and numerical methods are needed for accurate calculation. Here we give a brief theoretical description of WGMs as they occur in our disk structure and then introduce basic parameters for a microcavity. Consider a time-harmonic electromagnetic field $\mathbf{F} = \mathbf{F}(\mathbf{r})e^{-\mathrm{i}\omega t}$ with angular frequency $\omega$ where $\mathbf{F} = \{\mathbf{E}, \mathbf{H}\}$, in a source-free and homogeneous dielectric medium. Then Maxwell's equations can be simplified to the time-independent Helmholtz's wave equations:

$$\nabla^2\mathbf{F}(\mathbf{r}) + k_0^2 n^2(\mathbf{r})\mathbf{F}(\mathbf{r}) = 0, \tag{2.1}$$

where $k_0$ is the free-space wave number, $k_0 = \omega\sqrt{\varepsilon_0\mu_0} = \omega/c$ with $\varepsilon_0$ the permittivity, $\mu_0$ the permeability of free space and $c$ the speed of light in vacuum, and $n$ is the refractive index of the medium. In a thin microdisk, the modes only propagate in the disk plane and the finite vertical extension can be taken into account within the effective-index approximation [61, 62]. In this way, the problem is reduced to a two-dimensional one in which the modes can be separated to TE (E-field in the disk plane, H-field out of plane) and TM (H-field in the disk plane, E-field out of plane) polarizations and further obtained by solving the scalar wave equations for longitudinal field components. In the cylindrical coordinates ($r$, $\phi$, $z$) as shown in Figure 2.27(a), $H_z$ (TE) and $E_z$ (TM) are the components to be solved and using the method of separation of variables the solution can be expressed as following:

$$F_z(r,\phi,z) = R(r)\Phi(\phi)Z(z)\,, \tag{2.2}$$

where $F_z = \{E_z, H_z\}$. Thus Equation (2.1) can be separated as

$$\frac{d^2Z}{dz^2} + k_0^2(n^2 - n_{\text{eff}}^2)Z = 0\,, \tag{2.3}$$

$$\frac{d^2\Phi}{d\phi^2} + m^2\Phi = 0\,, \tag{2.4}$$

$$\frac{d^2R}{dr^2} + \frac{1}{r}\frac{dR}{dr} + (k_0^2 n_{\text{eff}}^2 - \frac{m^2}{r^2})R = 0\,, \tag{2.5}$$

where $n_{\text{eff}}$ is introduced as the effective index and $m$ is a constant, which will be determined by imposing a suitable boundary condition. Equation (2.3) gives the standard slab mode solutions and usually only the lowest order is relevant in a thin disk. Considering the rotational symmetry of the disk and therefore the periodicity condition, Equation (2.4) results in a set of eigenfunctions of the form $\Phi = \frac{1}{\sqrt{2\pi}} e^{\pm im\phi}$ with associated eigenvalue of $m$ being an integer, thus giving rise to the azimuthal mode number. The radial distribution is given by Equation (2.5) called the Bessel equation of the $m$-th order whose solutions are Bessel functions. Considering the wave function to remain finite inside the cavity and outgoing wave condition, the radial mode solution is given by

$$R(r) = \begin{cases} a_m J_m(k_0 n_{\text{eff}} r) & r \le R \\ b_m H_m^{(1)}(k_0 r) & r > R \end{cases}, \tag{2.6}$$

where $J_m$ is the Bessel function of the first kind and $m$-th order and $H_m^{(1)}$ is the modified Bessel function of the first kind and $m$-th order (also called the Hankel function of the first kind). Applying the boundary condition at the interface of disk and surroundings leads to a characteristic equation which determines a set of discrete eigenvalues of $n_{\text{eff}}$ and resonance frequencies $\omega_{nm}$ with $n$ denoting the $n$-th zero of the characteristic equation and associated with the radial mode number. Thus WGMs can be labeled with ($n$, $m$) in thin disk. Intuitively, $n$ gives the number of field maxima in the radial direction in disk and $m$ gives the number of wavelengths around the disk. Always the modes with lower $n$ but higher $m$ possess larger Q factors. Also note that due to rotational symmetry the modes ($\pm m$) are two-fold degenerate in frequency, corresponding to counterclockwise and clockwise traveling waves in the azimuthal direction.

The above mathematical analysis gives us a qualitative understanding of the WGMs in a simplified geometry. For a real three-dimensional disk, the modes will be quasi-TE and quasi-TM (hereafter still referred to as TE and TM) and the above theory cannot precisely calculate characteristic quantities of the WMG such as resonance frequency and quality factor, or even the coupling behavior for a complex structure. Therefore, numerical computing methods are required in photonic modeling and device design. We use both the commercial finite-difference time-domain (FDTD) solutions from Lumerical [63] and a freely available FDTD software package developed at MIT [64, 65]. The latter also supports cylindrical coordinates and thus simulates more efficiently for structures with axial symmetry such as the disk resonator. In Figure 2.27(b) we show a typical 1st order (fundamental) TE WGM profile in a SiN disk simulated with FDTD. For this mode $E_r$ is dominant and $m$=34 (34 periods for the oscillation of electric field around the perimeter of the disk). To illustrate the difference of the modes with different radial mode number, we also calculate the mode profiles of the 2nd and 3rd order radial TE modes and compare them with the 1st order mode in Figure 2.27(c). It is obvious that the number of field maxima ($|\mathbf{E}|^2$ has the same pattern and is not shown here) is equal to the radial order $n$ and that higher order radial modes are weakly confined manifested by a distinct radiation pattern, resulting in lower Q factors.

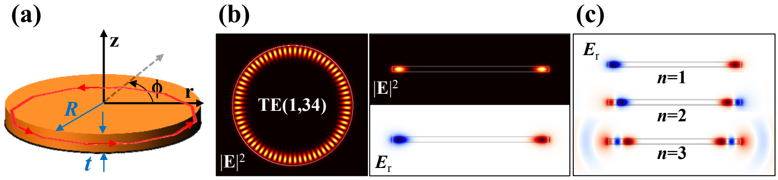

**Figure 2.27:** (a) Disk with radius $R$ and thickness $t$ in cylindrical coordinates. The red trajectory schematically depicts WGM. (b) FDTD simulated TE(1,34) WGM mode pattern in $r$-$\phi$ (left) and $r$-$z$ (right) planes of a SiN (index ~1.92) disk with $R$=5 μm and $t$=400 nm in air ($\lambda_{res}$~1300 nm). (c) TE WGMs of different radial orders of $n$=1, 2, 3. The $m$ number is chosen so that the resonance $\lambda_{res}$ is around 1300 nm. The Q factor are $1.6\times10^7$ ($n$=1), $1.6\times10^4$ ($n$=2), $1.6\times10^2$ ($n$=3).

The WGMs in a microdisk can be characterized by some basic parameters including the Q factor as already mentioned, free spectral range, finesse, and mode volume. These parameters can be obtained by simulation or by measurement.

## Q factor

In an ideal optical cavity, the mode oscillates inside at a deterministic frequency for infinitely long time. However, due to the dissipation of energy in a real cavity, the field of the mode decays with time and the extent of decay is measured by a dimensionless quantity, i.e., the Q-factor of the mode, which is defined as:

$$\frac{1}{Q}=\frac{P}{\omega_0 U}=\frac{1}{\omega_0 \tau}, \tag{2.7}$$

where $U$ is the EM energy stored in the cavity, $P$ is the outgoing power, $\omega_0$ is the resonance frequency and $\tau$ is the energy storage time (photon lifetime) [66]. From this definition, the EM energy within the cavity decays as $e^{-\gamma t}$ with $\gamma=1/\tau=\omega_0/Q$ and thus the field of the cavity mode oscillates with a complex frequency as $\mathbf{E} \propto e^{-\gamma t/2-\mathrm{i}\omega_0 t}$. The frequency distribution for the resonance power can be obtained by the Fourier transform of the time-varying field and is given by

$$\left|\mathbf{E}(\omega)\right|^2 \propto \frac{1}{(\omega-\omega_0)^2+(\omega_0/2Q)^2}. \tag{2.8}$$

Therefore, the resonant line shape of power has a Lorentzian peak in the frequency domain with a full width $\delta\omega$ at half-maximum and $\delta\omega=\omega_0/Q$. Thus the Q factor can also be expressed as

$$Q=\frac{\omega_0}{\delta\omega}\cong\frac{\lambda_0}{\delta\lambda}, \tag{2.9}$$

where $\lambda_0$ is the wavelength at resonance and $\delta\lambda$ is the full width of the wavelength-dependent line shape function. Since the Q factor defines a photon lifetime of $\tau=Q/\omega_0$ for the optical power to decay to $1/e$, the corresponding decay length $L$ is simply calculated as $L=c\tau/n_{\mathrm{eff}}$, where $n_{\mathrm{eff}}$ is the effective index of the mode[2]. Thus we can relate the Q factor to an effective absorption coefficient $\alpha=1/L$ as

$$Q=\frac{2\pi n_{\mathrm{eff}}}{\alpha\lambda_0}. \tag{2.10}$$

This expression is useful to calculate the Q factor for a given absorption coefficient.

---

[2] Sometimes, the group index $n_g$ of the mode is adopted instead. In the case SiN, the difference between $n_{\mathrm{eff}}$ and $n_g$ is small.

The Q factor of a resonant mode is determined by all loss mechanisms in the cavity, and according to the definition in (2.7) the overall Q can be written as $Q^{-1} = \sum_i Q_i^{-1}$, where $Q_i$ relates to the contribution of the $i$-th loss mechanism. In the case of a SiN disk, the total Q factor (also called loaded Q) consists of loss contributions such as modal loss (i.e. radiation loss), volume material absorption, scattering loss (both volume and surface), surface absorption (at interfaces), and external coupling loss (e.g. to a waveguide), given by

$$Q_{\mathrm{tot}}^{-1} = Q_{\mathrm{rad}}^{-1} + Q_{\mathrm{mat}}^{-1} + Q_{\mathrm{scat}}^{-1} + Q_{\mathrm{s.a.}}^{-1} + Q_{\mathrm{coup}}^{-1} = Q_{\mathrm{int}}^{-1} + Q_{\mathrm{ext}}^{-1}, \quad (2.11)$$

where $Q_{\mathrm{int}}$ (unloaded Q) excluding the coupling loss contribution is also referred to as the intrinsic Q factor. The radiation loss related $Q_{\mathrm{rad}}$ is inherent in WGMs due to incomplete confinement of photons by a curved reflection boundary and hence strongly depends on disk dimensions (approximately an exponential increase with growing radius) and index contrast. This Q factor can be calculated by using FDTD simulation. The material absorption limited $Q_{\mathrm{mat}}$ is universal and easily obtained using the expression (2.10). However, it is difficult to measure the material absorption coefficient with high accuracy in deposited SiN films due to its relatively small magnitude. The loss measurement of long waveguides, as performed previously, can give a good estimation of material loss, provided other losses in measured waveguides are negligible. The $Q_{\mathrm{scat}}$ due to volume scattering actually can be wrapped with material loss and assumed to be large enough. The scattering loss by surface roughness, however, is likely to be a main limitation for realizing high-Q integrated microresonators. For the surface, roughness comes from the fabrication process and remains challenging to be reduced. The surface absorption ($1/Q_{\mathrm{s.a.}}$) can be ignored in our disk. The $Q_{\mathrm{ext}}$ due to coupling between disk and waveguide is of practical importance in devices and can be readily tuned in the design. Finally, the total Q factor is determined through the expressions (2.7) or (2.9) and experimentally attained by exciting WGMs in the disk and measuring the response in the time or frequency domain. For example, obtaining a transmission spectrum by scanning the laser through a resonance is commonly used for measuring Q factors up to $10^8$, and will be employed in this thesis. Alternatively, the photon lifetime can be directly recorded in the time domain using a lifetime measurement set-up [67].

## Free spectral range, finesse, and mode volume

The WGMs in a disk have to satisfy a quantized resonance condition the same as the standing-wave condition in a Fabry–Pérot interferometer, given by

$$m\lambda = 2\pi R n_{\mathrm{eff}} \quad , \quad (2.12)$$

where $m$ is the azimuthal mode number, $\lambda$ is the resonance wavelength, $R$ is the geometrical radius of the mode, and $n_{\text{eff}}$ is the effective index of the mode. The free spectral range (FSR) is defined as the wavelength (frequency) spacing $\Delta\lambda$ ($\Delta\omega$) between adjacent WGM resonances. In weakly dispersive WGMs, we have $n_{\text{g}}(\lambda) = n_{\text{eff}}(\lambda) - \lambda\frac{\Delta n_{\text{eff}}(\lambda)}{\Delta\lambda}$, where $n_{\text{g}}$ is the group index. Then the FSR can be expressed as

$$\Delta\lambda = \frac{\lambda^2}{2\pi R n_{\text{g}}}, \quad \Delta\omega = \frac{c}{R n_{\text{g}}}. \tag{2.13}$$

Clearly, a smaller disk results in larger FSR. In practice, it is much easier to realize a small FSR, whereas it is much more difficult to achieve a larger one together with an acceptable Q factor although this is what is needed for important applications like single-mode operating lasers.

By combing the Q factor and the FSR, we can introduce an important figure of merit of a cavity, the finesse, defined as

$$\text{Finesse} = \frac{FSR}{\delta\lambda} = \frac{FSR \cdot Q}{\lambda}. \tag{2.14}$$

The finesse directly relates to some physical quantities in a cavity, for instance, the field enhancement factor in a cavity is proportional to the cavity finesse. It is always desirable to have a large finesse, intuitively meaning high Q in a relatively small disk, but it is challenging to achieve. To the best of our knowledge, the state-of-the-art finesses for on-chip integrated resonators (Si, SiN, …) are ~$10^4$ at ~1550 nm [17, 36] and ~$1.5\times10^3$ at ~650 nm [34, 35].

Apart from temporal confinement described by the Q factor, in many applications, the spatial confinement is equally important and is characterized by the mode volume ($V$). A common definition for the mode volume related to the energy density of the mode is given by

$$V = \frac{\int_v \varepsilon(\mathbf{r})\left|\mathbf{E}(\mathbf{r})\right|^2 d^3r}{\max\left(\varepsilon(\mathbf{r})\left|\mathbf{E}(\mathbf{r})\right|^2\right)}, \tag{2.15}$$

where the integral is performed over all space. This definition is interpreted as the equivalent occupying volume in which the whole energy of the mode is distributed homogeneously at the peak value. Clearly, the mode volume measures the extent of energy concentration on spatial scale and a small value implies a higher photon density in the cavity. This then leads to an increased light-matter interaction, which is critical in many studies such as nonlinear optics at a low power level, ultra-low threshold lasers and single-photon emitters based on the enhancement of spontaneous emission. In the disk, the mode volume shows an approximately linear dependence on the radius of the disk and a smaller disk obviously benefits the lower mode volume.

## On-chip waveguide coupling to microdisk

Most cavity parameters can be probed by the external excitation of WGMs in the cavity. Moreover, further exploitation of unique optical functions in an integrated cavity requires efficient and controlled excitation through co-integrated waveguides, which can provide robust and reproducible coupling to on-chip resonators. In this thesis, a simple waveguide-disk coupling design is adopted by using an evanescent coupling technique, as schematically shown in Figure 2.28. This design allows achievement of efficient and controllable coupling, due to natural phase matching of the modes in the SiN waveguides and disks and the implementation of a vertical coupling configuration as will be introduced later.

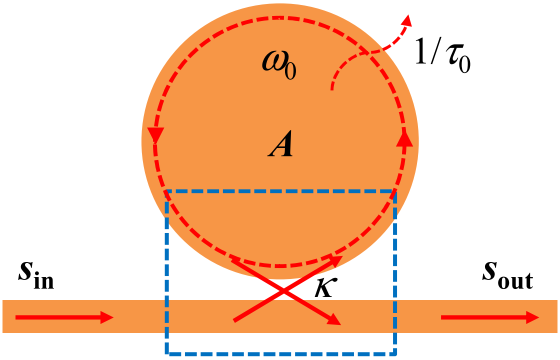

**Figure 2.28:** Schematics of a waveguide-coupled microdisk. The input single mode in a straight waveguide is coupled to a counterclockwise WGM in a disk.

For a weakly coupled cavity (Q factor is large enough, e.g., >100), the coupling behavior in the structure of Figure 2.28 can be described by the temporal coupled-mode theory [66, 68]. Consider a disk WGM of frequency $\omega_0$ and intrinsic lifetime $\tau_0$ (determined by the intrinsic $Q_{int}$), and a coupling lifetime $\tau_{ext}$ (determined by the $Q_{ext}$) with a single-mode bus waveguide, and also assume no parasitic losses at the coupling junction (e.g., back-reflection, scattering losses), we can write:

$$\frac{dA}{dt} = -(i\omega_0 + \frac{1}{2\tau_0} + \frac{1}{2\tau_{ext}})A + \kappa s_{in}, \tag{2.16}$$

$$s_{\text{out}} = s_{\text{in}} - \kappa A\,, \tag{2.17}$$

where $A$ is overall complex amplitude (giving both magnitude and phase) and is normalized so that $|A|^2$ is the cavity mode energy, $s_{\text{in}}/s_{\text{out}}$ are the input/output field amplitudes of the waveguide mode and $|s_{\text{in}}|^2$ is normalized to the input power, and $\kappa$ represents the strength of the cavity-waveguide coupling and $|\kappa| = \sqrt{1/\tau_{\text{ext}}}$. Assume the excitation of $s_{\text{in}} = e^{-\mathrm{i}\omega t}$, then the steady-state transmission through the waveguide is given by

$$T = \frac{|s_{\text{out}}|^2}{|s_{\text{in}}|^2} = 1 - \frac{4\tau_0\tau_{\text{ext}}}{(\omega-\omega_0)^2 + (\tau_0 + \tau_{\text{ext}})^2}\,. \tag{2.18}$$

Equation (2.18) results in a Lorentzian function and the loaded Q factor can be extracted by a fit of transmission peak/dip. Depending on the relation between intrinsic and external coupling decay rates, the transmission can be characterized by three coupling regimes.

(i) Under coupling: $\tau_0 < \tau_{\text{ext}}$, the waveguide coupling is weak and the cavity decay rate $1/\tau_0$ exceeds the coupling rate $1/\tau_{\text{ext}}$.

(ii) Critical coupling: $\tau_0 = \tau_{\text{ext}}$, the coupling loss is matched to the intrinsic cavity loss. In this case the power is completely transferred into the cavity mode (eventually dissipated out via intrinsic loss channels) and the transmission vanishes due to the destructive interference of the field coupled out of the cavity and the transmitted input field.

(iii) Over coupling: $\tau_0 > \tau_{\text{ext}}$, the coupling rate to the waveguide surpasses the intrinsic decay rate.

From Equation (2.18), a high Q factor is measured in the under- and critical-coupling regimes. Using Equations (2.7) and (2.11), the transmission at the resonance ($\omega=\omega_0$) can be expressed as:

$$T_0 = \left(\frac{2Q}{Q_{\text{int}}} - 1\right)^2, \tag{2.19}$$

where $Q$ is the loaded and also the measured Q-factor. This expression can be used to calculate the intrinsic Q factor from the transmission spectrum obtained in the under- or critical- coupling ($2Q > Q_{\text{int}}$).

### 2.4.2 Design and fabrication

Our waveguide-disk design is based on SiN platform and therefore the important condition of phase matching for the evanescent coupling is naturally satisfied. The cross sections of the disk and waveguide are designed as an ideal rectangle shape which can be perfectly produced using the previously developed etching process. As coupling geometry, due to several reasons we choose vertical coupling configuration in which the top free-standing SiN disk is vertically coupled to the bus SiN waveguide on the bottom as shown in Figure 2.29(a). A first consideration is that the space separation (i.e., coupling gap) between the waveguide and disk can be realized by a deposition step, rather than a lithographical definition and etching step used in lateral coupling. Thus the lithographic resolution limit is avoided and a coupling gap ranging from tens to hundreds of nanometers can be precisely controlled, and meanwhile the individual fabrication processes, especially in the disk layer, can be improved in terms of lithographic and etching uniformity due to the absence of interference effects among complex structures. Secondarily, the vertical coupling scheme makes it much easier to achieve a free-standing SiN disk by using aSi as sacrificed layer and subsequently an alkaline-based wet etching process, due to huge wet etching selectivity of aSi to SiN (even low temperature SiN). Third, the vertical coupling structure offers more degrees of freedom in the control the coupling strength via tuning vertical gap or horizontal offset. In particular, different maxima positions of radial order WGMs in disk as seen in Figure 2.27(c), potentially allows a respective control of the overlap of the evanescent fields of WGM and waveguide modes by changing underneath waveguide position or mode profile, making selective coupling among radial order modes possible. In a side-coupled design, however, coupling simultaneously occurs in all radial modes often featured in a complex transmission spectrum with all radial modes present. A further advantage of vertical coupling will be seen in the integration with active materials in Chapter 4.

In vertical coupling, surface planarity is a prerequisite for accomplishing high-quality lithography. Using previously developed CMP processes based on $SiO_2$ deposition or aSi deposition, we can have two designs of the device as shown in Figure 2.29(b) and (c). Since the aSi based CMP can provide extra spacing between disk and substrate, the WGM loss leaking to substrate is further reduced. Nevertheless, both will be used in passive SiN fabrication.

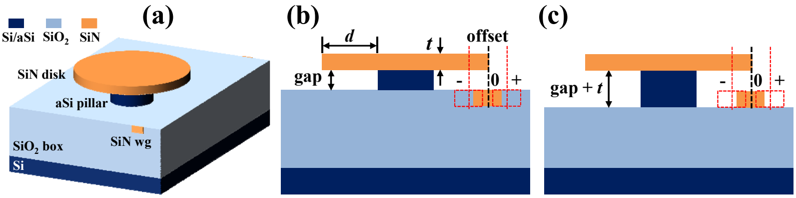

**Figure 2.29:** SiN disk-waveguide vertical coupling configuration. (a) Overview of the free-standing SiN disk supported on aSi pillar coupled to SiN waveguide planarized with $SiO_2$ CMP. (b) Cross-sectional view of the

coupling region of (a). (c) Cross-sectional view of another similar vertical coupling design but coupled to an air-cladded waveguide realized with aSi CMP.

## Design

The SiN waveguide and disk are designed for the O-band wavelengths because of the availability of a high-resolution tunable laser source. The design can be easily scaled to longer or shorter wavelengths and as an example a demonstration of a high-Q SiN disk operating in the 700–900 nm wavelength range will be given later in this chapter. First, we use a $SiO_2$ CMP process resulting in the device illustrated in Figure 2.29(a) and (b). The SiN disk is suspended on aSi pillar and vertically coupled to a straight bus SiN waveguide buried in a $SiO_2$ cladding with a smooth top surface. The parameters of the geometry are listed in Table 2.2.

| wg/disk thickness (*t*) | wg width | diameter (2*R*) | gap | offset | undercut (*d*) |
|---|---|---|---|---|---|
| 400nm | 0.8~1.5μm | 7~30μm | 150~700nm | -450 ~+450nm | >2.0μm |

**Table 2.2:** Structural parameters of the SiN waveguide-disk design.

Following FDTD simulations, we choose a thickness of 400 nm for both the waveguide and the disk layers, guaranteeing a fundamental TE mode with a low loss at ~1310 nm. The width of the bus waveguide is designed in the range of 0.8−1.5 μm with the actual fabricated width being ~0.6−1.4 μm. Below 1.4 μm, the waveguide perfectly operates in single TE mode and therefore only TE WGMs in the disk are excited. The diameter of the SiN disk is changed to study the properties of the WGMs such as Q factor, FSR, and coupling behavior of modes of different orders. The coupling gap, defined as the vertical spacing between the waveguide top and the disk bottom, is determined by the thickness of the aSi pillar and varies in the range of 150–700 nm. The horizontal offset is defined as the relative distance of the center of the bus waveguide with respect to the edge of the disk and varies from -450 nm to +450 nm with the bus waveguide moving away from the disk as schematically indicated in Figure 2.29(b). The undercut distance *d*, as shown in Figure 2.29(b) should be sufficiently deep to eliminate leakage of the TE WGMs to the aSi pillar. We performed a simulation of the Q factor ($Q_{rad}$) as a function of the undercut distance for the disk with a 15 μm diameter and 400 nm gap, as shown in Figure 2.30(a). It can be seen that the aSi pillar has negligible influence on the Q of the 1st radial TE modes in the disk when the undercut distance is above 2.0 μm (which is insufficient for higher order TE modes however, e.g., > 3.0 µm for 2nd TE WGMs). In Figure 2.30(b) we show the typical fundamental TE WGMs in a free-standing SiN disk. The mode is well confined in the SiN layer with little leakage loss to the substrate.

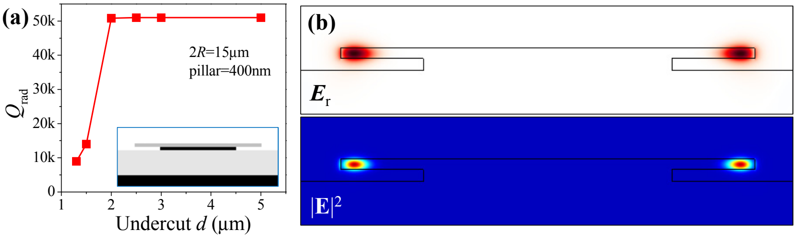

**Figure 2.30:** FDTD simulated Q factor of the 1st TE mode around 1300 nm for different undercut etch distance, with a fixed pillar of 400 nm height and a diameter of 15 µm for the disk SiN. Inset: simulated structure. (b) The 1st TE(1,53) mode profile of radial electric field and intensity for the disk with an undercut of 3 µm.

The influence of the substrate on the Q factor is further illustrated in Figure 2.31(a), which shows the Q factor as a function of aSi pillar height. The Q-factor nearly exponential grows with increasing the height (gap). From the mode distribution in Figure 2.31(b), it is clear that the mode of the SiN disk directly on the $SiO_2$ exhibits higher radiation loss to the substrate compared with that in a disk suspended over the substrate. Evidently, the free-standing design can enable high Q WGMs even in small disks.

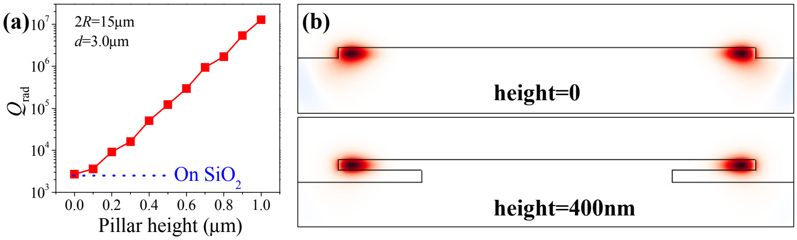

**Figure 2.31:** (a) Simulated Q factor of the 1st TE mode around 1300 nm as a function of aSi pillar height (gap) in a 15µm-diameter disk. (b) The electric field distribution of the modes with 0 and 400 nm height.

In Figure 2.32, we present the simulated Q factors for different disk diameters. The mode number (*n*,*m*) is chosen so that all resonances are around 1300 nm for comparison. It can be seen that the Q factors of the 1st and 2nd radial TE modes increase exponentially with the diameter, and the 1st modes have an average 1-2 orders higher Q than the 2nd modes. Besides, the 1st TM modes have an even lower Q than the 2nd TE modes.

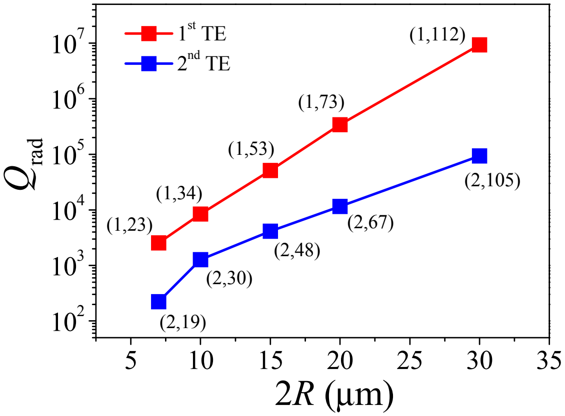

**Figure 2.32:** Simulated Q factors of the 1st and 2nd TE modes around 1300 nm as a function of disk diameter. The aSi pillar is set at 400 nm height and the undercut is 3.5 μm.

Last, we calculate the coupling strength between the bus waveguide and the disk by performing three-dimensional FDTD in which only the coupler region is simulated to calculate the power coupling efficiency ($\eta$) per round-trip. We hereby also exploit a mode-expansion technique integrated in Lumerical FDTD. We investigate the effect of waveguide width and offset on the coupling efficiency and plot the results in Figure 2.33. First, at a fixed offset, as shown in Figure 2.33(a) the $\eta$ of the 1st TE mode remains almost unchanged except for very narrow widths (in fact the waveguide is lossy below 650 nm width), while the $\eta$ of the 2nd TE mode exhibits an exponential decay with widening the width. Therefore, by using a wider waveguide, the higher order radial modes can be suppressed efficiently yet without changing the coupling strength for the 1st modes. In practice, the 1st order modes, which always have larger Q, can be excited firstly at critical-coupling regime accompanied by the maximum transmission extinction in the spectrum. At that point the higher order modes with lower Q are still far under coupled and thus barely excited. On the other hand, from Figure 2.33(b), the $\eta$ for both TE orders approximately decrease exponentially with increasing the offset, due to reducing field overlap of the modes. Thus an appropriate choice of offset can result in critical coupling for the 2nd order modes while the 1st order modes are already over coupled with the resulting shallow transmission dip. Consequently, we are able to achieve selective coupling between the WGMs of different orders. Note that there are still additional degrees of freedom in adjusting the coupling, such as the coupling gap, the thickness and shape of the bus waveguide.

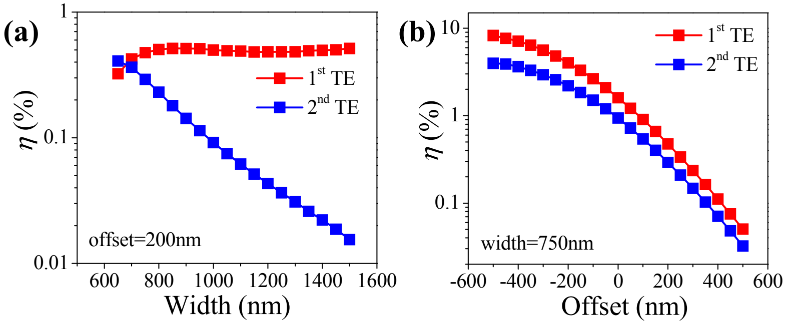

**Figure 2.33:** The simulated power coupling efficiency ($\eta$) per round-trip at ~1300 nm between fundamental TE waveguide mode and the 1st and 2nd TE WGMs in the 30μm-diameter disk, as a function of waveguide width (a) and offset (b). The gap is fixed at 400 nm and air-cladding waveguide is used.

## Fabrication

The SiN and $SiO_2$ are deposited using 270 °C PECVD, the aSi using 180°C PECVD, which results in a smooth surface. The previously optimized contact lithography and RIE processes are used throughout the fabrication. The mask is designed so that within a block of the die we can have a group of differently sized disks with each one coupled to different width waveguides at a fixed offset and then we repeat such block in one direction on the chip (perpendicular to the waveguide wires) with changing the offset to create the whole mask. In this way, the vertical alignment error between the waveguide and disk can be compensated by the offset as long as we have a large offset variation. The bus waveguide possesses a 200μm-long section of the designed width at the coupling region and is then tapered to 3.0 μm to reduce the waveguide loss and facilitate easier end-fire coupling. Figure 2.34 schematically shows the fabrication flow of the design with the $SiO_2$ CMP process. Firstly, a 400 nm thick SiN is deposited onto a 2.5×2.5 $cm^2$ Si chip with a 3 μm thermal $SiO_2$ box layer and then the bus waveguide is patterned by lithography and subsequently transferred onto the SiN layer by RIE to form a strip waveguide as shown in Figure 2.34(a). After waveguide fabrication, a 1.2 μm $SiO_2$ cladding is deposited and CMP is used to flatten the surface. Next, a gap layer of aSi and disk layer of 400 nm SiN are successively deposited on the planarized substrate. Then the top disk is fabricated, aligned with respect to the buried bus waveguide, as shown in Figure 2.34(d) and (e). Finally an alkaline-based wet etching is carried out to undercut the aSi and realize a free-standing SiN disk supported on the aSi pedestal as drawn in Figure 2.34(f). We show one typical fabricated result in Figure 2.35. The designed configuration of the device is well realized, demonstrating the suitability of our fabrication process to accomplish this integrated vertical coupling devices fabricated on chip scale.

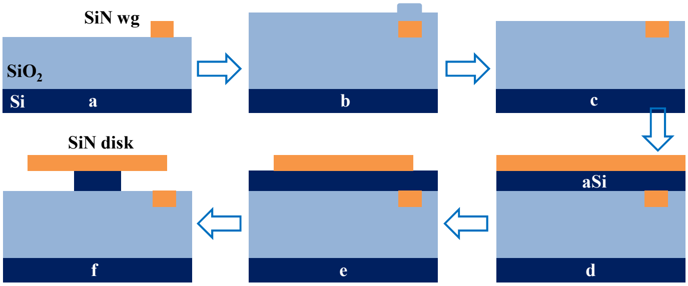

**Figure 2.34:** Schematics of the fabrication flow of SiN free-standing microdisk vertically coupled to on-chip waveguide. (a) Definition of SiN waveguide. (b, c) $SiO_2$ cladding deposition and CMP Planarization. (d, e) Deposition of aSi and SiN and definition of SiN disk. (f) Undercut etching of aSi.

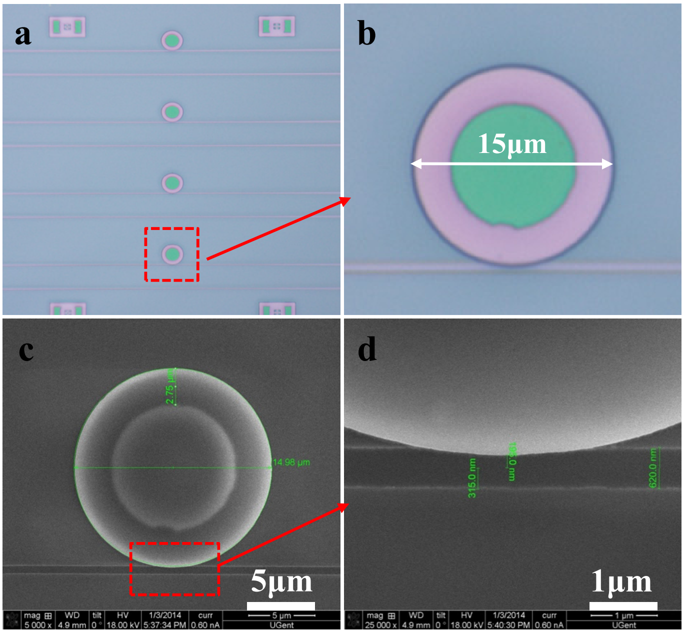

**Figure 2.35:** Fabricated SiN waveguide-disk coupled device with 15 µm diameter disk. (a) Optical images of an array of disk and (b) a selected disk. (c) SEM images of the disk and (c) enlarged view of the coupling region as indicated with the dashed red box in (c).

### 2.4.3 Characterization and discussion

The fabricated devices are characterized by taking transmission spectra from 1260 to 1360 nm. A tunable laser source is coupled to the cleaved facets of the bus waveguide on the same setup used for waveguide loss measurements. First, we characterized a chip with a measured aSi pillar of ~500 nm height and ~3.3 µm undercut. Both disk parameters and coupling tunability are characterized and discussed.

## Q factor of the disk

The fabricated devices are characterized by taking transmission spectra from 1260 to 1360 nm. A tunable laser source is coupled to the cleaved facets of the bus waveguide on the same setup used for waveguide loss measurements. The input power is set low enough (< -25 dBm) to avoid thermal effects. First, we characterized a chip with a measured aSi pillar of ~500 nm height and ~3.3 µm undercut. In Figure 2.36, we show the transmission of a set of disks with different radius coupled to waveguides of the same width at the fixed offset. Under these conditions, the smaller disks are under coupled due to their lower intrinsic Q while the larger ones are nearly critically coupled. Note that the background oscillation with 1.5–2 dB peak-to-peak amplitude, as seen from the inset in the spectrum of the 10µm-diameter disk, comes from the interference between transmitted and beams reflected by the facets. The transmission spectra clearly feature sharp dips at the WGM resonances and a flat transmission without parasitic insertion losses in the off-resonance regions. In addition, more than 20 dB maximum transmission extinction can be achieved near critical coupling. This shows our vertical coupling scheme provides an efficient way of exciting disk WGMs via an on-chip single-mode straight waveguide. The variation of the resonance wavelength on chip scale is less than 1.0 nm, implying excellent uniformity of the fabrication processes. In Figure 2.36, for smaller diameters, only the pure 1st order radial TE mode family is present in the spectra. For the 30µm-diameter disk, the 2nd radial mode family is also excited. In line with the simulations it exhibits a larger FSR and lower Q factor compared with the 1st order modes. In this way we can differentiate the 1st and 2nd order mode families in the transmission spectra, as denoted with the red and blue arrows, respectively in Figure 2.36.

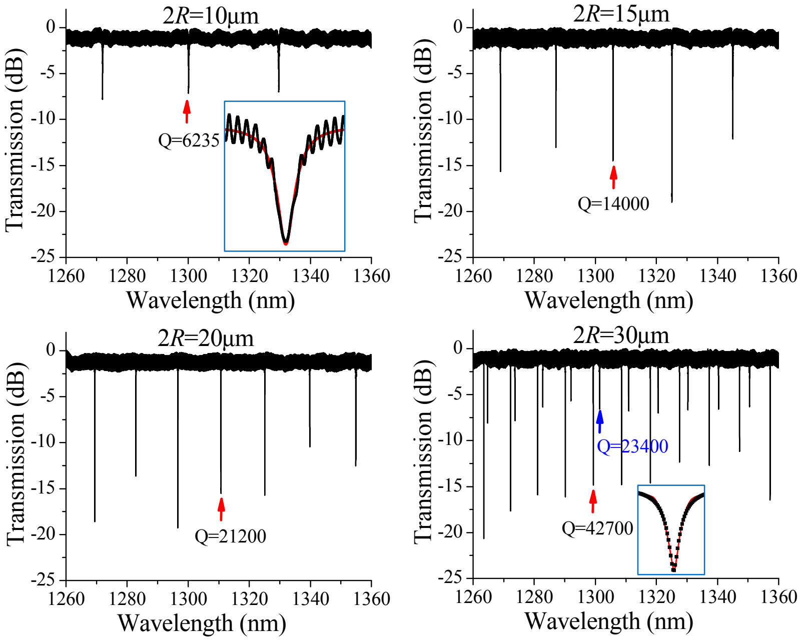

**Figure 2.36:** Normalized transmission spectra of the disks with different diameters of $2R$ = 10, 15, 20, 30 μm. The width of the bus waveguide is ~650 nm and the offset is around -120 nm. Red arrows designate the 1st TE WGMs with fitted Q factors. Blue arrow denotes the 2nd WGMs in 30 μm diameter.

By fitting a Lorentzian function, we can extract the loaded Q factors and from these calculate the intrinsic $Q_{\mathrm{int}}$ using Equation (2.19). They are plotted together with the finesse for different disk diameters in Figure 2.37(a) at the resonance of ~1300 nm. With increasing the diameter, both Q factor and finesse increase and reach the maximum values of $Q_{\mathrm{int}}=7.3\times10^4$ and finesse of 525 in the 30μm-diameter disk. For the smallest diameter of 7 μm, we still obtain a respectable Q factor of $3.7\times10^3$ and finesse of 120. Obviously, it is impossible to achieve these high qualities in a SiN disk which are not free-standing. To determine the limits for the Q factor, we come back to Equation (2.11) and assume the main contributions to the intrinsic Q in our disk are $Q_{\mathrm{rad}}$, $Q_{\mathrm{mat}}$, and $Q_{\mathrm{scat}}$. Consider the material loss of 1 dB/cm previously measured in a waveguide at 1300 nm, $Q_{\mathrm{mat}}$ is calculated to be around $3\times10^5$ using Equation (2.10). $Q_{\mathrm{rad}}$ can be obtained by simulation and $Q_{\mathrm{scat}}$ can then be extracted using Equation (2.11). We plot $Q_{\mathrm{scat}}$ and $Q_{\mathrm{rad}}$ in Figure 2.37(b). It can be seen that the $Q_{\mathrm{int}}$ in SiN disks of smaller diameters (<15 μm) is mainly limited by the scattering loss and radiation loss and that the scattering loss is dominant for larger disks. The scattering loss could be reduced by using even larger disks or improving the fabrication process, whereas the material loss will be the main limit of the Q factor in our PECVD SiN disk.

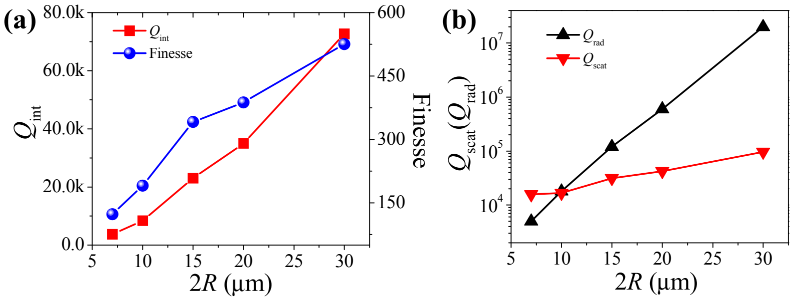

**Figure 2.37:** (a) Measured intrinsic Q factors and finesse of the 1st TE modes around 1300 nm as a function of disk diameter. (b) Extracted $Q_{\mathrm{scat}}$ and simulated $Q_{\mathrm{rad}}$ for different diameters.

## Tunability of the coupling between waveguide and disk

As shown in the simulation results, the coupling strength of WGMs can be tuned by changing the width of the bus waveguide or the offset, allowing operation in different coupling regimes. In particular, due to their differences in mode properties and coupling behaviors, selective coupling between different mode orders can be realized. In Figure 2.38 we show the evolution of the transmission of a 30μm-diameter disk with increasing the width of the bus waveguide. In the spectra, the 1st order modes remain almost unchanged due since the coupling strength is fairly independent of the bus width. By contrast, the transmission depth of the 2nd order mode family is substantially reduced when widening the bus waveguide and eventually becomes negligible for the 1110 nm wide bus waveguides. This removal of the higher order modes using wider waveguide arises from insufficient coupling strength and therefore these modes are far under coupled. Thus changing the dimension of the bus waveguide offers an effective way of exciting only fundamental WGMs in larger disks. Note that when the waveguide is wide enough to support higher order modes, the transmission spectrum will be contaminated by the inference of higher order waveguide modes that can be excited by input coupling or coupling from disk modes.

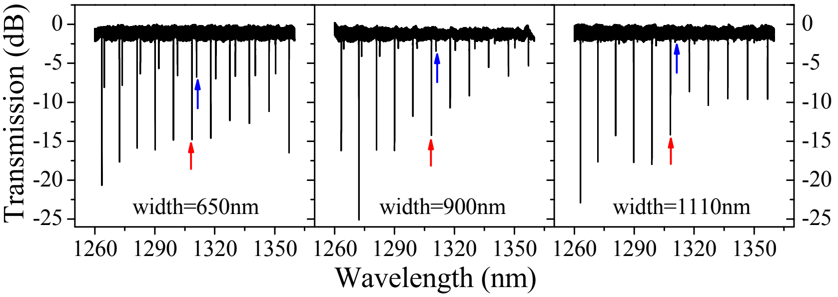

**Figure 2.38:** Normalized transmission spectra of the 30 μm diameter disk at the offset of -120 nm but different widths of the bus waveguides. Red and blue arrows designate the 1st and 2nd TE radial modes respectively.

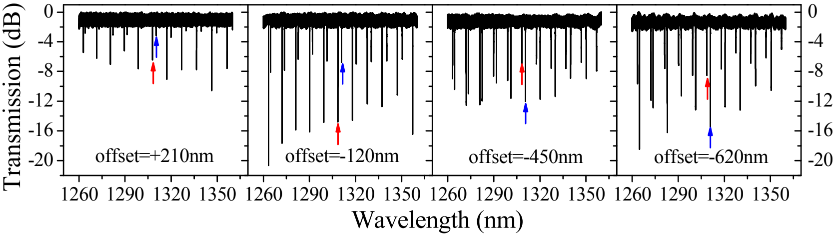

**Figure 2.39:** Normalized transmission spectra of the 30 μm diameter disk coupled to 650 nm bus waveguide at various coupling offsets. Red and blue arrows designate the 1st and 2nd TE radial modes respectively.

In Figure 2.39 we show the evolution of the transmission of a 30μm-diameter disk with changing the offset. It is obvious that when reducing the offset (i.e., moving the bus waveguide closer to the disk) the 1st TE mode family evolves from an under coupled to the critically coupled and eventually to the over coupled regime, with an overall transmission dip varying from 7 dB to 20 dB and back to 7 dB. On the other hand, the transmission depth of the 2nd order modes gradually increases when moving the waveguide closer to the disk, which indicates an increasing coupling strength for this mode family. For the offset of -620 nm, the second order modes reach nearly critical coupling. Therefore, the critical coupling condition occurs at different offset for both mode families, mainly due to significant difference in Q factors of different order modes. A proper choice of coupling offset allows to excite either a certain order mode of interest or a collection of modes of different orders, a clear advantage of the vertical coupling configuration.

### 2.4.4 Further improvement of device performance

The performance of the waveguide-disk coupled device can be improved on from two aspects. First, we can employ the design of Figure 2.29(c) and thus gain an extra spacing between disk and substrate to exponentially increase the radiation Q factors of WGMs as shown in Figure 2.31(a), in particular for small disks, while still keeping the same coupling gap between disk and waveguide. Additionally, it is found that the surface with direct CMP finish is much smoother than the as deposited aSi surface thus guaranteeing the definition of a more ideal disk geometry. The core of achieving such design relies on the aSi-based CMP process. Second, further optimizing the etch process can minimize scattering loss. This optimization using a reflow process for photoresist in lithography together with a slightly modified etching process was described previously.

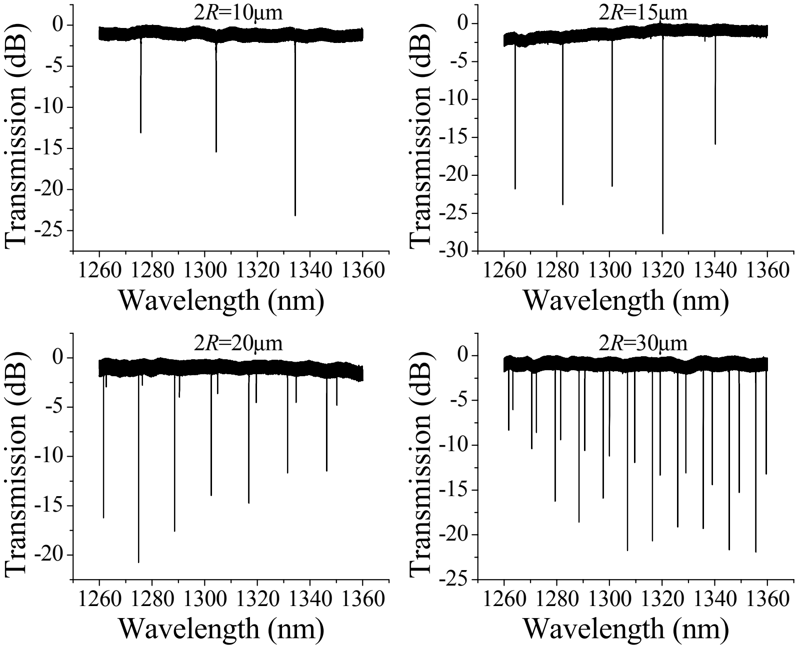

**Figure 2.40:** Transmission spectra of the disks fabricated with aSi-based CMP process. The coupling gap between disk and waveguide is ~460 nm. The width of bus waveguide is 880 nm and the offset is around -100 nm. The devices work at nearly critical-coupling regime.

The fabrication flow of the structure in Figure 2.29(c) is similar to the processes in Figure 2.34 but using a one-step aSi-based CMP process to replace the $SiO_2$-based CMP and aSi-deposition processes used before. In Figure 2.40, we show the measured transmission spectra of the disks fabricated with the aSi-CMP process, which have a similar mode structures as those made with the $SiO_2$ CMP design. However, the Q factor and finesse are notably improved, as shown in Figure 2.41(a). In the 15μm-diameter disk, we achieve a finesse of 2300 together with an intrinsic Q factor of $1.5\times10^5$, the state-of-the-art values in PECVD SiN resonators. For the smallest 7μm-diameter disk, the FSR is as large as 45 nm with a Q factor up to $2.7\times10^4$ which is limited by radiation and scattering losses as shown in Figure 2.41(b). The highest Q is measured in a 30μm-diameter disk with a record value of $2.5\times10^5$ which almost reaches the limitation imposed by the material loss of 1 dB/cm ($Q_{\mathrm{mat}}=3\times10^5$). This is also confirmed by the saturation of the Q when further increasing the diameter of disk. On the other hand, from Figure 2.41(b) the $Q_{\mathrm{scat}}$ is dramatically improved by more than one order of magnitude compared with the results in Figure 2.37(b). In the 30μm-diameter disk, we realize a $Q_{\mathrm{scat}}$ up to $1.5\times10^6$, suggesting it is possible to make even higher performance microdisks if we would use a low-loss SiN material. To prove this we used a 300 nm LPCVD SiN layer (from TriPleX$^{\mathrm{TM}}$ technology) for disk fabrication with a slightly modified RIE etching condition of gases of $CF_4/H_2/SF_6$ = 80sccm/7sccm/3sccm, a pressure of 20mTorr, and a RF power of 210 W. We achieved a Q of $3.0\times10^5$ in a 30μm-diameter in the first test, as shown in Figure 2.42. Higher Q is expected by using thicker or larger disks and by optimizing the etch processes for LPCVD SiN. We believe the combination of the current processing technique with LPCVD SiN will make it possible to realize on-chip waveguide-coupled microresonators with ultra-high Q, ultra-high finesse, and low mode volume.

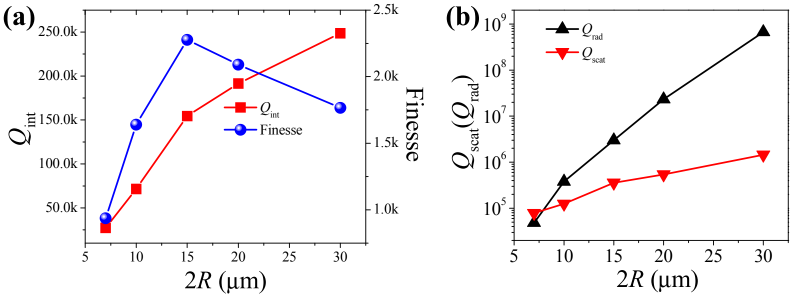

**Figure 2.41:** (a) Measured intrinsic Q factors and finesse of the 1st TE modes around 1300 nm as a function of disk diameter. (b) Extracted $Q_{\mathrm{scat}}$ and simulated $Q_{\mathrm{rad}}$ for different diameters.

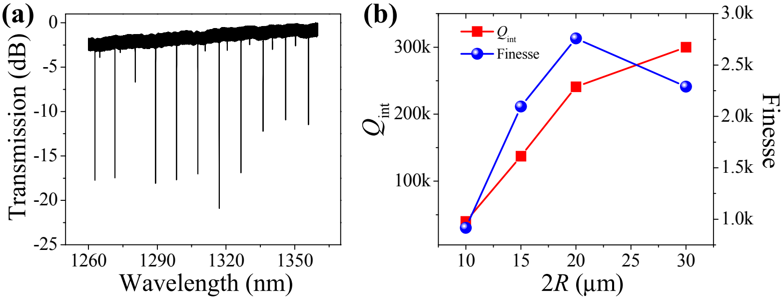

**Figure 2.42:** (a) Transmission spectrum of a LPCVD SiN disk with 30 μm diameter fabricated with aSi CMP. (b) Measured intrinsic Q factors and finesse of the 1st TE modes around 1300 nm for the disks fabricated in 300 nm LPCVD SiN.

Finally, it should be added that the splitting of the transmission dip is also observed in our measurement. This splitting, commonly encountered in high-Q WGM resonators, arises from scattering-induced intermode coupling of two degenerate eigenmodes – counterclockwise and clockwise traveling WGMs [69, 70]. The mode splitting can result in variations of dip depth over the transmission spectrum due to the change of the coupling condition.

### 2.4.5 Scaling working wavelength beyond 1310 nm

The design and fabrication of vertically waveguide-coupled disks can be easily scaled to other wavelengths. Taking the SiN material loss and available tunable laser sources into account we explore the performance of SiN microdisks in the wavelength range of 700–900 nm. The waveguide thickness is set at ~150 nm to ensure single-mode operation and the disk thickness is set at ~200 nm to support high-Q WGMs. As a demonstration we present the transmission spectrum around 745 nm of a 15μm-diameter disk in Figure 2.43. We obtain an intrinsic Q of $5\times10^4$ with ~400 finesse, the best results reported in PECVD SiN resonators for visible or near infrared. Higher Q up to $1.2\times10^5$ is achieved in larger disks. The main limitation in Q consists of material and scattering losses.

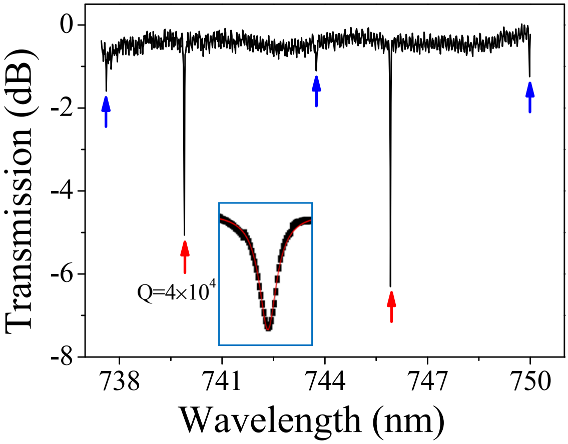

**Figure 2.43:** Transmission spectrum of the disk with 15 μm diameter fabricated with aSi CMP. The width of bus waveguide is ~510 nm and the coupling gap is ~300 nm. The disk is under coupled. Red and blue arrows designate the 1st and 2nd TE radial modes respectively.

Last, it is also of interest to characterize these disks in the telecom wavelengths around 1550 nm, although the material loss of PECVD SiN becomes large as shown previously. We present the transmission of a 30μm-diameter disk from 1500 nm to 1630 nm in Figure 2.44(a). Clearly the absorption at ~1520 nm results in extra 9 dB insertion loss and the intrinsic Q of the mode nearby is $1.8\times10^4$, compared with the Q of $7\times10^4$ for the mode at 1600 nm. Considering two main contributions to $Q_{\mathrm{int}}$ – radiation loss ($Q_{\mathrm{rad}}$) and material absorption ($Q_{\mathrm{mat}}$) and using Equations (2.10) and (2.11), we extract the material loss for all 1st TE family modes in the spectrum and plot the result in Figure 2.44(b). The maximum loss is ~15 dB/cm at ~1520 nm, very close to our estimated result from waveguide measurement. Beyond the absorption band, e.g., at 1600 nm, the loss is at the level of 3 dB/cm. Nevertheless, high-Q microdisks working at 1550 nm can be realized simply by using low-loss LPCVD SiN and for the first test we demonstrate a Q up to $10^5$ and a finesse of 1200 in a 20μm-diameter disk with 300 nm thickness. Higher performances are definitely realizable in future demonstrations.

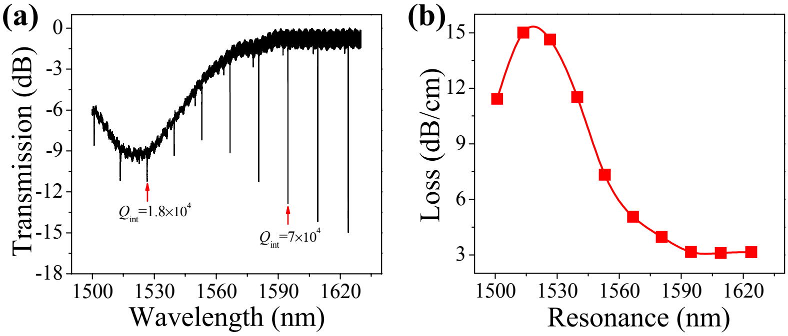

**Figure 2.44:** (a) Transmission spectrum of the SiN disk with 30 μm diameter in the same chip characterized in Figure 2.40. The width of bus waveguide is 1100 nm and the offset is around 200 nm. The disk is under coupled. (b) Extracted material loss for the 1st TE family modes in (a).

## 2.5 Conclusion

We have developed a SiN photonics platform CMOS compatible technology steps. By thoroughly optimizing the fabrication processes for SiN deposition and contact lithography, and particularly for dry etching of SiN, we achieved low-loss waveguides of ~1 dB/cm for the wavelengths ranging from 600 nm to 1360 nm in PECVD SiN deposited at relatively low-temperature from 120 °C to 270 °C. On the basis of the developed SiN platform, we further designed and realized vertically waveguide-coupled free-standing SiN microdisks exploiting a unique design and the developed processes. High-Q factors ($2.5\times10^5$ at 1310 nm) and large finesses (2300 at 1310 nm) have been demonstrated in these compact on-chip microresonators from the visible to the O-band telecom wavelengths, representing the state-of-the-art performance in integrated PECVD SiN resonators. Moreover, we demonstrated that our design scheme and fabrication technology for integrated free-standing SiN disks can be extended to LPCVD SiN films, thus potentially allowing for the realization of ultra-high-Q, ultra-high-finesse, and low-mode-volume integrated SiN microresonators operating over even broader spectral bands.

The current processing techniques for SiN will certainly provide valuable and universal guidance for future development of SiN-based photonics. The demonstrated high-performance SiN-photonics building blocks can be readily used in practical applications such as optical interconnect, nonlinear optics, optomechanics, and on-chip optical sensing. The developed technologies also form the base for the development of active SiN devices through the combination with active materials as will be described in subsequent chapters.

# References

[1] J. Bauer, "Optical-Properties, Band-Gap, and Surface Roughness of $Si_3N_4$," physica status solidi (a) **39**(2), 411-418 (1977).

[2] H. R. Philipp, "Optical Properties of Silicon Nitride," J. Electrochem. Soc. **120**(2), 295-300 (1973).

[3] C. E. Morosanu, "The Preparation, Characterization and Applications of Silicon Nitride Thin Films," Thin Solid Films **65**(2), 171-208 (1980).

[4] F. H. P. M. Habraken, ed. *LPCVD Silicon Nitride and Oxynitride Films: Material and Applications in Integrated Circuit Technology* (Springer, 1991).

[5] W. A. Lanford and M. J. Rand, "The hydrogen content of plasma-deposited silicon nitride," J. Appl. Phys. **49**(4), 2473-2477 (1978).

[6] V. J. Kapoor, R. S. Bailey, and H. J. Stein, "Hydrogen-Related Memory Traps in Thin Silicon-Nitride Films," Journal of Vacuum Science & Technology a-Vacuum Surfaces and Films **1**(2), 600-607 (1983).

[7] F. H. P. M. Habraken, "Characterization of LPCVD and PCVD Silicon Oxynitride Films," Appl. Surf. Sci. **30**(1-4), 186-196 (1987).

[8] C. M. M. Denisse, K. Z. Troost, F. H. P. M. Habraken, W. F. Vanderweg, and M. Hendriks, "Annealing of Plasma Silicon Oxynitride Films," J. Appl. Phys. **60**(7), 2543-2547 (1986).

[9] F. H. P. M. Habraken and A. E. T. Kuiper, "Silicon Nitride and Oxynitride Films," Materials Science & Engineering R-Reports **12**(3), 123-175 (1994).

[10] J. Yota, J. Hander, and A. A. Saleh, "A comparative study on inductively-coupled plasma high-density plasma, plasma-enhanced, and low pressure chemical vapor deposition silicon nitride films," Journal of Vacuum Science & Technology a-Vacuum Surfaces and Films **18**(2), 372-376 (2000).

[11] C. H. Henry, R. F. Kazarinov, H. J. Lee, K. J. Orlowsky, and L. E. Katz, "Low loss $Si_3N_4$–$SiO_2$ optical waveguides on Si," Appl. Opt. **26**(13), 2621-2624 (1987).

[12] F. Bruno, M. Delguidice, R. Recca, and F. Testa, "Plasma-Enhanced Chemical Vapor Deposition of Low-Loss SiON Optical Waveguides at 1.5-μm Wavelength," Appl. Opt. **30**(31), 4560-4564 (1991).

[13] T. Inukai and K. Ono, "Optical Characteristics of Amorphous Silicon Nitride Thin-Films Prepared by Electron Cyclotron Resonance Plasma

Chemical Vapor Deposition," Jpn. J. Appl. Phys., Part 1 **33**(5A), 2593-2598 (1994).

[14] F. Ay and A. Aydinli, "Comparative investigation of hydrogen bonding in silicon based PECVD grown dielectrics for optical waveguides," Opt. Mater. **26**(1), 33-46 (2004).

[15] S. C. Mao, S. H. Tao, Y. L. Xu, X. W. Sun, M. B. Yu, G. Q. Lo, and D. L. Kwong, "Low propagation loss SiN optical waveguide prepared by optimal low-hydrogen module," Opt. Express **16**(25), 20809-20816 (2008).

[16] http://www.lionixbv.nl/triplexmpw.html

[17] K. Luke, A. Dutt, C. B. Poitras, and M. Lipson, "Overcoming $Si_3N_4$ film stress limitations for high quality factor ring resonators," Opt. Express **21**(19), 22829-22833 (2013).

[18] W. Stutius and W. Streifer, "Silicon nitride films on silicon for optical waveguides," Appl. Opt. **16**(12), 3218-3222 (1977).

[19] S. Dutta, H. E. Jackson, J. T. Boyd, R. L. Davis, and F. S. Hickernell, "$CO_2$-Laser Annealing of $Si_3N_4$, $Nb_2O_5$, and $Ta_2O_5$ Thin-Film Optical-Waveguides to Achieve Scattering Loss Reduction," IEEE J. Quantum Electron. **18**(4), 800-806 (1982).

[20] S. Sriram, W. D. Partlow, and C. S. Liu, "Low-loss optical waveguides using plasma-deposited silicon nitride," Appl. Opt. **22**(23), 3664-3665 (1983).

[21] D. A. P. Bulla, B. H. V. Borges, M. A. Romero, N. I. Morimoto, and L. G. Neto, "Design and fabrication of $SiO_2/Si_3N_4$ integrated-optics waveguides on silicon substrates," IEEE Trans. Microwave Theory Tech. **50**(1), 9-12 (2002).

[22] N. Daldosso, M. Melchiorri, F. Riboli, M. Girardini, G. Pucker, M. Crivellari, P. Bellutti, A. Lui, and L. Pavesi, "Comparison among various $Si_3N_4$ waveguide geometries grown within a CMOS fabrication pilot line," J. Lightwave Technol. **22**(7), 1734-1740 (2004).

[23] M. Melchiorri, N. Daldosso, F. Sbrana, L. Pavesi, G. Pucker, C. Kompocholis, P. Bellutti, and A. Lui, "Propagation losses of silicon nitride waveguides in the near-infrared range," Appl. Phys. Lett. **86**(12), 121111 (2005).

[24] M. J. Shaw, J. Guo, G. A. Vawter, C. Habermehl, and C. T. Sullivan, "Fabrication techniques for low loss silicon nitride waveguides,"

Micromachining Technology for Micro-Optics and Nano-Optics III **5720**, 109-118 (2005).

[25] F. Morichetti, A. Melloni, M. Martinelli, R. G. Heideman, A. Leinse, D. H. Geuzebroek, and A. Borreman, "Box-shaped dielectric waveguides: A new concept in integrated optics?," J. Lightwave Technol. **25**(9), 2579-2589 (2007).

[26] J. F. Bauters, M. J. R. Heck, D. John, D. X. Dai, M. C. Tien, J. S. Barton, A. Leinse, R. G. Heideman, D. J. Blumenthal, and J. E. Bowers, "Ultra-low-loss high-aspect-ratio $Si_3N_4$ waveguides," Opt. Express **19**(4), 3163-3174 (2011).

[27] J. F. Bauters, M. J. R. Heck, D. D. John, J. S. Barton, C. M. Bruinink, A. Leinse, R. G. Heideman, D. J. Blumenthal, and J. E. Bowers, "Planar waveguides with less than 0.1 dB/m propagation loss fabricated with wafer bonding," Opt. Express **19**(24), 24090-24101 (2011).

[28] J. P. Epping, M. Hoekman, R. Mateman, A. Leinse, R. G. Heideman, A. van Rees, P. J. M. van der Slot, C. J. Lee, and K. J. Boller, "High confinement, high yield $Si_3N_4$ waveguides for nonlinear optical applications," Opt. Express **23**(2), 642-648 (2015).

[29] A. Gorin, A. Jaouad, E. Grondin, V. Aimez, and P. Charette, "Fabrication of silicon nitride waveguides for visible-light using PECVD: a study of the effect of plasma frequency on optical properties," Opt. Express **16**(18), 13509-13516 (2008).

[30] S. Romero-Garcia, F. Merget, F. Zhong, H. Finkelstein, and J. Witzens, "Silicon nitride CMOS-compatible platform for integrated photonics applications at visible wavelengths," Opt. Express **21**(12), 14036-14046 (2013).

[31] A. Z. Subramanian, P. Neutens, A. Dhakal, R. Jansen, T. Claes, X. Rottenberg, F. Peyskens, S. Selvaraja, P. Helin, B. Du Bois, K. Leyssens, S. Severi, P. Deshpande, R. Baets, and P. Van Dorpe, "Low-Loss Singlemode PECVD Silicon Nitride Photonic Wire Waveguides for 532-900 nm Wavelength Window Fabricated Within a CMOS Pilot Line," IEEE Photonics J. **5**(6)(2013).

[32] N. Sherwood-Droz and M. Lipson, "Scalable 3D dense integration of photonics on bulk silicon," Opt. Express **19**(18), 17758-17765 (2011).

[33] P. E. Barclay, K. Srinivasan, O. Painter, B. Lev, and H. Mabuchi, "Integration of fiber-coupled high-Q SiNx microdisks with atom chips," Appl. Phys. Lett. **89**(13), 131108 (2006).

[34] E. S. Hosseini, S. Yegnanarayanan, A. H. Atabaki, M. Soltani, and A. Adibi, "High Quality Planar Silicon Nitride Microdisk Resonators for Integrated Photonics in the Visible Wavelength Range," Opt. Express **17**(17), 14543-14551 (2009).

[35] E. S. Hosseini, S. Yegnanarayanan, A. H. Atabaki, M. Soltani, and A. Adibi, "Systematic design and fabrication of high-Q single-mode pulley-coupled planar silicon nitride microdisk resonators at visible wavelengths," Opt. Express **18**(3), 2127-2136 (2010).

[36] Q. Li, A. A. Eftekhar, M. Sodagar, Z. X. Xia, A. H. Atabaki, and A. Adibi, "Vertical integration of high-Q silicon nitride microresonators into silicon-on-insulator platform," Opt. Express **21**(15), 18236-18248 (2013).

[37] M. Khan, T. Babinec, M. W. McCutcheon, P. Deotare, and M. Loncar, "Fabrication and characterization of high-quality-factor silicon nitride nanobeam cavities," Opt. Lett. **36**(3), 421-423 (2011).

[38] M. C. Tien, J. F. Bauters, M. J. R. Heck, D. T. Spencer, D. J. Blumenthal, and J. E. Bowers, "Ultra-high quality factor planar $Si_3N_4$ ring resonators on Si substrates," Opt. Express **19**(14), 13551-13556 (2011).

[39] F. Ramiro-Manzano, N. Prtljaga, L. Pavesi, G. Pucker, and M. Ghulinyan, "A fully integrated high-Q Whispering-Gallery Wedge Resonator," Opt. Express **20**(20), 22934-22942 (2012).

[40] D. T. Spencer, J. F. Bauters, M. J. R. Heck, and J. E. Bowers, "Integrated waveguide coupled $Si_3N_4$ resonators in the ultrahigh-Q regime," Optica **1**(3), 153-157 (2014).

[41] K. Ikeda, R. E. Saperstein, N. Alic, and Y. Fainman, "Thermal and Kerr nonlinear properties of plasma-deposited silicon nitride/silicon dioxide waveguides," Opt. Express **16**(17), 12987-12994 (2008).

[42] J. S. Levy, A. Gondarenko, M. A. Foster, A. C. Turner-Foster, A. L. Gaeta, and M. Lipson, "CMOS-compatible multiple-wavelength oscillator for on-chip optical interconnects," Nat. Photonics **4**(1), 37-40 (2010).

[43] T. J. Kippenberg, R. Holzwarth, and S. A. Diddams, "Microresonator-Based Optical Frequency Combs," Science **332**(6029), 555-559 (2011).

[44] R. Halir, Y. Okawachi, J. S. Levy, M. A. Foster, M. Lipson, and A. L. Gaeta, "Ultrabroadband supercontinuum generation in a CMOS-compatible platform," Opt. Lett. **37**(10), 1685-1687 (2012).

[45] D. J. Moss, R. Morandotti, A. L. Gaeta, and M. Lipson, "New CMOS-compatible platforms based on silicon nitride and Hydex for nonlinear optics," Nat. Photonics **7**(8), 597-607 (2013).

[46] M. Eichenfield, R. Camacho, J. Chan, K. J. Vahala, and O. Painter, "A picogram- and nanometre-scale photonic-crystal optomechanical cavity," Nature **459**(7246), 550-U579 (2009).

[47] G. S. Wiederhecker, L. Chen, A. Gondarenko, and M. Lipson, "Controlling photonic structures using optical forces," Nature **462**(7273), 633-U103 (2009).

[48] M. A. Zhang, G. S. Wiederhecker, S. Manipatruni, A. Barnard, P. McEuen, and M. Lipson, "Synchronization of Micromechanical Oscillators Using Light," Phys. Rev. Lett. **109**(23), 233906 (2012).

[49] I. A. Young, E. Mohammed, J. T. S. Liao, A. M. Kern, S. Palermo, B. A. Block, M. R. Reshotko, and P. L. D. Chang, "Optical I/O Technology for Tera-Scale Computing," IEEE J. Solid-State Circuits **45**(1), 235-248 (2010).

[50] J. Pfeifle, V. Brasch, M. Lauermann, Y. M. Yu, D. Wegner, T. Herr, K. Hartinger, P. Schindler, J. S. Li, D. Hillerkuss, R. Schmogrow, C. Weimann, R. Holzwarth, W. Freude, J. Leuthold, T. J. Kippenberg, and C. Koos, "Coherent terabit communications with microresonator Kerr frequency combs," Nat. Photonics **8**(5), 375-380 (2014).

[51] X. G. Tu, J. F. Song, T. Y. Liow, M. K. Park, J. Q. Yiying, J. S. Kee, M. B. Yu, and G. Q. Lo, "Thermal independent Silicon-Nitride slot waveguide biosensor with high sensitivity," Opt. Express **20**(3), 2640-2648 (2012).

[52] A. Dhakal, A. Z. Subramanian, P. Wuytens, F. Peyskens, N. Le Thomas, and R. Baets, "Evanescent excitation and collection of spontaneous Raman spectra using silicon nitride nanophotonic waveguides," Opt. Lett. **39**(13), 4025-4028 (2014).

[53] P. Muellner, E. Melnik, G. Koppitsch, J. Kraft, F. Schrank, and R. Hainberger, "CMOS-compatible $Si_3N_4$ Waveguides for Optical Biosensing," Procedia Engineering **120**, 578-581 (2015).

[54] http://www.microchemicals.com/downloads/application_notes.html

[55] R. A. Morgan. *Plasma etching in semiconductor fabrication* (Elsevier, 1985).

[56] D. M. Manos and D. L. Flamm, *Plasma etching: an introduction* (Elsevier, 1989).

[57] J. W. Coburn and H. F. Winters, “Plasma etching—A discussion of mechanisms,” Journal of Vacuum Science & Technology **16**(2), 391-403 (1979).

[58] J. W. Coburn, “Insitu Auger-Electron Spectroscopy of Si and $SiO_2$ Surfaces Plasma Etched in $CF_4$-$H_2$ Glow-Discharges,” J. Appl. Phys. **50**(8), 5210-5213 (1979).

[59] M. Gupta, V. K. Rathi, R. Thangaraj, O. P. Agnihotri, and K. S. Chari, “The Preparation, Properties and Applications of Silicon-Nitride Thin-Films Deposited by Plasma-Enhanced Chemical Vapor-Deposition,” Thin Solid Films **204**(1), 77-106 (1991).

[60] B. De Geyter, K. Komorowska, E. Brainis, P. Emplit, P. Geiregat, A. Hassinen, Z. Hens, and D. Van Thourhout, “From fabrication to mode mapping in silicon nitride microdisks with embedded colloidal quantum dots,” Appl. Phys. Lett. **101**(16), 161101 (2012).

[61] M. Borselli, T. J. Johnson, and O. Painter, “Beyond the Rayleigh scattering limit in high-Q silicon microdisks: theory and experiment,” Opt. Express **13**(5), 1515-1530 (2005).

[62] H. Cao and J. Wiersig, “Dielectric microcavities: Model systems for wave chaos and non-Hermitian physics,” Rev. Mod. Phys. **87**(1), 61-111 (2015).

[63] https://www.lumerical.com/

[64] A. F. Oskooi, D. Roundy, M. Ibanescu, P. Bermel, J. D. Joannopoulos, and S. G. Johnson, “MEEP: A flexible free-software package for electromagnetic simulations by the FDTD method,” Comput. Phys. Commun. **181**(3), 687-702 (2010).

[65] http://ab-initio.mit.edu/wiki/index.php/Meep

[66] J. D. Joannopoulos, S. G. Johnson, J. N. Winn, and R. D. Meade, *Photonic crystals: molding the flow of light* (Princeton University Press, 2011).

[67] D. K. Armani, T. J. Kippenberg, S. M. Spillane, and K. J. Vahala, “Ultra-high-Q toroid microcavity on a chip,” Nature **421**(6926), 925-928 (2003).

[68] H. A. Haus, *Waves and fields in optoelectronics* (1983).

[69] M. L. Gorodetsky, A. D. Pryamikov, and V. S. Ilchenko, “Rayleigh scattering in high-Q microspheres,” Journal of the Optical Society of America B-Optical Physics **17**(6), 1051-1057 (2000).

[70] T. J. Kippenberg, S. M. Spillane, and K. J. Vahala, “Modal coupling in traveling-wave resonators,” Opt. Lett. **27**(19), 1669-1671 (2002).

# 3

# Development of patterning technique for QDs

To develop active photonics devices using colloidal semiconductor quantum dots (QDs), often a patterning technique for registering QDs in predefined active regions is required. Since QDs are mostly synthesized and stabilized as colloidal dispersions in solution while the processing of photonics devices is performed on a planar solid substrate, it remains challenging to transfer a solid film of QDs with well-defined geometrical shape and position to a substrate. Moreover, deterministically positioning QDs at the single-dot level becomes a highly desired tool in not only fundamental studies but also real device applications such as integrated single-dot emitters for single-photon sources based on QDs, as currently being investigated in our group.

In this chapter, we aim for developing a versatile and straightforward technique of pattering QDs on solid substrates on nanoscale and single-dot levels. This patterning technique allows for further applicability in the context both of fundamental studies and development of novel optoelectronic devices using QDs, for instance, precisely and efficiently locating a single QD for optical or electrical excitation and integrating with photonic building blocks.

## 3.1 Introduction to patterning of QDs

Semiconductor QDs have emerged as a novel class of materials of high scientific and technological interest, due to their unique electrical and optical properties. Combined with their suitability for solution-based processing, which makes them compatible with a wide range of existing material technologies, this makes for an ideal platform for fundamental studies in nanoscience and a wide variety of potential applications such as light-emitting diodes, photodetectors, lasers, and biosensing. Whereas colloidal QDs are synthesized as colloidal dispersions, multiple applications need QD films with different requirements in terms of film area, thickness, and patterning. As a result, the geometrically controlled deposition of QD mono- and multilayers is an essential step for exploiting their unique properties in practical applications. For instance, the quantitative analysis of the interaction between active QDs and photonic components such as optical waveguides [1, 2], resonators [3-5], and surface plasmons [6] requires well-controlled pattern shape and accurate placement of QDs integrating with passive photonics. Well-controlled approaches to deposit QDs in nanoscale patterns can also enable QD-based devices such as light-emitting diodes, photodetectors, modulators, or sensors to be further miniaturized and eventually integrated on photonic chips.

Parallel to application development, the investigation of QD properties at the single-dot level has become of significant importance to deepen the understanding of some of their fundamental optoelectronic properties and their interaction with external environments. Seminal studies have addressed the dynamical and spectral properties of single QDs, either through photoexcitation or via tunneling spectroscopy [7-15] and their coupling to microcavities [16], plasmonic nanocavities [17], or optical antennas [18-21]. The QD properties these investigations revealed, such as single photon emission [7, 8, 16] and tunable radiation by coupling with photonic building blocks [18-21], may eventually promote the development of single-QD based devices, such as single photon sources and controlled quantum emitters. Currently, most of the achieved investigations with single QDs rely either on randomly deposited QDs combined with careful localization of target devices around targeted QDs, or on directly patterning QDs close to the predefined structures. Both the random approach and existing direct-patterning approaches of QDs, however, have very low yield of localizing single QDs and lack an accurate control over the QD position, thus limiting the experimental efficiency and hampering the development of single-QD devices. Therefore, one of the biggest challenges for single-QD studies, and eventually for single-QD devices, is the ability to position a single QD at a predefined location with an accuracy of a few tens of nanometers or less.

Various approaches to deposit QDs in micrometer- and nanometer-sized patterns have been proposed in literature, using such methods as optical lithography combined with Langmuir–Blodgett (LB) deposition [22], direct electron-beam lithography (EBL) on LB films [23] or combined with a lift-off process [24-26], electrostatic self-assembly techniques [27, 28], and lithography assisted by surface functionalization [3, 20]. However, despite the significant progress made in patterning QDs, the technique still remains to be improved in terms of the control over patterning geometry and dimension, and the quality of the patterned layer. For instance, in most demonstrated experiments for QDs pattering, it remains a challenge to achieve the uniform and contamination-free patterns that applications will eventually need. Moreover, little approaches have demonstrated a straightforward and high yield positioning of individual QD. Often, downscaling a methodology to single QD positioning leads to significant complications due to the extremely small size of QDs and single QD deposits typically come together with ill-defined QD patches.

Here, we introduce an EBL-based technique for the formation of nanopatterned QD monolayers providing excellent control over the pattern structure and maintaining a well-defined QD surface density in the monolayers. By combining photoresist patterning by EBL, LB deposition of a QD monolayer and an optimized lift-off process, we demonstrate QD patterns with feature sizes down to ~30 nm and with arbitrary predefined shapes. The patterned QD monolayer exhibits sharp edges and the process leaves the monolayer and the blank substrate free of residues. Moreover, we show that the same approach applies to the formation of single QD patterns with a single-QD deposition yield as high as 40%. Importantly, the approach relies on methodologies compatible with standard solid-state pre- and postprocessing steps that can be applied on large area substrates. A numerical model describing the statistical behavior of the QD deposition process is developed and shows excellent agreement with the experimental results. The nano- and single-QD patterning technology proposed here not only provides a powerful tool for the fundamental studies of QDs but also represents a significant step toward optoelectronic devices based on QD nanopatterns and, eventually, single QDs.

## 3.2 Methodologies

Figure 3.1 schematically illustrates the proposed processing scheme. Firstly, using EBL we define the desired pattern in a diluted ZEP 520A resist film with an initial thickness of ~40 nm. Any possible residues are removed using a few seconds of oxygen plasma. If a thinner resist film is needed, the oxygen plasma is applied for longer time. Next a close-packed monolayer of QDs is formed through a LB machine (Nima 312D) and then transferred onto the patterned substrate, by pulling the substrate out of the LB trough. We use oleic acid passivated CdSe/CdS core/shell QDs synthesized[3] by a seeded-growth flash approach [29] with a diameter of ~10 nm and a central emission peak of ~650 nm. Finally, a lift-off process is carried out and the resist is removed from the substrate leaving the patterned QDs behind. The quality of the QD pattern is examined by a high-resolution scanning electron microscope (SEM) (FEI Nova 600) and photoluminescence (PL) characterization on a micro-PL setup.

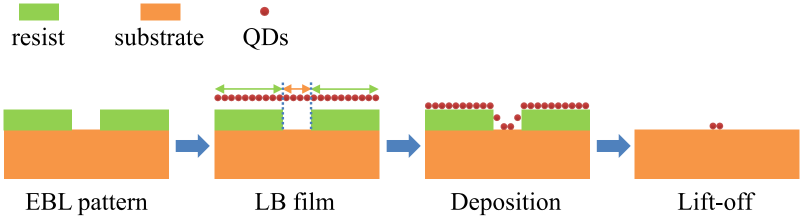

**Figure 3.1:** Schematics of the experimental flow of the patterning of QDs.

The formation of close-packed and residue-free QD-film patterns down to nanoscale dimensions relies upon several key processes including high-resolution EBL, deposition of a high quality QD LB-film onto a patterned substrate, and a clean lift-off process.

## 3.2.1 High-resolution EBL in thin resist film

As shown in Figure 3.1, the dimension of the final QD pattern is directly determined by the EBL pattern. More importantly, the thickness of the resist should be thin enough to minimize edge effects during transferring of the QD film onto a patterned substrate as we will further analyse in detail. In the experiment, we use diluted ZEP 520A positive resist and oxygen plasma to control the thickness of the resist in the range of 15 to 40 nm. The exposure dose in EBL is optimized to define nanoscale patterns of various shapes and feature sizes. In Figure 3.2 we show the various defined patterns in a ~33 nm thick resist. In particular, the hole patterns with a minimum diameter of ~30 nm are defined in dot-exposure mode in our EBL system and they will be employed for the investigation of single-dot patterning.

---

[3] The synthesis was carried out by Dr. Raquel Gomes of the UGent PCN group.

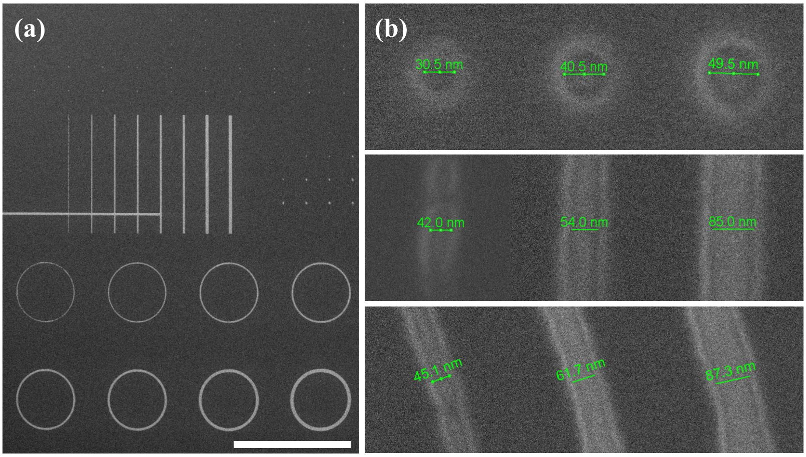

**Figure 3.2:** (a) SEM images of EBL patterns of various shapes with a resist thickness of ~33 nm. The scale bar is 10 µm. (b) Enlarged views of the patterns of hole (top panel), line (middle panel), and ring (bottom panel), with different feature sizes.

### 3.2.2 LB QD film deposition on the patterned substrate

There are several ways to form a QD solid film from the solution phase including simple spin-coating and the LB technique [22]. In comparison with spin-coating, the LB deposition of QDs used here provides better control of both the quality and the exact thickness of the QD film. With spin-coating, whereby the QD film is formed directly from the solution by evaporating the solvent, it is impossible to obtain a uniform layer of QDs and the resultant film is typically either submonolayer in nature or consists of areas with multilayers of varying thickness. Spinning QDs on a patterned substrate unavoidably results in over deposition of QDs near steps or a discontinuous film around pattern edges. As a result the subsequent lift-off process is made difficult by the limited amount of solvent seeping through the accumulated QD layer near steps or the film might completely peel off from the patterned areas. In contrast, the LB technique allows preparing a highly uniform monolayer of QDs over large areas, even when these are not completely flat, as long as the height variations are sufficiently gradual. When depositing the LB film onto a patterned substrate with sharp edges, the film around the patterned location will bend and break up as schematically indicated in Figure 3.1, resulting in exposed sidewalls favorable for the subsequent lift-off process. On the other hand, due to the additional area associated with the sidewalls, the QD density within the area of the pattern will be smaller than that of a closed packed film as illustrated in Figure 3.1. This effect is illustrated by SEM images of the substrate after QD deposition but before resist lift-off, as shown in Figure 3.3. It can be seen that the resist is covered by an undisturbed LB film up to the pattern edges whereas part of the QDs within the pattern stick to the resist sidewalls.

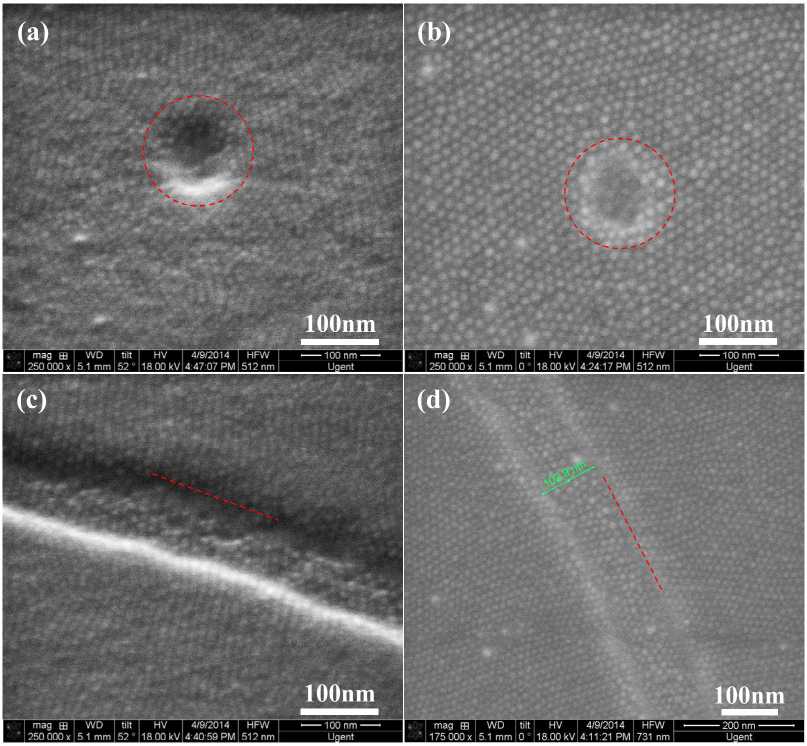

**Figure 3.3:** SEM images of as-deposited QD-film morphology after LB process on resist patterns with a thickness of ~33 nm. Tilted and top views for a hole pattern (a, b) and a trench pattern (c, d), respectively. The red dashed circles in (a, b) indicate the hole, and the lines in (c, d) indicate the edge of the trench.

### 3.2.3 Optimization of the lift-off process

Obviously, to minimize the above described edge effect the resist thickness needs to be thinned down. However, there is a trade-off between reducing the thickness of the resist and establishing an effective lift-off process without residues: the thicker the resist, the easier and cleaner the lift-off, and vice versa. When the thickness of the resist becomes comparable to the size of the QDs, lifting off QDs from the substrate becomes nearly impossible since all openings are covered by the close-packed QD film and no dissolvent can seep into the resist to start of the lifting process. More importantly, because of the strong van der Waals' interaction [22] between the QDs and the substrate, the lifted QDs can redeposit on the substrate from the dissolvent, an effect much more notable for thinner resists. Therefore, an efficient lift-off procedure turns out to be critical in obtaining a contaminant-free patterning and the associated threshold thickness for the resists needs to be determined.

In previous work whereby LB-deposited QD films were patterned using optical lithography photoresist films with a thickness of ~1.0 μm were used. For such a relative thick photoresist redeposition of QDs on the substrate can be avoided, even when using simple acetone as the dissolvent [22]. In recent work, it was shown that using EBL resist with a thickness of tens of nanometers spin coated diluted QDs can be lifted off albeit still with redeposition of QDs for very thin resist [26]. In our test as shown in Figure 3.4(a, b), pure acetone cannot lift off a QD LB-film deposited on resist with a thickness below ~1 μm. This is believed to originate from the high quality of the LB-film, which is more compact than the spin coated film. To develop a lift-off process that is compatible with thin resist layers and that does not leave undesired residual QDs on the substrate, we prepared a mixture of acetone and toluene as dissolvent for efficient lifting off QDs on thin resist. It is well known that acetone, widely used for cleaning and lifting-off most optical and EBL resists, is a polar solvent. As such it cannot form a stable and homogeneous suspension for typical QDs passivated with organic ligands, due to their nonpolar functional groups. On the other hand, toluene is commonly used as a nonpolar solvent for dispersing QDs in an extremely stable suspension. Hence, a mixture of acetone and toluene can exploit their respective relevant functionalities: dissolving the resist by acetone and stabilizing the lifted QDs by toluene, preventing redeposition of QDs on the substrate. The ratio of the two solvents has to be optimized in order to obtain a fairly moderate dissolution rate for the resist and to provide a sufficient stabilization of the removed QDs by the surrounding solvent, avoiding immediate attachment of the lifted QDs onto the substrate. However, simply rinsing the substrate in the mixture of acetone and toluene (e.g., a 1:2 volume-ratio of acetone to toluene), is not sufficient: there is almost no lift-off QDs and most of them are still redeposited on the substrate as shown in Figure 3.4(c). This could be understood by the fact that the in-situ released QDs can still immediately attach to the substrate before entering into the solvent. To prevent this, we employ a mild ultrasonic treatment to take the lifted QDs away from the substrate and subsequently to stabilize them in the solvent, and this approach is demonstrated to be very effective as shown in Figure 3.4(d), which uses the same solvent ratio as in Figure 3.4(c). Still, there are some residual QDs left for an aceton:toluene volume ratio of 1:2. When changing the ratio to 1:4 however, an almost residue-free pattern can be achieved as shown in Figure 3.4(e). When further increasing the relative amount of toluene, for instance with a 1:10 ratio of acetone to toluene, the redeposition of QDs becomes again significant as seen in Figure 3.4(f), due to the now very slow dissolution rate for the resist. Therefore, in summary we experimentally determine that the optimal solvent ratio of acetone to toluene is around 1:4 for an efficient and clean lift-off process.

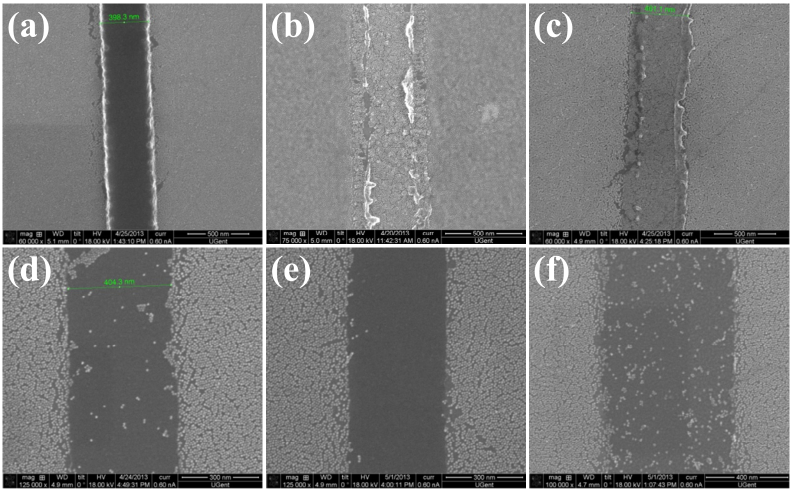

**Figure 3.4:** Optimization of lift-off process. (a) SEM image of the QD LB-film as deposited on the resist pattern substrate. (b) Lift-off result by rinsing with pure acetone. (c) Lift-off result by rinsing with a mixture of acetone and toluene (using a 1:2 volume ratio of acetone to toluene). (d-f) Lift-off results by using an ultrasonic in acetone and toluene with different volume ratios of 1:2, 1:4, and 1:10, respectively.

Based on the optimized solvent, we further investigate the threshold thickness of the resist for successful lift-off without residual QDs. We patterned the substrates with the same mask but with different resist thicknesses of 16, 22, and 30 nm and then carried out the LB deposition and lift-off process in the mixture of acetone and toluene with a ratio of 1:4. In Figure 3.5, we show the SEM results after the lift-off process for different resist thicknesses. It is clearly seen that there are some random residual QDs redeposited in the area outside of the patterned region for the 16 nm thick film while all residues can be eliminated for films thicker than 22 nm. Actually, the threshold thickness was determined to be even lower, at ~20 nm for the used QDs with ~10 nm diameter. It is believed that this threshold thickness depends on several factors such as the size of the QDs and the type of surface ligands. As a rule of thumb, a resist pattern with a thickness double that of the diameter of the QDs including passivating oleic acid ligands can be effectively lifted off without redeposition (in association with the optimized 1:4 ratio of acetone to toluene mixture as described above).

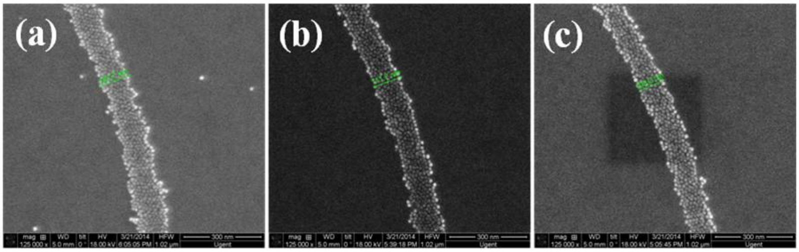

**Figure 3.5:** Determination of the threshold thickness of resist. SEM images after lifting off the resist with the thicknesses of (a) 16 nm, (b) 22 nm, and (c) 30 nm. Lift-off process was carried out by using an ultrasonic in the mixture of acetone and toluene with a volume ratio of 1:4.

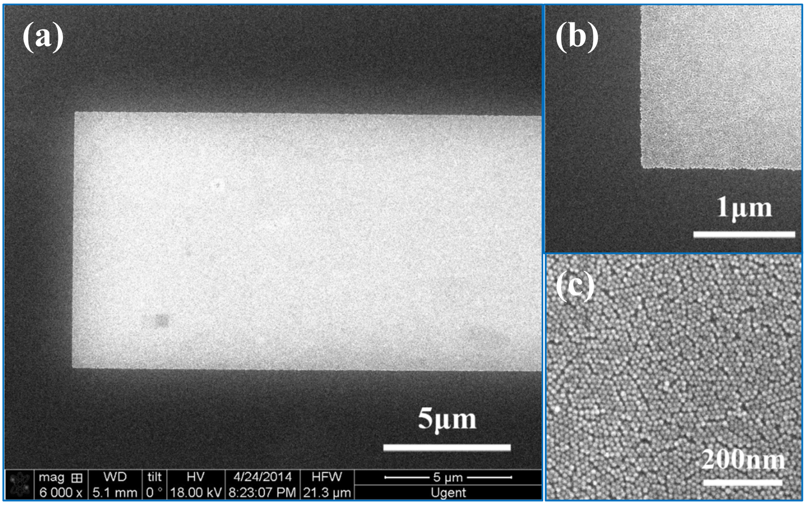

**Figure 3.6:** SEM images of the microscale patterns of LB QD film after lift-off. (a) Overall view of the pattern, (b) zoom-in view of the corner of the pattern, and (c) high-resolution view of LB QD film.

To verify the quality of the QD film prepared using the above process, firstly we patterned a ~23 nm thick resist layer deposited on a silicon substrate with microscale feature size and then carried out the lift-off process. Figure 3.6 shows the result, indicating that the LB technique allows transferring a uniform monolayer of QDs onto the patterned substrate and that the lift-off process works efficiently without leaving any unwanted residual QDs or resist. The excellent performance of the lift-off process can clearly be seen in Figure 3.6(b), where the enlarged SEM image of the corner of the pattern distinctly shows a sharp boundary between the monolayer of QDs and the lifted area, without peeling off the patterned QDs. Figure 3.6(c) presents the morphology of the QD film at higher magnification, showing a nearly close-packed film except for a few tiny voids within the film, possibly caused by the size dispersion of the QDs or small aggregations in the QD solution. It can also be learned that the QD film can be well preserved after our lift-off process, thanks to the sufficient adhesion of QDs to the substrate.

## 3.3 Nanoscale patterning

Using the optimized lift-off process and a resist thickness near the previously determined threshold value, we achieve nanoscale patterning of QD films. In Figure 3.7, we show patterning results with various shapes and different feature sizes. First, we patterned the QDs in lines and crossings with various widths, ranging from 30 to 250 nm, as shown in Figure 3.7(a) and (b). The lift-off process is demonstrated to be efficient for nanoscale patterns down to 30 nm feature size without any observable redeposition of free QDs or tearing of patterns. Moreover, it can be seen that the LB deposition is capable of transferring the QD film to the substrate through a 30 nm trench pattern in a 20 nm thick resist film, although as the magnified view for the 30 nm design in Figure 2b shows there is an evident loss of QDs because of the non-negligible sidewall effect in the narrowest trenches. In fact, it appears that the breaking up of the LB film by the resist sidewalls randomizes the QD deposition at the pattern edges. This probably reflects the dominance of QD–substrate interactions over QD–QD interparticle interactions [30]. As can be seen at the top of the 31 nm strip shown in Figure 3.7(b), this can favor the deposition of QDs as individual entities on the resist sidewalls or the substrate over the systematic assembly of QDs in 2D or even 3D aggregates.

In patterns of 60 nm and wider on the other hand, a nearly perfect closed-packed film is formed, implying that the quantity of QDs can be actually determined, very important for the quantitative study of QD properties and their interaction with the environment. To verify preservation of the PL in the QDs, we carried out micro-PL measurements on the patterned QDs. The result shown in the inset of Figure 3.7(a) clearly indicates that the emission properties of the QDs are well preserved after LB deposition and the lift-off process, verifying further study is indeed of practical value. Similarly, we successfully patterned QDs in microring shapes with different widths as can be seen Figure 3.7(c) and (d).

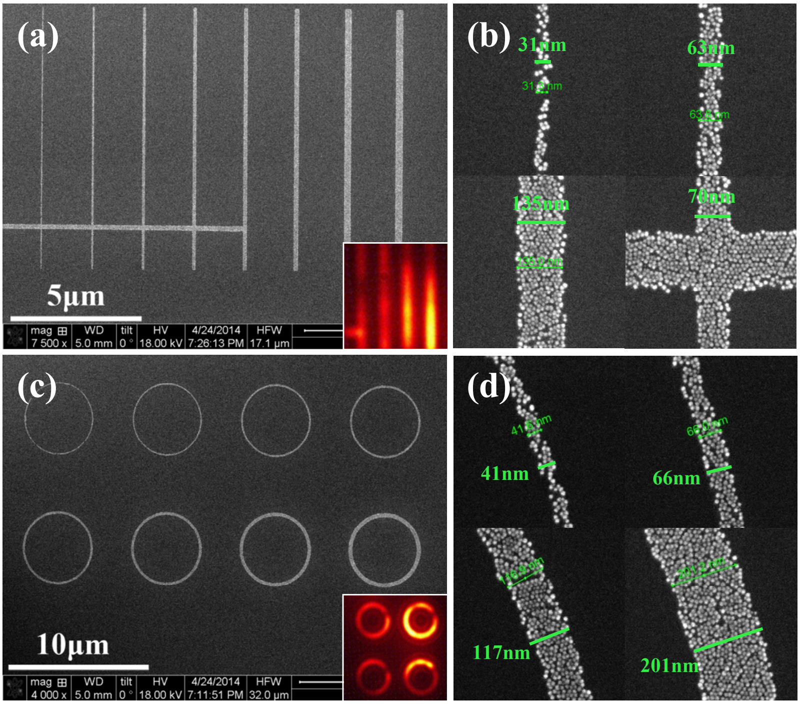

**Figure 3.7:** SEM images of the nanoscale patterns for QD films. (a) Line and (c) ring patterns with different widths, and the enlarged views for some selected widths for line (b) and ring (d) patterns, respectively. The insets at the right lower corner in (a, c) show the respective micro-PL of the corresponding pattern shapes.

Finally, using a mask consisting of holes with different diameters we found uniformly filled QD patches can be formed for holes of 60 nm diameter, as shown in Figure 3.8(a). Compared to the line and ring patterns these hole patterns are more difficult to form. To fill the resist hole the LB film now has to bend in all directions. When the size of the hole becomes comparable to the thickness of the resist, given the increasing ratio of the sidewall to hole area, the proportion of QDs deposited on the resist sidewalls that are eventually lifted off significantly increases while the probability for the QDs to remain in the target hole site on the substrate decreases. As shown in Figure 3.8(b), a reduction of the diameter of the hole in the resist also induces a more random deposition of the QDs on the substrate, similar to the edge effect observed with strip patterns. In the case of 47 nm wide holes for example, this leads to deposits containing only a few, often unconnected QDs. This suggests that a further reduction of the resist hole diameter to dimensions comparable to the size of the QD itself, may lead to the trapping of a single QD in the resist hole. We will explore this probability in next section.

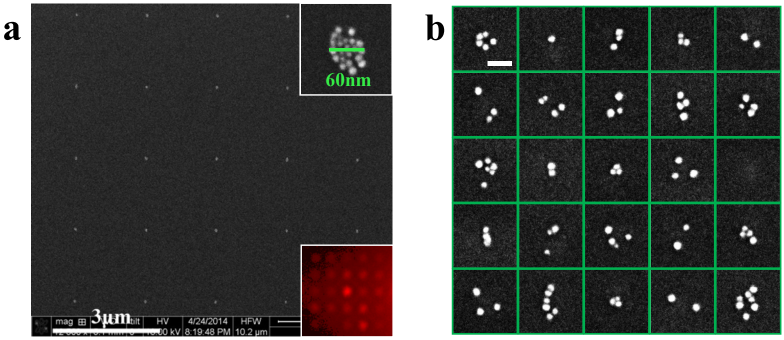

**Figure 3.8:** (a) SEM image of the array of dot patterns with an average diameter of 60 nm and the enlarged image of one dot in the inset at right upper corner. The inset at the right lower corner shows the micro-PL of the dot-pattern array. (b) SEM images of 5×5 dot patterns of QDs with a resist hole diameter of ~47 nm. All images have the same scale bar of 50 nm as shown in the image at the left top corner.

## 3.4 Single-dot patterning

It is clearly seen that the use of 47nm-diameter hole pattern can localize few QDs. This leads us to believe further reducing the hole size could realize single-dot pattern with high probability. In this section, before carrying out experimental tests, first we propose a simple mathematical model for describing the deposition of QDs into small hole patterns. Using this model, we can numerically predict the distribution of the number of QDs for a given parameter set of pattern and QD dimensions and thus provide valuable guidance for experimental settings. Then we experimentally demonstrate single-dot patterning and also reveal statistical characteristics in the probability distribution of the number of QDs which shows good agreement with experimental results.

### 3.4.1 Modeling of single-dot deposition

To assess upfront the probability of trapping individual QDs on predefined spots of a substrate using a resist pattern consisting of an array of holes with small diameter and a certain resist thickness as drawn in Figure 3.9(a) and (b), we build on the conclusion that the resist sidewalls break apart the LB film resulting in a randomized deposition of QDs on the resist sidewalls and the substrate. The probability of retaining a given number of QDs on the substrate will then depend on the QD diameter and the surface areas of the hole and the resist sidewall.

More specifically, the QD LB film can be described as a hexagonal close-packed (hcp) plane consisting of spheres with constant diameter (2*r*) as shown in Figure 3.9(c).

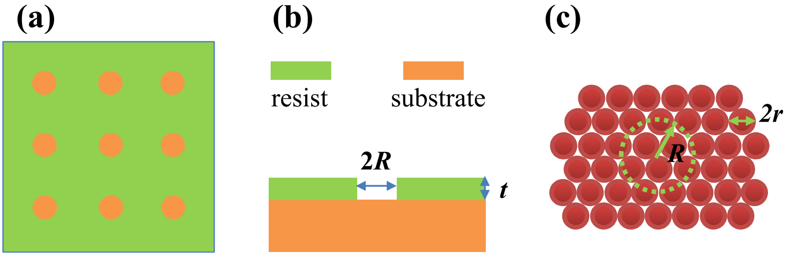

**Figure 3.9:** (a) Schematics of the array of hole patterns, (b) the side view of the hole with a diameter of 2*R* and a resist thickness of *t*, and (c) the ideal close-packed QD film with the green-dot circle designated as the opening of the resist hole under the LB film.

Assuming a resist thickness $t$ and hole radius $R$, the hole area $S_\mathrm{h}$ on the substrate and the sidewall area $S_\mathrm{s}$ of resist are simply calculated as $S_\mathrm{h} = \pi R^2$, and $S_\mathrm{s} = 2\pi R t$, respectively. On the other hand, the number of QDs $n$ overlapping with the hole area can approximately be expressed as

$$n = \Gamma \frac{S_\mathrm{h}}{\pi r^2}, \tag{3.1}$$

where $\Gamma$ is the packing fraction for the 2D hcp lattice given by $\Gamma = \pi/2\sqrt{3}$. On the basis of our previous discussion, we neglect interparticle interactions and postulate that these $n$ QDs are randomly deposited over the substrate area $S_\mathrm{h}$ and a fraction $\alpha$ of the sidewall area $S_\mathrm{s}$ and that only the QDs actually deposited on the substrate will be retained after the lift-off process. The average number of QDs $N$ retrieved on the substrate is then given by the product of $n$ and the ratio of the accessible substrate area and the total area, substrate and sidewalls, available to the $n$ QDs

$$N(r, R, t, \alpha) = \Gamma \frac{S_\mathrm{h}}{\pi r^2} \frac{S_\mathrm{h}}{S_\mathrm{h} + \alpha S_\mathrm{s}}. \tag{3.2}$$

To test this model, we analyze the number of QDs deposited on a line formed using a photoresist trench only 35–40 nm across. As shown in Figure 3.7(b), the number of deposited QDs can be readily obtained by counting whereas it can be predicted using our model. For a resist line pattern with a width of *W*, length of *L*, and thickness of *t*, Equation (3.2) becomes

$$N = \Gamma \frac{LW}{\pi r^2} \frac{LW}{LW + 2\alpha L t}, \tag{3.3}$$

where $N$ is the average number of QDs $N$ retrieved on the substrate. Figure 3.10(a) shows the calculated $N$ as a function of $W$ for a given line length of 1.1 µm, for $\alpha$ = 0.7, 0.85, and 1.0, respectively. The red solid line indicates the experimental number of QDs $N_{\mathrm{exp}}$ for a line pattern with a length of 1.1 µm, obtained by counting QD number from SEM image of Figure 3.10(b). Considering the uncertainty on the width of the resist trench in experiment which ranges between 35 and 40 nm, we find that the actual number of deposited QDs matches the numerical prediction for $\alpha$ ranging from 0.7 to 1.0 with a best match obtained for $\alpha \approx 0.85$.

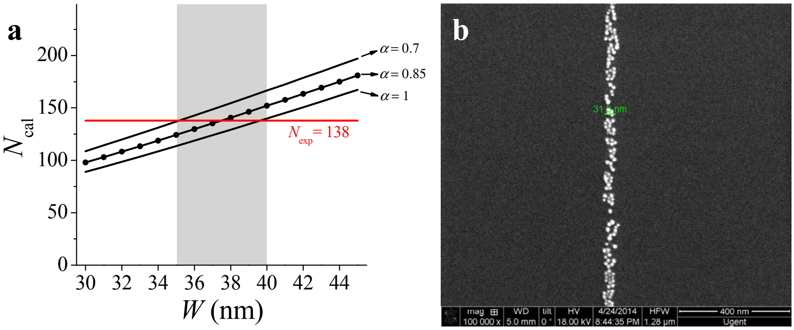

**Figure 3.10:** (a) Calculated average number of deposited QDs $N_{\mathrm{cal}}$ using a line pattern as a function of the line width $W$, for $\alpha$ = 0.7, 0.85, and 1.0, respectively. The red solid line indicates the experimental number of QDs $N_{\mathrm{exp}}$=138 for a line resist pattern with a length of 1.1 µm and a certain width. The grey area indicates the range of the uncertainty of the line width (~35-40 nm) in the experiment. (b) SEM image of the associated line pattern of QDs.

We therefore use the above model to calculate the distribution of $N$ from Equation (2) as a function of $R$ and $t$ for a given $r$ and $\alpha$. In Figure 3.11, we show the calculated map of $N$ for the QDs used in our experiment with $r$ of 6.5 nm obtained by measuring the average center-to-center distance between LB QDs under SEM and taking $\alpha$ = 1.0. To achieve maximal probability of single-QD patterning, intuitively we should adopt such parameters of $R$ and $t$ that the value of $N$ can be maintained around 1.0 as indicated by the white dot line in Figure 3.11. The calculated map clearly shows that $N$ is very sensitive to the diameter of the patterned hole. For $N$~1.0 and resist thickness ranging from 10 to 50 nm the allowed working diameter window is only ~12 nm. Increasing the hole size above 35 nm results in a larger tolerance on the exact diameter but also leads to a dramatic increase in the optimal resist thickness (> 50 nm) and a corresponding increase in aspect ratio $t/2R$. Intuitively it will be more difficult to coat a LB film conformally into a high aspect ratio hole. Furthermore, the relative fraction of QDs attached to the sidewall versus those attached on the substrate will increase leading to a larger variation on the number of QDs left on the surface. To the contrary, for smaller diameter of the hole, the required thickness $t$ (e.g., $t$ ~ 10 nm at $2R$ ~ 22 nm) for obtaining $N$~1.0 can be significantly reduced, decreasing the aspect ratio and facilitating deposition of the QD film. As discussed above however, given a particular QD size, there exists a threshold thickness $t$ for the resist to allow for a successful lift-off process without residual QDs. For our QDs, this threshold thickness is ~20 nm with a corresponding optimal hole diameter of 27 nm for $N$~1.0 as can be derived from Figure 3.11. The minimum hole diameter we can stably define in our EBL system however is 30–32 nm with a corresponding optimal resist thickness of 30–36 nm.

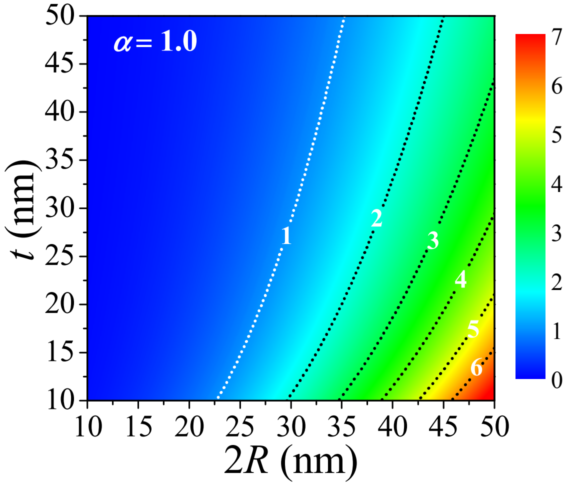

**Figure 3.11:** Contour image of the calculated $N$ as a function of the resist thickness $t$ and hole diameter $2R$ for QDs with an effective radius of $r$ = 6.5 nm and $\alpha$ = 1.0.

### 3.4.2 Experimental demonstration

To achieve optimal single QD deposition according to the calculation from our model, we patterned a 5×5 array of holes with diameter ~31 nm in a 33 nm thick resist layer. After LB deposition and lift-off we observed and counted the number of QDs at each site via high-resolution SEM. In Figure 3.12(a), we show the collection of SEM images of the 5×5 dot patterns. We have eight cases of single-QD occupancy for a total of 25 holes, equivalent with a single-QD yield of 32%. The deviation of the number of QDs is pretty small and most holes end up with 0–3 QDs. In order to obtain a statistically more reliable distribution, we inspected patterns of 300 holes each for four different hole diameters. The results are shown in Figure 3.12(b) using a different symbol for each hole diameter. For a diameter of 31.6 nm the probability of obtaining a single-QD reaches a peak value of ~40% and the deviation of the distribution is only ~2 counts. When increasing the hole diameter, the single-QD probability decreases rapidly (only ~8% for 46.8 nm diameter) and the peak of the probability shifts to larger QD counts. The distribution also broadens to about ~3.5 counts for a hole diameter of 46.8 nm. The shift of the probability peak is intuitively understood from the $N$ map shown in Figure 3.11: when increasing the diameter for fixed resist thickness the expected number of QDs deposited on the substrate distinctively increases. Even so, the average number of deposited QDs $N$ as shown in Figure 3.11 only gives a partial description of the experimentally observed distribution curves, without accounting for, for example, their absolute position and magnitude or their broadening with increasing hole diameter. Moreover, it does not allow us to determine the upper limit for the probability of single-QD positioning in the experiment.

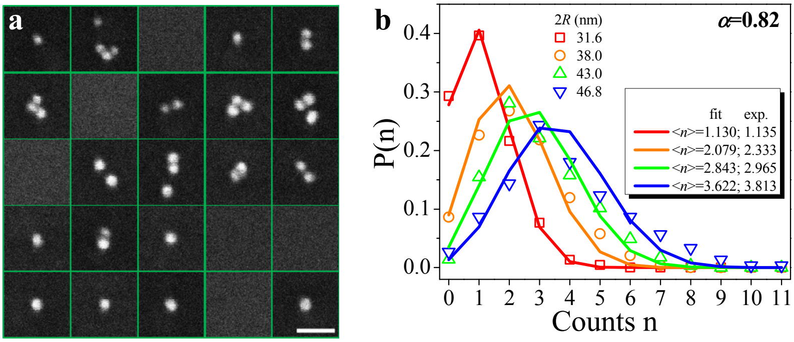

**Figure 3.12:** (a) SEM images of 5×5 dot patterns of QDs by using the resist hole of 31.6 nm diameter and ~33 nm thickness. All images have the same scale bar of 50 nm as shown in the image at the right bottom corner. (b) The experimental (scatters) and binomial fitting (solid lines) distribution of the probability P(n) as a function of the count of QDs for different diameters of the resist hole by counting 300 dot patterns, respectively.

To assess the statistical characteristics behind the experimentally measured distribution for the probability of QD counts, we further build on the randomizing effect of the resist sidewall on the QD deposition. This allows us to look at the deposition of a QD on the substrate as an event that has a success probability $p$ given by the ratio between the accessible substrate area and the total area available, expressed as

$$p = \frac{S_\mathrm{h}}{S_\mathrm{h} + \alpha S_\mathrm{s}}, \tag{3.4}$$

where $S_\mathrm{h}$, $S_\mathrm{s}$, and $\alpha$ were defined previously. Since $n$ QDs are deposited within each hole, the probability distribution of the number of QDs deposited on the substrate can then be approximated by a binomial distribution B($n$, $p$) with $n$ trials that each have a success probability $p$. In this way, by calculating B($n$, $p$) for a given $t$, $R$, and $\alpha$ we can calculate the probability distribution for the number of QDs deposited on the substrate.

First, we determine the a priori unknown parameter $\alpha$ by fitting the function B($n$, $p$) with $n(R, t)$ and $p(R, t, \alpha)$ to the experimentally obtained distribution curves for $t$=33 nm and 2$R$ = (31.6, 38.0, 43.0, 46.8 nm). In this procedure, $n(R, t)$ as calculated using Equation (3.1) was rounded to the closest lower integer value, that is, the maximum number of QDs that fit into the patterned hole, and $p(R, t, \alpha)$ was obtained from Equation (3.4). Using a least-mean-square algorithm with $\alpha$ as the only free parameter we obtain $\alpha$=0.82 for an optimal fit, which is in close agreement to the value found previously for QD strip patterns. The result is shown in Figure 3.12(b) in solid lines, showing excellent agreement with the experimental results, especially for the smallest diameter of 31.6 nm. With increase of the diameter, the shift of the probability peak and the broadening of the distribution in the fits exactly represent the features of the experimental data. Note that we adopt an identical value for the parameter $\alpha$ for all fits and the good correspondence between experiment and fitting verifies our assumption that the sidewall area contributes to a certain proportion of the total deposition area in the case of small diameter hole patterns. The insert panel of Figure 3.12(b) shows the mean $\langle n \rangle$ calculated for both the experimental and the fitted data. The discrepancy between both is less than 10% again indicating the suitability of the binomial distribution model for the description of the behavior of the deposition process of a LB QD film in a narrow hole pattern. Also, note that for the largest holes, the binomial distribution underestimates the fraction of deposits containing more than five QDs. This may reflect the original observation that the LB film is only disturbed around the resist sidewalls, making that for larger resist holes the original LB film will be retrieved in the center of the deposit.

Although we experimentally achieved a single-QD pattering probability as high as 40% it is still interesting to explore the upper limit of this probability in the present technique. Relying on the above model, we therefore calculate the single-QD count probability P(n=1) as a function of the diameter 2$R$ of the hole and the resist thickness *t* with the experimentally obtained value $\alpha$=0.82. The result is shown in Figure 3.13. Note that the discontinuity at certain diameters stems from the discreteness of the integer *n*. Figure 4c shows that it is theoretically possible to accomplish a probability close to 100% for an infinitely thin resist thickness (<5 nm). However, we have already established that such a thin resist is not compatible with a successful and residue-free lift-off process. Taking into account the threshold thickness of *t*~ 20 nm for the resist layer, a probability of ~45% theoretically can be reached. Considering the resolution limitation of our EBL system for the definition of the hole diameter (30–32 nm), the calculation shows a maximal probability of ~42% for single-QD positioning as indicated by the red cross in Figure 4c, very close to our experimental result of ~40%. Using larger size quantum dots does not substantially increase this probability but does relax the requirements on the patterned holes, both in absolute size and in acceptable size variation.

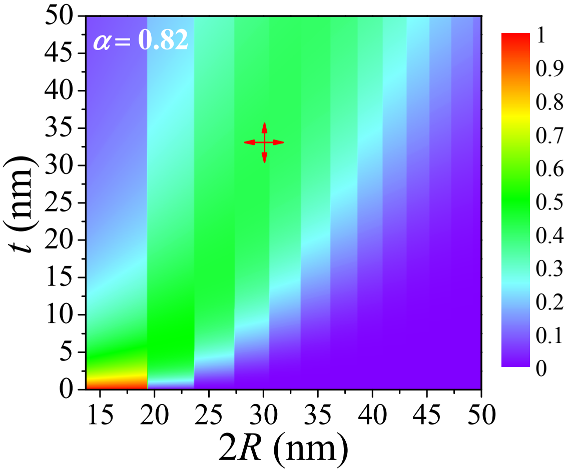

**Figure 3.13:** The calculated probability of single-QD count P(n=1) as a function of the diameter 2*R* of hole and resist thickness *t* by using a binomial distribution B(*n*, *p*), with the red cross indicating the probability of ~42% at 2*R*=30 nm and *t*=33 nm.

## 3.5 Conclusion

In summary, using high quality LB deposition and a residue-free lift-off process, we experimentally demonstrated both nanoscale and single-dot patterning of colloidal QD-films. Feature sizes down to ~30 nm for a continuously uniform film of QDs and a yield up to 40% for single-QD positioning are obtained. To describe the experimental processes a theoretical model was proposed. The good agreement between the experiment and the numerical model reveals that the deposition behavior of QDs onto a substrate and the experimental distribution of QD counts can be described by a binomial distribution, providing valuable guidance in the realization of single-QD patterns with an expected yield. The presently developed patterning technology for QDs provides an efficient tool both for the fundamental study of the properties of stand-alone QDs and for the quantitative investigation of the interaction between QDs and their environment such as on-chip photonic or electronic devices. We believe that this technique will open up various novel applications relying on QDs and represents a practically significant step toward the development of real optoelectronic devices based on QDs.

In particular, in our own case, this technique is carried out in an ongoing effort to realize single-QD emitters whereby a single QD can be localized in photonic components such as a highly confined waveguide for exploring on-chip single-photon emission. Also, in the future we may employ this technique for integrating a few or a single QD in optical resonators and studying lasing in such devices where both the QD number and position need to be precisely controlled for deterministic optical coupling.

# References

[1] A. Omari, P. Geiregat, D. Van Thourhout, and Z. Hens, "Light absorption in hybrid silicon-on-insulator/quantum dot waveguides," Opt. Express **21**(20), 23272-23285 (2013).

[2] A. Omari, W. Q. Xie, P. Geiregat, D. Van Thourhout, and Z. Hens, "Modeling the Optical Properties of Low-Cost Colloidal Quantum Dot Functionalized Strip SOI Waveguides," IEEE J. Sel. Top. Quantum Electron. **20**(4) (2014).

[3] A. G. Pattantyus-Abraham, H. J. Qiao, J. Shan, K. A. Abel, T. S. Wang, F. C. J. M. van Veggel, and J. F. Young, "Site-Selective Optical Coupling of PbSe Nanocrystals to Si-Based Photonic Crystal Microcavities," Nano Lett. **9**(8), 2849-2854 (2009).

[4] S. Gupta and E. Waks, "Spontaneous emission enhancement and saturable absorption of colloidal quantum dots coupled to photonic crystal cavity," Opt. Express **21**(24), 29612-29619 (2013).

[5] A. Qualtieri, F. Pisanello, M. Grande, T. Stomeo, L. Martiradonna, G. Epifani, A. Fiore, A. Passaseo, and M. De Vittorio, "Emission control of colloidal nanocrystals embedded in $Si_3N_4$ photonic crystal H1 nanocavities," Microelectron. Eng. **87**(5-8), 1435-1438 (2010).

[6] P. P. Pompa, L. Martiradonna, A. Della Torre, F. Della Sala, L. Manna, M. De Vittorio, F. Calabi, R. Cingolani, and R. Rinaldi, "Metal-enhanced fluorescence of colloidal nanocrystals with nanoscale control," Nat. Nanotechnol. **1**(2), 126-130 (2006).

[7] P. Michler, A. Imamoglu, M. D. Mason, P. J. Carson, G. F. Strouse, and S. K. Buratto, "Quantum correlation among photons from a single quantum dot at room temperature," Nature **406**(6799), 968-970 (2000).

[8] X. Y. Wang, X. F. Ren, K. Kahen, M. A. Hahn, M. Rajeswaran, S. Maccagnano-Zacher, J. Silcox, G. E. Cragg, A. L. Efros, and T. D. Krauss, "Non-blinking semiconductor nanocrystals," Nature **459**(7247), 686-689 (2009).

[9] R. Osovsky, D. Cheskis, V. Kloper, A. Sashchiuk, M. Kroner, and E. Lifshitz, "Continuous-Wave Pumping of Multiexciton Bands in the Photoluminescence Spectrum of a Single CdTe-CdSe Core-Shell Colloidal Quantum Dot," Phys. Rev. Lett. **102**(19)(2009).

[10] A. P. Beyler, L. F. Marshall, J. Cui, X. Brokmann, and M. G. Bawendi, "Direct Observation of Rapid Discrete Spectral Dynamics in Single

Colloidal CdSe-CdS Core-Shell Quantum Dots," Phys. Rev. Lett. **111**(17), 177401-177405 (2013).

[11] L. Li, G. J. Tian, Y. Luo, H. Brismar, and Y. Fu, "Blinking, Flickering, and Correlation in Fluorescence of Single Colloidal CdSe Quantum Dots with Different Shells under Different Excitations," J. Phys. Chem. C **117**(9), 4844-4851 (2013).

[12] Y. S. Park, W. K. Bae, L. A. Padilha, J. M. Pietryga, and V. I. Klimov, "Effect of the Core/Shell Interface on Auger Recombination Evaluated by Single-Quantum-Dot Spectroscopy," Nano Lett. **14**(2), 396-402 (2014).

[13] G. A. Grinbom, M. Saraf, C. Saguy, A. C. Bartnik, F. Wise, and E. Lifshitz, "Density of states in a single PbSe/PbS core-shell quantum dot measured by scanning tunneling spectroscopy," Phys. Rev. B **81**(24), 245301-245307 (2010).

[14] B. Diaconescu, L. A. Padilha, P. Nagpal, B. S. Swartzentruber, and V. I. Klimov, "Measurement of Electronic States of PbS Nanocrystal Quantum Dots Using Scanning Tunneling Spectroscopy: The Role of Parity Selection Rules in Optical Absorption," Phys. Rev. Lett. **110**(12), 127406-127405 (2013).

[15] K. Maturova, S. U. Nanayakkara, J. M. Luther, and J. van de Lagemaat, "Fast Current Blinking in Individual PbS and CdSe Quantum Dots," Nano Lett. **13**(6), 2338-2345 (2013).

[16] A. Qualtieri, G. Morello, P. Spinicelli, M. T. Todaro, T. Stomeo, L. Martiradonna, M. De Giorgi, X. Quelin, S. Buil, A. Bramati, J. P. Hermier, R. Cingolani, and M. De Vittorio, "Nonclassical emission from single colloidal nanocrystals in a microcavity: a route towards room temperature single photon sources," New J. Phys. **11**(2009).

[17] C. T. Yuan, Y. C. Wang, H. W. Cheng, H. S. Wang, M. Y. Kuo, M. H. Shih, and J. Tang, "Modification of Fluorescence Properties in Single Colloidal Quantum Dots by Coupling to Plasmonic Gap Modes," J. Phys. Chem. C **117**(24), 12762-12768 (2013).

[18] J. N. Farahani, D. W. Pohl, H. J. Eisler, and B. Hecht, "Single quantum dot coupled to a scanning optical antenna: A tunable superemitter," Phys. Rev. Lett. **95**(1), 017402-017404 (2005).

[19] A. G. Curto, G. Volpe, T. H. Taminiau, M. P. Kreuzer, R. Quidant, and N. F. van Hulst, "Unidirectional Emission of a Quantum Dot Coupled to a Nanoantenna," Science **329**(5994), 930-933 (2010).

[20] A. G. Curto, T. H. Taminiau, G. Volpe, M. P. Kreuzer, R. Quidant, and N. F. van Hulst, “Multipolar radiation of quantum emitters with nanowire optical antennas,” Nature Communications **4**(2013).

[21] I. M. Hancu, A. G. Curto, M. Castro-Lopez, M. Kuttge, and N. F. van Hulst, “Multipolar Interference for Directed Light Emission,” Nano Lett. **14**(1), 166-171 (2014).

[22] K. Lambert, I. Moreels, D. Van Thourhout, and Z. Hens, “Quantum dot micropatterning on si,” Langmuir **24**(11), 5961-5966 (2008).

[23] M. H. V. Werts, M. Lambert, J. P. Bourgoin, and M. Brust, “Nanometer scale patterning of Langmuir-Blodgett films of gold nanoparticles by electron beam lithography,” Nano Lett. **2**(1), 43-47 (2002).

[24] Y. Park, Y. G. Roh, U. J. Kim, D. Y. Chung, H. Suh, J. Kim, S. Cheon, J. Lee, T. H. Kim, K. S. Cho, and C. W. Lee, “Nanoscale patterning of colloidal quantum dots on transparent and metallic planar surfaces,” Nanotechnology **23**(35), 355302 (2012).

[25] T. S. Mentzel, D. D. Wanger, N. Ray, B. J. Walker, D. Strasfeld, M. G. Bawendi, and M. A. Kastner, “Nanopatterned Electrically Conductive Films of Semiconductor Nanocrystals,” Nano Lett. **12**(8), 4404-4408 (2012).

[26] V. R. Manfrinato, D. D. Wanger, D. B. Strasfeld, H. S. Han, F. Marsili, J. P. Arrieta, T. S. Mentzel, M. G. Bawendi, and K. K. Berggren, “Controlled placement of colloidal quantum dots in sub-15 nm clusters,” Nanotechnology **24**(12), 125302 (2013).

[27] Q. Zhang, C. Dang, H. Urabe, J. Wang, S. H. Sun, and A. Nurmikko, “Large ordered arrays of single photon sources based on II-VI semiconductor colloidal quantum dot,” Opt. Express **16**(24), 19592-19599 (2008).

[28] M. M. Jiang, J. A. Kurvits, Y. Lu, A. V. Nurmikko, and R. Zia, “Reusable Inorganic Templates for Electrostatic Self-Assembly of Individual Quantum Dots, Nanodiamonds, and Lanthanide-Doped Nanoparticles,” Nano Lett. **15**(8), 5010-5016 (2015).

[29] M. Cirillo, T. Aubert, R. Gomes, R. Van Deun, P. Emplit, A. Biermann, H. Lange, C. Thomsen, E. Brainis, and Z. Hens, “"Flash" Synthesis of CdSe/CdS Core-Shell Quantum Dots,” Chem. Mater. **26**(2), 1154-1160 (2014).

[30] K. Lambert, Y. Justo, J. S. Kamal, and Z. Hens, “Phase Transitions in Quantum-Dot Langmuir Films,” Angew. Chem. Int. Ed. **50**(50), 12058-12061 (2011).

# 4

# Hybrid integration of QDs and SiN

In Chapter 2 we have developed a passive Silicon nitride (SiN) photonics platform and demonstrated low-loss waveguides and high-quality microresonators, which can provide functionalities for manipulating photons within submicron structures on a chip. However, generating photons, a key function in integrated photonics, is still missing, due to the dielectric nature of SiN. As highly luminescent emitters, obviously semiconductor colloidal quantum dots (QDs) have great potentials as photon-generating media incorporated in passive photonics possibly via a hybrid integration approach.

In this Chapter, we develop a compatible platform for the hybrid integration of SiN photonics with colloidal QDs. Based on this platform, SiN waveguides with a monolayer of QDs embedded inside are fabricated. Both the preservation of QD luminescence and low waveguides loss are demonstrated. This fabrication technology is further used for developing waveguide-coupled free-standing SiN microdisks integrated with embedded QDs. The detailed photoluminescence (PL) characterization of the fabricated devices reveals both high performance in disk resonators and efficient coupling of QD emission to disk resonance modes and eventually to the on-chip waveguide. The presented optically active devices provide new opportunities for the development of novel optoelectronic devices based on QDs.

## 4.1 Concept of QD-SiN integration

As we have demonstrated, SiN integrated photonics is compatible with complementary metal-oxide-semiconductor (CMOS) processing technology and enables miniaturizing optical functions, operating at both visible and infrared wavelengths, compactly integrated on a chip. Therefore, it has become a promising platform both for cost-effective and high-volume applications such as optical communication, information processing or optical sensing as well as for fundamental optics research in various domains such as nonlinear optics, cavity quantum electrodynamics and quantum optics. However, because of its dielectric nature, so far most demonstrated SiN photonic building blocks are limited to passive optical functions such as transmission with low-loss waveguides and temporal and spatial manipulation of photons with high quality (Q) microresonators. The generation of light in SiN photonics, as a basic and probably central issue for a complete photonics system, still remains to be addressed.

A straightforward approach of realizing integrated light sources, driven by optical or electrical excitation, is to incorporate external light-emitting materials physically into passive photonic components, that is, the concept of hybrid integration. In fact, such attempts have already been undertaken in silicon photonics, for example, through the use of wafer bonding techniques or through direct growing III-V semiconductors on passive photonics and active devices operating at near infrared and telecom wavelengths have also been demonstrated [1, 2]. Apart from conventional bulky materials, the hybrid integration concept however can also be applied to other materials and in particular to nanomaterials which possess novel and adjustable optical and electrical properties and have been extensively studied in recent decades. Among these materials, colloidal semiconductor QDs [3-5], due to their size-dependent quantum confinement effects and vast choices of material, exhibit widely tunable absorption and emission spectra, perfectly matching the broadband transparency of SiN photonics. Moreover, today's available nanotechnologies such as synthesis and processing for QDs make them applicable for practical applications. Consequently, they are becoming suitable for integration with existing passive photonics for the development of integrated light sources and even low-threshold lasers. In return, the combination of integrated photonic building blocks and QD emitters could provide an ideal platform for fundamental studies of light-matter interaction and quantum optics experiments based on QDs. In particular, by using our patterning technique introduced in Chapter 3, we can integrate either an ensemble or single QDs deterministically in SiN photonics possibly for making on-chip quantum emitters.

Obviously, an effective integration technique able to handle solution-processible QDs within a top-down CMOS-like manufacturing flow for SiN photonics is critically important. However, because of the inherent differences between QDs and SiN photonics in terms of material composition and processing, it remains a big challenge to develop such a process which should fulfill the following basic requirements:

(i) Preserve the optical properties of QDs from solution to solid films
(ii) Provide robust and long-term stabilization for QDs
(iii) Allow for efficient coupling between QD emission and optical modes of an integrated waveguide device
(iv) Ensure high performance passive and active devices can be realized simultaneously.

To fulfill above requirements, a low-temperature process is preferable to minimize degradation of the optical quality of the QDs. Second, a processing scheme capable of embedding QDs in SiN layers appears to be an ideal option both for environmental stabilization and for optimal coupling. Finally, we can confine QDs selectively in active regions without affecting passive components, through either localization methods or design strategies.

In the following sections, we first demonstrate a low-loss hybrid QD-SiN photonic platform by using low-temperature and optimal fabrication processes. The performance of this hybrid platform is quantitatively evaluated by characterizing the optical loss of QD-SiN waveguides with a monolayer of QDs embedded inside. Then on-chip waveguide-coupled QD-SiN microdisks are fabricated using a vertical coupling design that is able to separate passive and active layers and thereby allows to achieve high performance integrated active resonators.

## 4.2 Low-loss QD-SiN waveguide development

Colloidal QDs have already been employed in various types of photonic devices, including polymer waveguides [6-8], silicon photonics [9, 10], and SiN microcavities [11-13]. In most examples, the QDs were either stabilized in a polymer matrix or directly dispersed on the surface of the devices. Given the drawbacks of the polymers used (low index contrast, unknown long term stability) and the instability of the QDs themselves when they are left exposed, there is a need for the integration of colloidal QDs with an all inorganic low-loss photonics platform whereby the QDs are fully encapsulated. Moreover, all these demonstrations were achieved in an individual component and often experimental results show either weak coupling of QD emission into optical modes or low out coupling efficiency, because either they lack an effective embedding scheme or they lack an efficient coupling scheme. Therefore, a reliable photonics platform fully integrated with QDs remains to be demonstrated and practical devices integrated on chip need to be developed and quantitatively assessed.

In this section, relying upon previously developed low-loss passive SiN photonics based on a low-temperature (120–270 °C) plasma-enhanced chemical vapor deposition (PECVD), we develop a low-loss hybrid QD-SiN waveguides fabricated by using a dry etching process further optimized specifically for the QD-SiN system. These waveguides, with a close-packed monolayer of colloidal QDs embedded into two layers of SiN, exhibit losses as low as 2.69 dB/cm at 900 nm wavelength. Since only standard lithography and direct top-down etching is utilized here, one could envisage leveraging mature CMOS technology for the realization of even advanced active SiN devices, for example, high-Q factor cavities with embedded QDs, as we will investigate in next section.

### 4.2.1 Fabrication processes

The fabrication includes substrate preparation and waveguide definition, as shown in the process flow in Figure 4.1(a). Firstly we prepared a SiN/QD/SiN sandwich substrate starting with a silicon wafer with a 3μm thermal $SiO_2$ box layer, onto which first a ~100 nm SiN layer was deposited using an optimized PECVD process with a low plasma frequency at a temperature of 270 °C, as described in Chapter 2. Next a close-packed monolayer of colloidal QDs was transferred onto the SiN substrate by a Langmuir–Blodgett (LB) method. We used CdSe/CdS core/shell QDs, a typical visible-emission colloidal QD-type, with a diameter of ~7.2 nm and a central emission peak of ~625 nm. The quality of the QD-film was examined by scanning electron microscope (SEM) and photoluminescence (PL) under a UV lamp, as presented in Figure 4.1(b) and (c), showing the layer of QDs is uniform over large areas. A second ~100 nm SiN layer was subsequently deposited for embedding the LB QDs layer, using the same PECVD process. In this case a temperature of 120 °C was used however to minimize impact on the optical quality of the QDs [13], while still retaining sufficient material quality for the SiN to allow for low-loss photonic devices. This is confirmed by ellipsometry measurements where, within the measurement accuracy, we do not see a distinct difference in the extinction coefficient of SiN deposited at 120 °C compared to that deposited at 270 °C. The refractive index on the other hand (measured at 900 nm) changes from 1.92 to 1.85 with the temperature decreasing from 270 °C to 120 °C, indicating a reduction in the material density. After preparation of the substrate, the same photoresist mask previously designed for waveguide-loss measurement was used to pattern QD-SiN layers using optimized contact optical lithography. Finally, the waveguide pattern was transferred into the QD-SiN layers by using reactive ion etching (RIE) to form strip waveguides. For simplicity, hereafter the terms H-SiN and L-SiN will be used to refer to SiN deposited at 270 °C and at 120 °C respectively, as we did before. In order to evaluate the influence of the QDs on the waveguide loss, we also fabricated waveguides using a H-SiN/L-SiN stack without QDs for comparison.

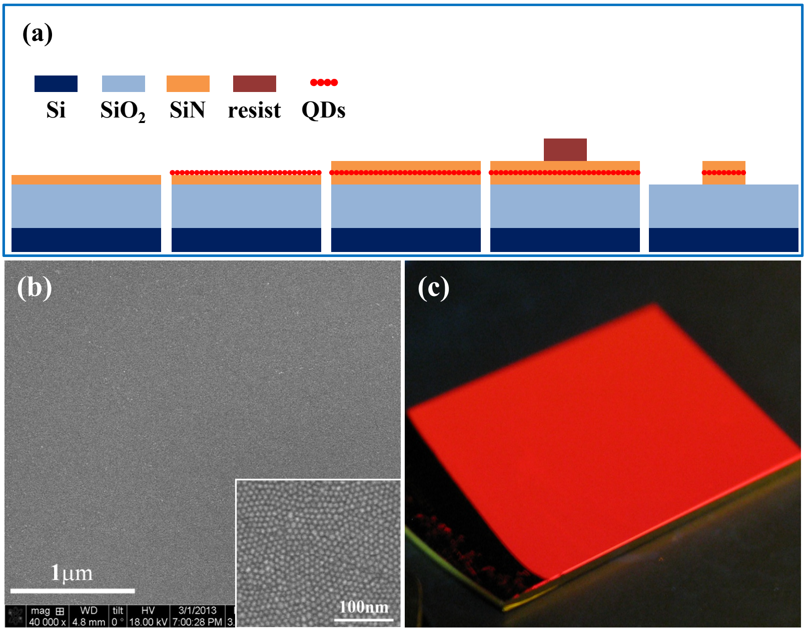

**Figure 4.1:** (a) Schematics of QD-SiN hybrid waveguide fabrication flow. (b) SEM image of the LB QD-film with the inset showing the close-packed LB QD-film under a high resolution. (c) PL of a 2×2 cm LB QD-film illuminated with a UV lamp.

### 4.2.2 Optimization of dry etching for QD-SiN

In Chapter 2, we have obtained the optimized RIE conditions for H-SiN/L-SiN etching using a gas system of $CF_4/H_2$ (80sccm/3sccm), a RF power of 210 W, and a chamber pressure of 20mTorr. In the case of etching composite QD-SiN films, due the large differences not only in material density of SiN but also in material composition between SiN and QDs, it is more difficulty to have a RIE process capable of achieving vertically co-etched sidewalls and reasonably smooth surfaces. Based on our understanding of the etching mechanism in the $CF_4/H_2$ gas system, we know that $H_2$ plays a critical role in the formation of the polymer inhibitor on lateral sidewalls and that increasing the content of $H_2$ can significantly promote this protection process for the sidewalls. Therefore, we start with the optimized recipe and modify the content of $H_2$ to investigate the effects on etching profiles of SiN/QD/SiN layers. Again, our initial etching experiments are carried out on silicon substrates and the etched samples are inspected by means of high-resolution SEM analysis and focused ion beam (FIB) milling. When making a FIB cross section, again structures are protected by a Pt layer.

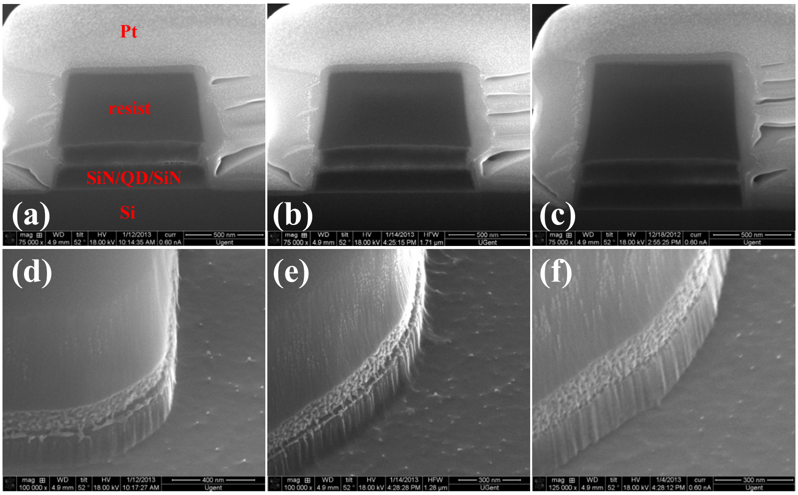

**Figure 4.2:** FIB cross-sectional and sidewall images of the as-etched H-SiN/QD/L-SiN layers. The gas system is $CF_4/H_2$ with different ratios of (a, d) 80sccm/3sccm, (b, e) 60sccm/3sccm, and (c, f) 40sccm/3sccm.

In Figure 4.2, we show the etch results under different $H_2$ content. Apparently, this RIE process does indeed allow etching through the close-packed monolayer of CdSe/CdS QDs, most probably through the formation of volatile organometallic etch products in the $CF_4/H_2$ plasma [14]. However, due to the slight quality loss of the L-SiN when deposited on the QD layer, the etching with $CF_4/H_2$ (80sccm/3sccm) results in an unwanted undercut at the interface of L-SiN and QDs, leaving an observable step, as shown in Figure 4.2(a, d). When increasing the hydrogen content ratio in the gas mixture in Figure 4.2(b, e), it is clearly seen that the profile of the sidewall is ameliorated in terms of continuity of slope and surface roughness thanks to the enhanced lateral protection. Under a $CF_4/H_2$ (40sccm/3sccm), the sidewall is etched almost vertically and exhibits a topologically continuous surface without distinct roughness, as seen in Figure 4.2(c, f). Additionally, the embedded QD layer is clearly visible and shows negligible defects along the uniform monolayer, indicating the high quality of the LB process used for preparing the layer and the fact that the dry etching process does not attack the layer. Thus, the gases of $CF_4/H_2$ (40sccm/3sccm) will be used for etching hybrid QD-SiN waveguides with nearly a monolayer of QDs embedded in the SiN layer. It should be added that the optimal etching process for a thicker embedded QD layer may slightly differ from the single-layer situation and will be discussed during the integration with thicker QD layers in SiN cavities in the next section.

### 4.2.3 Characterization of PL and waveguide loss

In Figure 4.3(a, b), we show cross-sectional photographs of 2μm-wide waveguides defined in H-SiN/L-SiN and H-SiN/QD/L-SiN structures deposited on a 3 μm oxide layer. Both types of waveguides consist of a ~100 nm bottom H-SiN layer and a ~100 nm top L-SiN layer. In the case of the hybrid H-SiN/QD/L-SiN waveguide, a monolayer of QDs is embedded between the two layers of SiN (not clearly visible in Figure 4.3(b) due to charging in the SEM). The H-SiN/L-SiN waveguide in Figure 4.3(a) exhibits a vertical sidewall while the sidewall of the H-SiN/QD/L-SiN waveguide shows a slightly sloped profile, in line with the observations discussed in the previous section and demonstrating the reproducibility of our process. As the QDs in the H-SiN/QD/L-SiN stack were subject to a PECVD deposition at 120 °C, their optical quality could have been degraded. In order to verify this, we measured the PL of QDs after embedding them in an H-SiN/QD/L-SiN waveguide and compared it with that of patterned QDs processed at room temperature on top of a SiN waveguide. The result is shown in Figure 4.3(c). In both cases, the PL was excited by illuminating the top of the waveguide with a 447 nm laser diode and then collected from the cleaved facet of a waveguide with a microlensed fiber. It can be seen that, except for a red shift and an increased intensity at longer wavelength due to wavelength-dependent reabsorption and probably also the change of emission profile, the main features of the PL spectrum are well preserved. Because of different pumping and collection efficiencies, it is hard to compare the absolute PL intensities of embedded QDs with those deposited on top of the SiN film. Therefore in Figure 4.3(c) we only show the normalized PL. As demonstrated in our previous work [13], in general there is a reduction in PL intensity after depositing SiN at 120 °C, and this effect is dramatically magnified when increasing temperature (e.g. to 300 °C). We believe that by further improving the quality of the QDs themselves, for example, by increasing the shell thickness for better protection of the core, the wavelength shift and intensity decrease of the PL can further be decreased and higher processing temperature without bringing distinct degradation of optical properties of QDs may be possible.

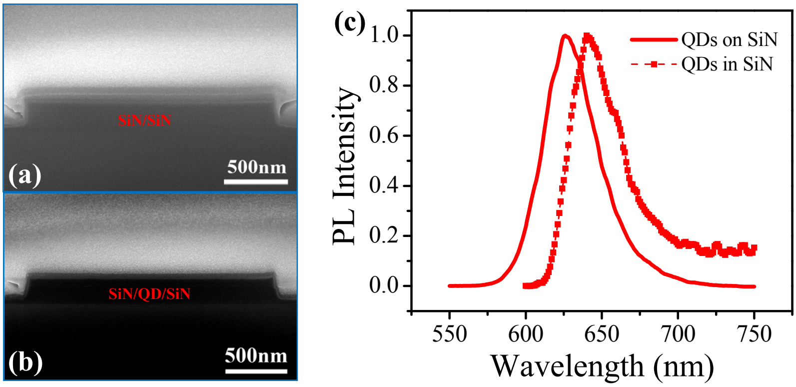

**Figure 4.3:** FIB cross-sectional images of ~200 nm thick, 2 μm wide waveguides for (a) H-SiN/L-SiN and (b) H-SiN/QD/L-SiN structures on 3 μm oxide box. (c) PL spectra of QDs on the top of SiN and embedded in SiN waveguides, respectively.

To evaluate the QD-SiN platform more quantitatively, we measure and extract the propagation losses of SiN and SiN/QD waveguides by using the same method and setup as in Chapter 2. Since the target of this work is to develop and demonstrate a QD-SiN compatible technical platform integrating low-loss passive photonics with efficient photon emitters inside, of primary concern is the optimization of the fabrication process, especially the deposition and etching, and their influence on the waveguide quality. Therefore we measured the waveguide losses at a wavelength of 900 nm to avoid the intrinsic absorption peak of the QD layer and hence the measured loss mainly originates from absorption loss in the SiN layers, scattering loss by surface roughness and non-uniformity in the QD layer and other loss caused by fabrication imperfections. In Figure 4.4 we show the measured results for both H-SiN/L-SiN and H-SiN/QD/L-SiN waveguides. The results exhibit a similar decrease in loss for wider waveguides as discussed before for SiN waveguides in Chapter 2. We obtain losses as low as 1.82 dB/cm and 2.69 dB/cm for the widest H-SiN/L-SiN and H-SiN/QD/L-SiN waveguides, respectively. The inset shows the transmission as function of length for these 2μm-wide waveguides and the associated linear fits. However, unlike the significant difference of loss between pure H-SiN and L-SiN waveguides, the loss of the H-SiN/QD/L-SiN waveguide stably remains 1–2 dB/cm larger than that of the H-SiN/L-SiN waveguide for all measured widths as seen in Figure 4.4. It is clear that this loss difference comes from the presence of QDs in the H-SiN/QD/L-SiN waveguides. As shown in the etched profile, the sidewalls of the H-SiN/QD/L-SiN waveguide are slightly sloped and a bit rougher than those of the waveguides without embedded QDs. In addition, the QD layer can introduce some roughness at the interfaces of the layer deposited on top, for instance, due to the imperfections in the LB deposited QD layer. All of these could account for the 1–2 dB/cm increase in loss for the H-SiN/QD/L-SiN waveguides compared to the H-SiN/L-SiN waveguides.

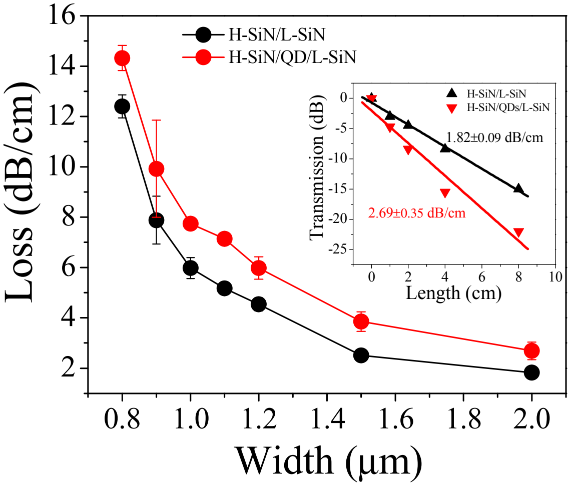

**Figure 4.4:** Waveguide losses at different widths of H-SiN/L-SiN and H-SiN/QD/L-SiN stacked layers, obtained by linearly fitting waveguide-length dependent transmission. The inset shows the normalized transmissions of 2 µm wide waveguides at different lengths together with the corresponding linear fits of the slopes for different types of waveguide, indicating a very small discrepancy between the measured and fitted results.

Summarizing, we have developed a platform for the hybrid integration of SiN photonics with colloidal QDs and demonstrated losses lower than 2.7 dB/cm in the optically active waveguides consisting of a close-packed monolayer of QDs embedded in between SiN layers. Since the entire fabrication of QD-SiN waveguide wires is CMOS compatible, the present platform can take advantages of existing CMOS technology and enable realizing on-chip low-loss SiN devices integrated with active QDs, in particular, the integration with high-Q microcavities for on-chip light sources and even lasers.

## 4.3 On-chip QD-SiN microdisks

On-chip microresonators can allow for manipulation for photon and also serve as ideal platform for studying light-matter interactions. In Chapter 2, we have developed a unique processing technology to realize waveguide-coupled free-standing SiN microdisks and demonstrated high-Q factors in small SiN disks operating from the visible to infrared. Active on-chip resonators will be more appealing in some research fields, for example, controlling the emission properties of emitter and providing optical feedback for lasing.

In this section, we design and fabricate on-chip free-standing SiN microdisks integrated with embedded colloidal QDs. We provide in depth characterization results and according analysis of the performance of active SiN microdisks and also show the ability of controlling accurately the coupling between disk and bus waveguide. Efficient coupling of QD emission to disk modes and eventually to the on-chip waveguides is experimentally realized. Furthermore, the tunability of coupling between disk and bus waveguide through changing geometrical parameters of the design is demonstrated in both experiments and simulations. These active disks exhibit both a high Q factor and a large free spectral range (FSR), making them suitable for further development of on-chip compact laser sources in Chapter 5. The developed approach is also relevant for the study of SiN cavities integrated with a few or a single QD for both fundamental studies and the realization of on-chip single photon emitters.

### 4.3.1 Design and fabrication of QD-SiN microdisks

The proposed configuration for the QD-SiN disk vertically coupled to an access waveguide is schematically shown in Figure 4.5(a). The structure is the same as the passive SiN disk designed in Chapter 2. We employ the $SiO_2$-based chemical mechanical planarization (CMP) process and the associated design. In particular, the disk consists of sandwiched SiN/QD/SiN layers with the embedded QD layer at the center. The structural parameters are adapted to make the device working at ~625 nm, the central emission wavelength of the QDs employed. The undercut distance ($d$) is ~3 μm to prevent leakage loss of the fundamental transverse-electric (TE) whispering gallery modes (WGMs) to the amorphous Si (aSi) pillar. To tune the coupling strength, the horizontal offset is varied from -400 nm to +400 nm. From finite-difference time-domain simulations (FDTD) [15], we adopt a height of ~125 nm for the bus waveguide, guaranteeing single TE mode operation at a wavelength of ~625 nm. The total disk height, including the top and bottom SiN layer and the QD layer was set to ~170 nm to ensure low loss for the fundamental TE WGMs. Both the diameter of the SiN disk and the width of the bus waveguide are varied to investigate their effects on the disk-waveguide coupling and on the coupling of QD emission into disk modes. In Figure 4.5(b), we present the simulated cross-sectional field profiles of the radial component ($E_r$) and intensity ($|\mathbf{E}|^2$) for the fundamental TE mode in a suspended SiN disk with a 7 μm diameter. It is obvious that the field is well centered in SiN layer, ensuring maximum coupling with the QDs. Note also that the suspended configuration makes the mode strongly confined in the disk, implying significantly reduced leakage loss to the substrate. More quantitatively, we simulated the Q-factor as function of the gap between disk and substrate for a mode at around 625 nm in the disk with a 7 μm diameter, as shown in Figure 4.5(c). It can be seen that the substrate has a distinct influence on the Q-factor of the mode. For instance, with only a 150 nm gap a Q factor of $1.3\times10^4$ is obtained, seven times as large as that for a disk directly fabricated on a $SiO_2$ substrate (Q = $1.8\times10^3$). This shows that the vertical coupling configuration allows realizing waveguide-coupled free-standing disks with small diameters while supporting high-Q WGMs, or in other words allows large FSR and small modal volume, essential characteristics in many potential applications. In our design, the vertical gap is fixed at ~200 nm to facilitate coupling of the WGMs to the underneath waveguide. An additional advantage of the vertical coupling scheme is that the fabrication steps for waveguide and disk are separated so that it is straightforward to integrate the QDs locally inside the disk and not in the access waveguides. This offers two distinct benefits: achieving low-loss passive connecting circuits and preventing undesired background signal from QDs elsewhere – critical requirements particularly in the context of low-light studies like controlled photon emitters. Realizing this in a lateral coupling scheme would be considerably more complex.

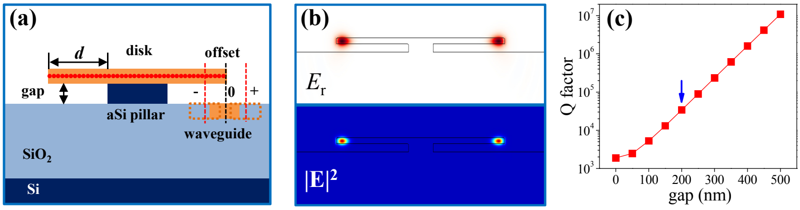

**Figure 4.5:** Cross-sectional view of SiN disk with embedded QDs vertically coupled with on-chip waveguide. (b) Simulated cross-sectional field profiles of radial component ($E_r$) and intensity ($|\mathbf{E}|^2$) for the fundamental TE WGM in suspended SiN disk with a 7 μm diameter. (c) Simulated Q factor (mode wavelength ~625 nm) as a function of coupling gap for a 7 μm diameter disk with 170 nm thickness. The blue arrow indicates the gap of 200 nm used in our devices.

To obtain a quantitative analysis of QD emission coupled to cavity modes, we approximately regard the QD as a dipole oscillator and calculate the power coupling efficiency ($\eta$) of the dipole radiation to the disk mode by performing FDTD simulations, as shown in Figure 4.6. It is clearly seen that for the TE WGM the main contribution of $\eta$ is from the $r$-polarized dipole as expected and that the maximum efficiency reaches 54% when the dipole is located at the center of the layer. When moving the dipole towards the top of the layer, $\eta$ decreases quickly to a value of 14.6% for the dipole on the top. On average, we can achieve 3.7 times enhancement of coupling efficiency by embedding the QD emitter right inside the disk compared to the placement on the surface, and this improvement is essential for boosting emitter-mode interactions.

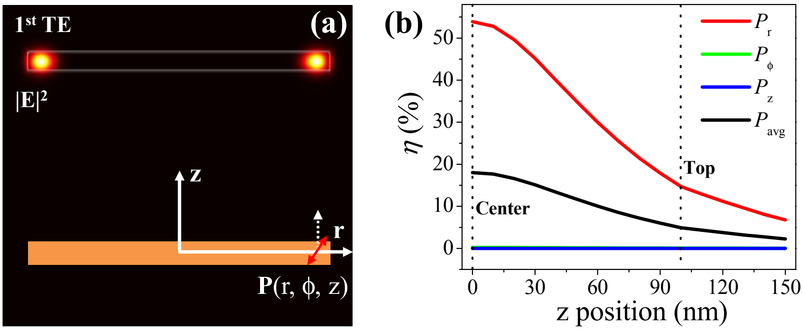

**Figure 4.6:** Coupling of a dipole radiation to the disk mode. (a) Upper: simulated field profile of the 1st TE WGM in the SiN disk with 7 μm diameter and 200 nm thickness in air. Lower: schematics of a dipole oscillator **P**(r,ϕ,z) as indicated by the red arrow inside the disk with an offset of 200 nm in r axis with respect to the edge of disk. (b) Calculated power coupling efficiency ($\eta$) for different polarizations of the dipole oscillator to the 1st TE WGM as a function of dipole position in z axis, at ~630 nm.

The fabrication flow of the device is similar to that of the $SiO_2$-CMP SiN disk in Chapter 2, as schematically shown in Figure 4.7. Firstly, a 125 nm thick SiN film is deposited onto a wafer with a 3 μm thermal $SiO_2$ box layer by a PECVD process performed at a temperature of 270 °C. Then the bus waveguide is patterned to form a strip waveguide (see Figure 4.7(a)) that supports only a single TE mode at the designed wavelength. This ensures only the TE WGMs in the disk will be coupled out efficiently. The waveguide is then planarized by depositing a ~800 nm PECVD $SiO_2$ cladding and flattening the surface down to the top of the bus waveguide via a CMP process, as shown in Figure 4.7(b, c). Next, a ~200 nm thick PECVD aSi layer is deposited to define the vertical coupling gap. Then the QD-SiN composite layer is deposited and patterned as depicted in Figure 4.7(d, e). The QD-SiN stacked layer is prepared by successively depositing a ~80 nm bottom SiN, spin-coating nearly a monolayer of QDs, and depositing ~80 nm top SiN for embedding the QDs. To define the disks the optimized etching process for the QD-SiN waveguide is used to obtain smooth and steep sidewalls. The QDs employed in our device are ~10 nm CdSe/CdS core/shell dots prepared according to the "flash" synthesis procedure [16], with a peak PL wavelength around 625 nm. For suspending the disk an alkaline based wet etching step is used. Since this process to some extent can also etch the QDs, an extra protection layer is patterned over the disks to prevent damaging the QDs as shown in Fig. 2(f). We used the commercially available

ProTEK® B3, designed to withstand alkaline solutions, for this purpose. Finally the disk is undercut and the protective layer is removed to realize a free-standing SiN disk supported on aSi pedestal as drawn in Figure 4.7(g, h).

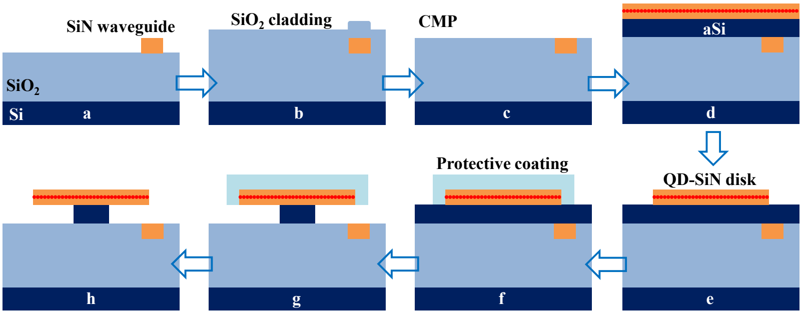

**Figure 4.7:** Schematics of QD-SiN hybrid device fabrication flow. (a) Definition of SiN waveguide. (b, c) SiO$_2$ cladding deposition and CMP Planarization. (d, e) Deposition of aSi gap layer and SiN/QD/SiN films, and definition of QD-SiN disk. (f) Coating and patterning of protective layer. (g, h) Undercut etching of aSi and cleaning of protective layer.

In Figure 4.8(a), we show optical images of fabricated devices with various disk diameters from 7 µm to 20 µm. It is clearly seen that the presently developed approach is capable of realizing on-chip free-standing SiN disk integrated with QDs. In Figure 4.8(b), we show SEM images of a fabricated device with a 7 µm diameter disk suspended on a aSi pillar with a ~3.0 µm undercut distance, under which the bus SiN waveguide is clearly buried in an oxide matrix for on-chip coupling. To check the morphology of the embedded QD layer, we made a FIB cross-sectional image along the dashed red line in Figure 4.8(b) under the protection of a Pt layer deposited in situ by electron beam and ion beam, shown in Figure 4.8(c). The ~10 nm thick QD layer is perfectly embedded between the two layers of SiN and the QD-SiN disk is supported on the aSi layer as expected. In Figure 4.8(d), we show the tilted view of the enlarged disk sidewall area as indicated with dashed red box in Figure 4.8(b) and the sidewall shows a continuously co-etched surface for the composite layers without steps at the interfaces of the different layers, which is an important feature for high quality microdisk resonators.

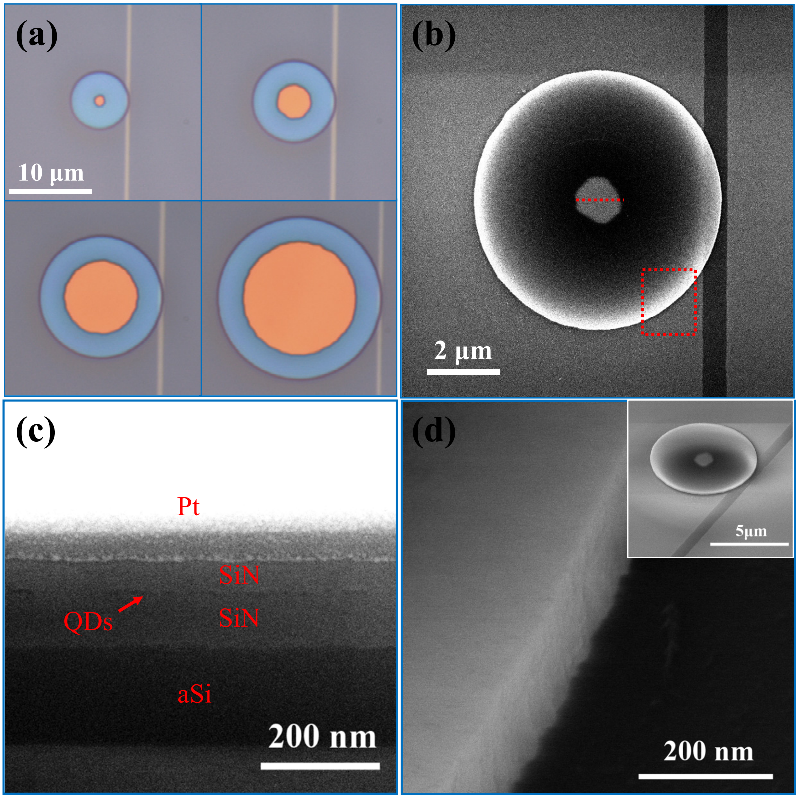

**Figure 4.8:** Fabrication results. (a) A set of optical images of fabricated devices with different disk diameters. All images have the same scale bar of 10 µm as shown in the first left-top image. (b) SEM image of a device with a 7 µm diameter disk. (c) FIB cross-sectional image of the disk taken along the dashed red line in (b). (d) SEM image of the tilted view of the disk sidewall area indicated with dashed red box in (b). The inset shows the whole view of the disk.

## 4.3.2 Device characterization and discussion

### PL characterization for QD-SiN disks

To characterize the PL spectrum of the fabricated devices, we pumped the disks from the top using a 400 nm laser and collected the PL-signal from the cleaved facet of the bus waveguide using microlensed fibers. In Figure 4.9(a) and (b), we show the normalized PL spectra of disks with two different diameters coupled to a ~500 nm wide bus waveguide with an about +160 nm offset, as defined in Figure 4.5(a). The spectra clearly show that the QD emission is successfully coupled to the disk WGMs. Taking advantage of the fact that the 500 nm waveguide bus waveguide is in cut-off for the TM polarized modes, we only couple out the TE WGMs of the disk. For the smallest disk of 7 μm diameter, only the fundamental TE mode family is recorded in the spectrum shown in Figure 4.9(a). This is in agreement with FDTD simulations showing that the higher order modes are lossy and exhibit a low Q-factor in this small disk. When increasing the diameter of the disk, a second family of WGMs starts appearing, as shown in Figure 4.9(b) for the 15 μm disk. This family exhibits a larger FSR and through simulation we can identify it as originating from the 2nd TE radial modes. In the insets of Figure 4.9(a) and 4(b), we also denote the Q-factors of the modes around 622 nm determined by fitting a Lorentzian function. We obtain a Q of 1160 with a FSR of ~8.9 nm for the 7 μm diameter disk and a Q of 4460 with a ~4.15 nm FSR for the 15 μm diameter disk. Note that characterization of the modes with Q above ~4000 as shown in the fitting is already limited by the 0.05 nm resolution of the spectrometer we used.

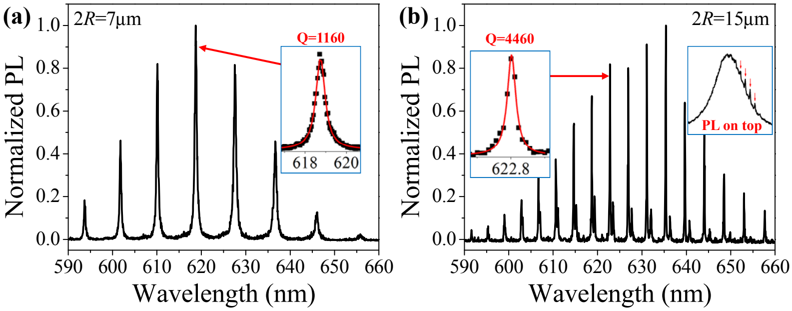

**Figure 4.9:** Normalized PL spectra of the devices coupled to ~500 nm wide waveguides with an offset of +160 nm, for disk diameters of 7 and 15 μm in (a) and (b), respectively. The insets at the right side of (a) and left side of (b) show the fitted Q factors for representative fundamental WGMs as denoted by the red arrows. The right-side inset in (b) shows the PL spectrum collected on top of the disk for comparison.

Another impressive signature of these spectra is that the background PL signal is very strongly suppressed, leading to sharp shoulders between the modes. This can be attributed to two factors – the enhanced interaction between the QD emission and the disk modes and the efficient coupling of the disk modes to the access waveguide. For photonic devices integrated with optical emitters, the background PL typically stems from emission directly radiated to free space (radiation modes) and light coupled to undesired modes, e.g., with an unwanted polarization or mode number. In our case, since the location of the thin QD layer almost perfectly overlaps with the maximum field intensity of the WGMs in the disk, the proportion of QD emission coupled to these disk modes is significantly enhanced compared to that coupled to free space. Second, for collecting the PL we use the single-TE mode bus waveguide, which can efficiently couple out TE modes from the disk while coupling of any other modes as well as any scattered light is strongly suppressed. As a result, the PL spectra exhibit a very low background. For comparison, in the second inset of Figure 4.9(b), we show the PL spectrum as collected on top of the disk. This spectrum is dominated by the broad background PL of the QDs and only a few of the WGMs, as indicated by the red arrows are vaguely visible. Similar spectra reported in previous work [12, 13] show that this background is unavoidable in free-space collection.

The envelope in the PL spectra in Figure 4.9(a) and (b) can arise from the wavelength-dependent emission of the QDs itself but also from the wavelength-dependent disk-waveguide coupling strength. We believe the first effect actually plays the primary role. To verify this we prepared a SiN/QD/SiN slab waveguide using the similar process as depicted in Figure 4.7. In Figure 4.10(a) we show the PL spectrum of this slab waveguide together with that of the original QD solution. It can be seen that these spectra match well with the envelope of the device spectra in Figure 4.9(a) and (b). Nevertheless, it should be mentioned that the wavelength-dependent coupling coefficient in the vertical coupling scheme cannot be neglected under some circumstances, for instance, when changing the coupling offset, we also observe a considerable shift in the PL spectra envelopes. It is also important to note that, although the absolute intensity may decrease, the PL spectra of the QDs after embedding them in the SiN stack exhibits almost the same peak position and overall profile as the original PL spectra of the QDs in solution.

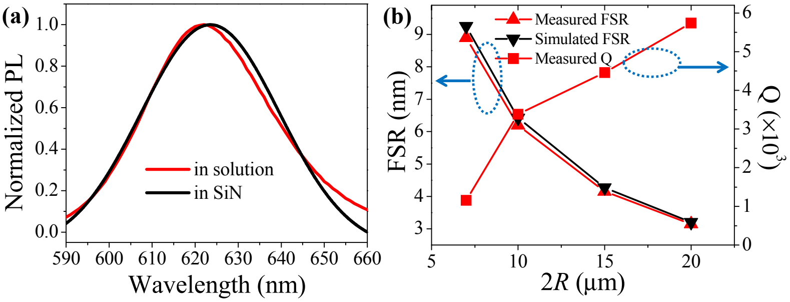

**Figure 4.10:** (a) PL spectra of QDs in solution and in SiN slab. (b) Measured and simulated FSR values and fitted Q factors for different diameter (2*R*) disks. For a fair comparison, both FSR and Q are calculated for the modes around ~622 nm, and Q factors are measured for the devices with ~500 nm waveguide width and +160 nm offset.

In Figure 4.10(b), we plot the Q-factor and FSR for devices with various disk diameters but a constant bus waveguide width of ~500 nm and offset of +160 nm (measured around ~622 nm). A highest Q of 5740 and a FSR of 3.15

nm is achieved in the 20 μm diameter disk, an impressive result for such an active cavity. For the smallest disk, we attain a FSR of 8.9 nm and a moderate Q of 1160 (up to Q~1800 for some devices), promising for single-mode and low-threshold QD-based lasers on chip. The quality of the devices can still be improved by further optimizing the fabrication process, to attain a more uniform QD layer and smoother sidewalls, both factors reducing the scattering loss. We also present the simulated FSR values for different diameters in Figure 4.10(b). In the simulation we assumed the disks were fabricated from a uniform SiN-layer with refractive index of 1.94 and thickness of 170 nm. The gap is fixed at 200 nm. The simulated results show good agreement with the measured values, with a discrepancy less than 4%, which can be attributed to small variation of the refractive index and dimensional and structural deviations between the designed and actually fabricated devices.

## Tunability of the coupling strength

In a vertical coupling configuration, since the mode centers for different modes are spatially separated along the radial direction, the coupling coefficients for one family of modes can be tuned relatively to those of a different radical order by changing the offset between the bus waveguide and the disk or by adjusting the width of the bus waveguide. In fact, this tunability has already been studied in passive SiN disks in Chapter 2. In active devices it is of practical importance, for example, to control the external efficiency of lasers. To investigate this further, we fabricated devices with varying offsets as well as varying bus waveguide widths. In Figure 4.11 (a) and (b), we show PL spectra of devices with a disk diameter of 10 μm and a 500 nm wide bus waveguide, having an offset of +60 nm and +160 nm, respectively. The spectra were not normalized and care was taken to take the experimental conditions constant so the absolute value of the recorded intensity can be compared between both configurations. When moving the bus waveguide away from the disk edge (i.e., increasing the offset to +160 nm), obviously the PL spectra evolve from a strong to a relatively weak coupling regime, with the overall light intensity coupled out decreasing by ~2.4 times. At the same time the Q-factor for the central peak is increasing by ~2 times. The possibility to efficiently and accurately tune the coupling strength comes from the strongly offset dependent coupling coefficient and is another advantage of the presented vertical coupling scheme. In Figure 4.11(c), we also show the simulated offset-dependent power coupling efficiency ($\eta$) between the fundamental TE waveguide mode and the fundamental TE WGMs in the disk with a diameter of 10 μm. The simulation is similar to that performed in Chapter 2 but is carried out at around 625 nm. Note that the parameter settings in the simulation are taken from the actually fabricated devices. With changing the offset from +60 to +160 nm, $\eta$ decreases from 2.4% to 0.8% as indicated by the red arrows in Figure 4.11(c), which can account for the decrease of the out-coupled PL intensity in Figure 4.11(a) and (b).

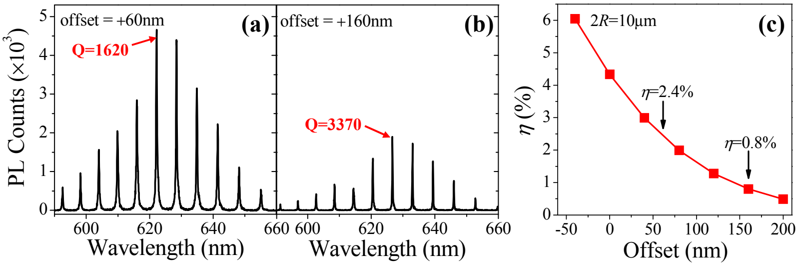

**Figure 4.11:** PL intensity spectra of the devices with a disk diameter of 10 μm and a 500 nm wide bus waveguide but under different offsets of +60 nm and +160 nm in (a) and (b), respectively, together with Q-factors for the central peaks denoted by the red arrows. (c) The simulated offset-dependent coupling efficiency ($\eta$) between fundamental the TE waveguide mode and the fundamental TE WGMs in the disk with a diameter of 10 μm.

Instead of changing the offset, we can also modify the width of the bus waveguide to adjust the degree of coupling between different order disk modes and the bus waveguide. In Figure 4.12(a) and (b), we show the PL spectra of devices with a disk diameter of 20 μm and an offset of +160 nm, coupled respectively to a 500 nm and 650 nm bus waveguide. In this case the PL spectra were normalized to compare the change of coupling ratio of different order modes. The 20 μm diameter disk supports also higher order TE radial modes and these can be coupled out to the bus waveguide with considerable efficiency as clearly shown in Figure 4.12(a). From their FSR, we can designate the two sets of modes as the 1st and 2nd TE radial order mode families as denoted by the red and blue arrows for a fraction of the spectrum in the insets of Figure 4.12(a) and (b). By widening the bus waveguide, coupling of the 1st order modes can be enhanced with respect to the 2nd order modes as clearly illustrated in the inset of Figure 4.12(b), for example, the PL intensity ratio of the 1st to 2nd order modes increases from 1.84 to 6.25 for the modes nearby 625 nm. The reduced coupling for 2nd order modes towards the wider waveguide can be explained by the fact that the fundamental mode in this wider waveguide is more strongly confined, reducing the overlap between this waveguide mode and the 2nd order disk modes, resulting in a rather weak coupling for these modes. The maximum electrical field of the 1st order modes on the other hand is located closer to the edge of disk, which ensures the spatial overlap with the waveguide mode remains substantial. From the simulated $\eta$ for the 1st and 2nd order modes shown in Figure 4.12(c), it is indeed obvious that widening the waveguide width from 400 nm to 800 nm the coupling strength for the 2nd order modes decreases while it increases for the 1st order modes, leading to an enhanced coupling ratio of the 1st to 2nd order modes consistent with the measured results in Figure 4.12(a) and (b). Finally, off course also adapting the gap between the free-standing disk and the waveguide offers an additional degree of freedom in engineering coupling efficiency as well as Q factor. The demonstrated tunability of coupling efficiency and cavity Q-factor could potentially be employed in further development of light sources, for example, in laser devices for tuning such parameters as threshold, line-width, and mode control.

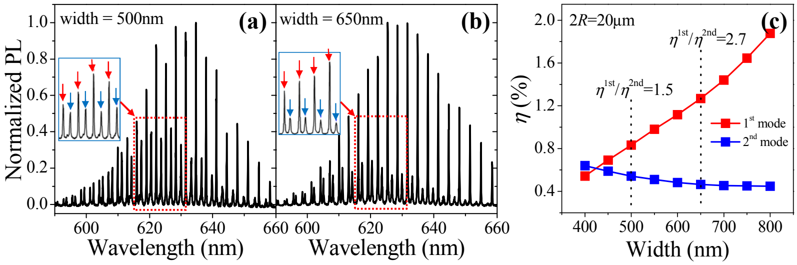

**Figure 4.12:** Normalized PL spectra of the devices with a disk diameter of 20 μm and an offset of +160 nm but under different bus waveguide widths of 500 nm and 650 nm in (a) and (b), respectively. The insets show the zoom-in spectra for the selected regions as indicated with the red-dashed boxes. The red and blue arrows in the insets designate the 1st and 2nd order mode families, respectively. (c) The simulated waveguide width-dependent coupling efficiency between fundamental TE waveguide mode and 1st and 2nd order TE WGMs in the disk with a diameter of 20 μm.

## 4.4 Conclusion

We have developed a platform for the hybrid integration of SiN integrated circuits with colloidal QDs and demonstrated low-loss QD-SiN waveguides with the preservation of QD luminescence. On the basis of this platform and previously developed fabrication technology, we designed and fabricated free-standing SiN microdisks hybridly integrated with embedded colloidal QDs, with those disks coupled to an on-chip access waveguide in a vertical coupling scheme. The detailed PL characterization of the fabricated devices revealed both high performance – high quality factors together with large free spectral ranges – and an efficient coupling of QD emission to disk resonance modes and eventually to the on-chip waveguide. Furthermore, by changing geometrical parameters associated with the proposed vertical configuration, the coupling between the disk whispering gallery modes and the bus waveguide could be efficiently and accurately tuned. The presented optically active devices provide new opportunities not only for the on-chip SiN photonics community but also for the development of novel optoelectronic devices based on QDs.

In particular, the demonstration of on-chip QD-SiN microresonators with high performance could be also realized in the combination with the colloidal QDs with optical gains, as already demonstrated, toward on-chip SiN lasers based on QDs. This exploration will be carried out in next section.

# References

[1] D. Liang and J. E. Bowers, “Recent progress in lasers on silicon,” Nat. Photonics **4**(8), 511-517 (2010).

[2] Z. C. Wang, B. Tian, M. Pantouvaki, W. M. Guo, P. Absil, J. Van Campenhout, C. Merckling, and D. Van Thourhout, “Room-temperature InP distributed feedback laser array directly grown on silicon,” Nat. Photonics **9**(12), 837-842 (2015).

[3] A. P. Alivisatos, “Semiconductor clusters, nanocrystals, and quantum dots,” Science **271**(5251), 933-937 (1996).

[4] G. Schmid, ed. *Nanoparticles: from theory to application* (John Wiley & Sons, 2011).

[5] A. L. Efros, D. J. Lockwood, and L. Tsybeskov, eds. *Semiconductor nanocrystals: from basic principles to applications* (Springer Science & Business Media, 2013).

[6] L. Martiradonna, T. Stomeo, M. De Giorgi, R. Cingolani, and M. De Vittorio, “Nanopatterning of colloidal nanocrystals emitters dispersed in a PMMA matrix by e-beam lithography,” Microelectron. Eng. **83**(4-9), 1478-1481 (2006).

[7] Y. K. Olsson, G. Chen, R. Rapaport, D. T. Fuchs, V. C. Sundar, J. S. Steckel, M. G. Bawendi, A. Aharoni, and U. Banin, “Fabrication and optical properties of polymeric waveguides containing nanocrystalline quantum dots,” Appl. Phys. Lett. **85**(19), 4469 (2004).

[8] I. Suarez, H. Gordillo, R. Abargues, S. Albert, and J. Martinez-Pastor, “Photoluminescence waveguiding in CdSe and CdTe QDs-PMMA nanocomposite films,” Nanotechnology **22**(43), 435202 (2011).

[9] M. Humer, R. Guider, W. Jantsch, and T. Fromherz, “Integration, photostability and spontaneous emission rate enhancement of colloidal PbS nanocrystals for Si-based photonics at telecom wavelengths,” Opt. Express **21**(16), 18680-18688 (2013).

[10] M. Humer, R. Guider, W. Jantsch, and T. Fromherz, “Integration, photostability and spontaneous emission rate enhancement of colloidal PbS nanocrystals for Si-based photonics at telecom wavelengths,” Opt. Express **21**(16), 18680-18688 (2013).

[11] S. Gupta and E. Waks, “Spontaneous emission enhancement and saturable absorption of colloidal quantum dots coupled to photonic crystal cavity,” Opt. Express **21**(24), 29612-29619 (2013).

[12] A. Qualtieri, F. Pisanello, M. Grande, T. Stomeo, L. Martiradonna, G. Epifani, A. Fiore, A. Passaseo, and M. De Vittorio, “Emission control of colloidal nanocrystals embedded in $Si_3N_4$ photonic crystal H1 nanocavities,” Microelectron. Eng. **87**(5-8), 1435-1438 (2010).

[13] B. De Geyter, K. Komorowska, E. Brainis, P. Emplit, P. Geiregat, A. Hassinen, Z. Hens, and D. Van Thourhout, “From fabrication to mode mapping in silicon nitride microdisks with embedded colloidal quantum dots,” Appl. Phys. Lett. **101**(16), 161101 (2012).

[14] V. Srivastav, R. Pal, and H. P. Vyas, “Overview of etching technologies used for HgCdTe,” Opto-Electron. Rev. **13**(3), 197-211 (2005).

[15] A. F. Oskooi, D. Roundy, M. Ibanescu, P. Bermel, J. D. Joannopoulos, and S. G. Johnson, “MEEP: A flexible free-software package for electromagnetic simulations by the FDTD method,” Comput. Phys. Commun. **181**(3), 687-702 (2010).

[16] M. Cirillo, T. Aubert, R. Gomes, R. Van Deun, P. Emplit, A. Biermann, H. Lange, C. Thomsen, E. Brainis, and Z. Hens, “"Flash" Synthesis of CdSe/CdS Core-Shell Quantum Dots,” Chem. Mater. **26**(2), 1154-1160 (2014).

# 5

# On-chip integrated QD-SiN microlasers

Colloidal quantum dots (QDs) represent an excellent gain material that is amenable to versatile, solution-based processing. Moreover, the gain wavelength in QDs is easily adjustable exploiting size-dependent quantum confinement and correct material choice, perfectly matching the broadband transparency of Silicon Nitride (SiN) photonics. A variety of types of QDs and their 2D counterparts, colloidal quantum wells, have been shown in the past few years to exhibit optical gain at wavelengths that can be readily adjusted from near infrared to visible wavelengths through size quantization and material choice [1-9], providing a perfect match with broadband SiN photonics. Various laser devices exploiting these colloidal gain media have been demonstrated, either using accidental *ad hoc* resonators [10, 11], vertical cavities in which gain materials are embedded between reflectors [5-7, 12], or individual cavities where QDs are coated on the surface [13-22]. Despite the confirmation of QDs as an optical gain medium in microlasers, the lack of a suitable integration process and limited QD stability have inhibited the development of more complex, fully integrated waveguide-coupled laser sources that could propel integrated photonics into radically new applications.

Fabricating on-chip QD-SiN lasers requires an effective methodology to handle solution-processable QDs within a top-down complementary metal-oxide-semiconductor (CMOS) manufacturing process. As pointed out before, such a process should preserve the optical properties of the QDs especially the optical gain and facilitate a strong spatial overlap between the QDs and the resonating optical modes without degrading the optical quality factor (Q) of the hybrid device. Moreover, the QD-SiN resonators need to be coupled with low loss on-chip waveguides to facilitate efficient extraction and further manipulation of the emitted light. In these respects, the use of SiN membranes with locally embedded QD films within a CMOS-like process flow is a potent approach that allows for the combination of active QD-SiN resonators and passive SiN circuits on the same platform, as we have developed and demonstrated in Chapter 4.

In this chapter, we use the same approach to demonstrate a first on-chip QD-SiN microdisk laser coupled to planar SiN waveguides. The microdisk consists of a SiN/QD/SiN sandwich that supports high-Q whispering gallery modes (WGMs) with a maximum of optical confinement in the central QD layer. Lasing is achieved for different disk diameters under picosecond optical pumping. The lasing action is characterized via measuring the photoluminescence (PL) intensity versus pump power, and features a non-linear increase above a very low threshold fluence of 27 $\mu J \cdot cm^{-2}$ for a 7 μm disk. In addition, pronounced spectral narrowing, reduced emission lifetime and enhanced temporal coherence are observed above threshold. These ultra-compact waveguide-coupled QD-SiN microdisk lasers showcase the key building block for realizing active integrated photonics on the SiN platform. Our approach opens up new paths for optical communication, lab-on-a-chip, gas sensing and, potentially, on-chip cavity quantum electrodynamics and quantum optics.

## 5.1 Optical properties of QDs

In this section, we investigate the optical properties of the QDs to be integrated in a SiN microdisk. First, we describe the synthesis and linear optical properties of the QDs used. Then we describe the intrinsic gain properties determined using transient absorption spectroscopy[4]. We then study the optical index and absorption coefficient of SiN-embedded QD films.

### 5.1.1 QD synthesis and linear optical properties

---

[4] The QDs were synthesized by Dr. Tangi Aubert. The transient absorption spectroscopy was carried out by Suzanne Bisschop.

The CdSe/CdS QDs were prepared according to the *flash* synthesis procedure [23]. This technique consists of a fast and high temperature seeded growth process that has proven to be very efficient for the synthesis of large core-shell QDs with robust optical properties. First, 3.6 nm wurtzite CdSe QDs were synthesized according to the method reported by Carbone *et al.* [24], whereby tetradecylphosphonic acid was used instead of octadecylphosphonic acid for ease of of the purification process. These CdSe QDs were then used as seeds for the growth of a CdS shell in a single *flash* procedure. Briefly, 189 mg of CdO mixed with 10 g of trioctylphosphine oxide and 2.5 g of oleic acid were degassed under nitrogen at 120 °C for 1 h. The mixture was subsequently heated to 330 °C at which point 2 mL of trioctylphosphine were injected. After the temperature had recovered to 330 °C, 250 nmol of the CdSe cores dispersed in 2 mL of trioctylphosphine solution with 1.2 mmol of S dissolved beforehand was injected. After 5 min, the reaction was quenched by using a water bath, resulting in CdSe/CdS core/shell QDs with a total diameter of 9.1 nm. The QDs were precipitated and further purified 3 times using toluene and methanol as solvent and non-solvent. Finally, the QDs are dispersed in toluene and the concentration can be adjusted to obtain a desired thickness of QD film by spin-coating.

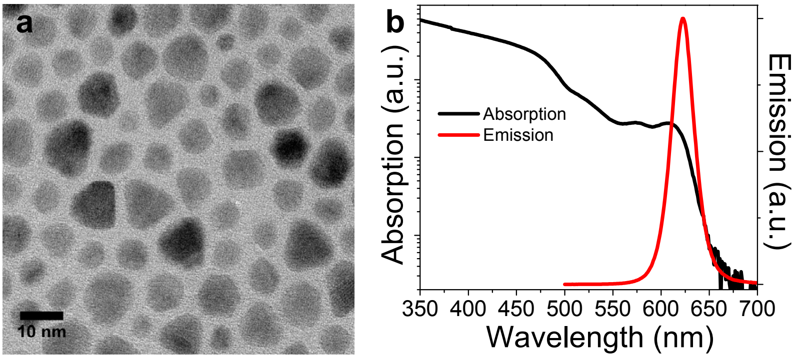

**Figure 5.1:** Morphological and optical properties of the CdSe/CdS QDs. (a) TEM image. (b) Absorption and emission spectra in solution.

Figure 5.1(a) shows the transmission electron microscope (TEM) image of the CdSe/CdS QDs used in this study. These QDs are made of a 3.6 nm CdSe core for a total diameter of 9.1±2.2 nm. Figure 5.1(b) shows the absorption and emission spectra of the CdSe/CdS QDs used here as measured on an ensemble in a toluene solution. Due to the large volume of the CdS shell, the absorption curve is dominated by the bulk-like CdS absorption below 500 nm, whereas the first exciton transition of the CdSe cores can still be identified at 608 nm. The QDs have an emission centered at ~625 nm with a full-width at half-maximum (FWHM) of ~30 nm, a typical value for colloidal CdSe/CdS QDs. The emission band is attributed to the bandgap transition of the QD cores. The quantum yield is about 50% as measured relatively to an organic dye.

### 5.1.2 Optical gain measurement in solution

To assess quantitatively the optical gain characteristics of the CdSe/CdS QDs used here, we first determine the non-linear absorbance of a CdSe/CdS QD dispersion using transient absorption spectroscopy. A pulsed laser at $\lambda$ = 520 nm is used as pump (an automated optical parametric amplifier for wavelength extension of a regeneratively amplified Ti: Sapphire laser, ≈100-200 fs pulse duration, 1 kHz repetition rate) and a pulsed broadband as probe (by supercontinuum generation with a linearly polarized near-IR 800nm pump in a calcium fluoride crystal, ≈100-200 fs pulse duration, 1 kHz repetition rate). We can extract the material gain $g_\mathrm{m}$ of the used QDs from the measured non-linear absorption $A$ using $g_\mathrm{m} = -\ln(10) \cdot A/(fL)$, with $f$ the volume fraction and $L$ the length of the cuvette.

Figure 5.2(a) shows the material gain as a function of wavelength for different pulse energies at a fixed delay of 4 ps. It can be seen that optical gain is first attained at 638-655 nm once the pump pulse energy exceeds 38.7 μJ·cm$^{-2}$. At higher pump energies the QDs have a very broadband, up to 74 nm wide, gain-band and a maximal gain of about 930 cm$^{-1}$ at a wavelength of 623 nm can be reached when the QDs are pumped with pump energy 95 μJ·cm$^{-2}$. The corresponding non-linear absorbance as a function of time at a fixed probe wavelength of 620 nm is shown in Figure 5.2(b). It shows that at this same higher pump energy, a situation of population inversion and optical gain lasts up to 80 ps. Fitting the relaxation of the transient absorbance to a single exponential yields a decay rate of 4 ns$^{-1}$, which corresponds to a lifetime of 250 ps. As population-inversion lasts for such long time, we attribute optical gain in these QDs to stimulated emission from biexciton states, where interfacial alloying may somewhat suppress Auger recombination of the biexcitons [11, 25, 26].

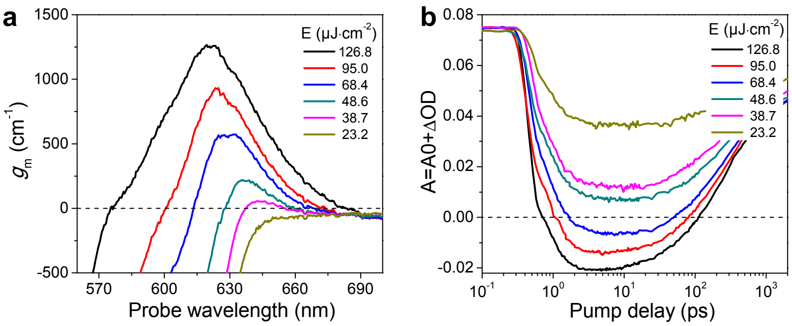

**Figure 5.2:** Transient absorption results. (a) Material gain spectra at a fixed delay of 4 ps at different pump pulse energies. (b) Corresponding time slices at a fixed probe wavelength of 620 nm.

### 5.1.3 Optical properties of QD film

So far, the optical properties of QDs have been studied in solution. For integrated photonic devices, however a solid film of QDs with controlled thickness and uniform surface is needed. Here, we obtain a QD film using spin-coating. Unlike the monolayer of QDs used previously, we employ thicker QD film (e.g., tens of nanometer) in order to provide sufficient optical gain. For optimizing the design of SiN photonics devices and for the quantitative assessment of the possible device performance, the optical properties of such a QD film hence need to be determined before integration with SiN resonators.

First, we measure the optical refractive index of the QD film using ellipsometry. The QD film is prepared directly on a silicon substrate and the real and imaginary parts of optical index ($n$, $k$) are simultaneously obtained by fitting the Cody-Lorentz model [27] to the measured data. Then the absorption coefficient can be deduced from the $k$. However, since the $k$ is sensitive to fitting models, for more reliable values we directly determine the absorption of the QD film through measuring the transmission $T$ and the reflection $R$ ($A = 1 - T - R$) for the SiN/QD/SiN (~100/55/100 nm) layer stack to be used also for fabricating the disk, deposited on a glass substrate. This layer stack is prepared by successively depositing a 100 nm bottom SiN layer, spin-coating a 55 nm layer of QDs, and depositing another 100 nm top SiN layer to encapsulate the QDs. SiN was deposited using our plasma-enhanced chemical vapor deposition (PECVD) system operating at a temperature of 270 °C. All SiN layers were prepared using low-frequency PECVD, except for the top SiN layer of the SiN/QD/SiN sandwich, which was deposited using a mixed frequency mode so as to reduce stress in the SiN layer and prevent cracks. In Figure 5.3 we present the morphological results of the SiN/QD/SiN layer stacks after top ~100 nm SiN deposition. It is clear that the low-frequency SiN deposition on the QD surface regularly induces wrinkles with scale of tens of microns on the entire surface of the QD film as shown in Figure 5.3(a), probably due to high compressive stress in this SiN film and weak QD-QD adhesion. The wrinkled surface can be cracked and peeled off easily by nitrogen blowing or wetting and is useless for further processes. On the other hand, the mixed-frequency mode deposition results in a compact stack and a neat surface as seen in Figure 5.3(b), possibly due to significantly reduced stress in this SiN layer. Moreover, this layer stack exhibits mechanically robustness and can survive further processes such as lithography, dry etching, and wet cleaning even under ultrasonic. It is also notable that there is no observable difference between high- and mixed-frequency SiN deposited in our PECVD system.

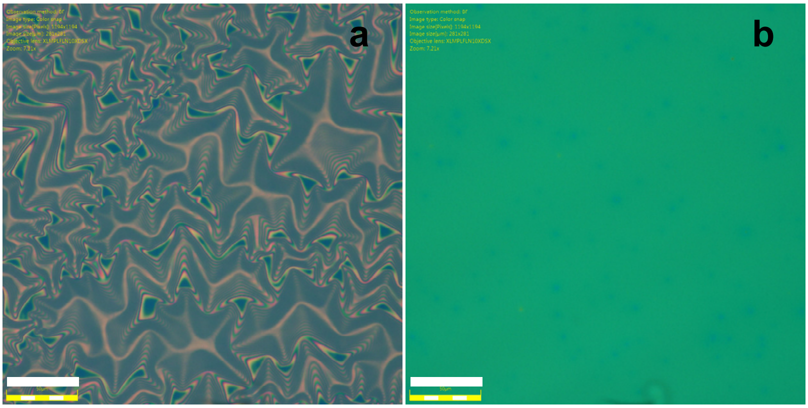

**Figure 5.3:** Optical microscope images of the surface morphologies of SiN/QD/SiN layer stack after deposition of top SiN at different PECVD frequency mode. (a) Low-frequency and (b) mixed-frequency modes. The scale bar is 50 μm.

In Figure 5.4 we show the optical index *n* and absorption coefficient $\alpha$ of a QD film as a function of wavelength. At ~630 nm the index is 1.88, which is close to that of the SiN film (1.9-1.94). This index matching facilitates straightforward device design in terms of mode control in the disk and coupling to the bus waveguide. The absorption coefficient exhibits a value of $2.78\times10^4$ $\text{cm}^{-1}$ at wavelength of 400 nm which we use to excite the QDs in devices.

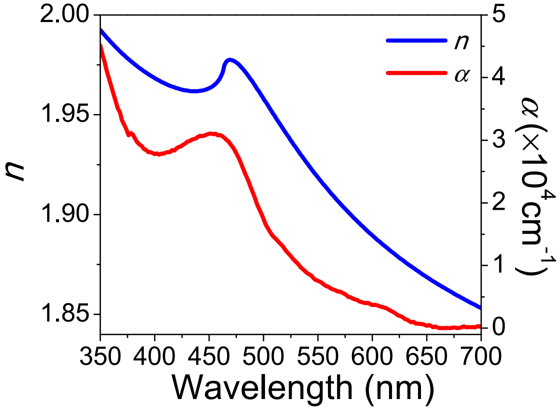

**Figure 5.4:** Measured optical index *n* and absorption coefficient $\alpha$ of SiN/QD/SiN film.

## 5.2 Optical properties of QD-SiN waveguide

In this section, we fabricate QD-SiN waveguides and characterize their linear and nonlinear emission properties. Using a variable stripe length method, we determine the optical gain in the QD-SiN waveguide.

### 5.2.1 Fabrication of QD-SiN waveguide

The QD-SiN waveguide is defined in the same (100/55/100 nm) SiN/QD/SiN layer stack as described before on a silicon substrate with a 3 µm thermal oxide layer, similar to the waveguide fabrication in Chapter 4. Specifically, the reactive ion etching (RIE) process uses the gases of $CF_4/H_2$ (40sccm/5sccm), which slightly differs from the etching condition for previous monolayer QD film in SiN, to attain smooth and steep sidewalls, which are critical for further fabricating high performance disk resonators.

To check the quality of the SiN/QD/SiN layer stack and the etching profile, we made scanning electron microscope (SEM) images of the cross section of as-etched QD-SiN waveguides, as shown in Figure 5.5. They were prepared using focused ion beam (FIB) milling under the protection of a platinum (Pt) layer, deposited *in-situ* by electron and ion beams. It is obvious that an epitaxial-like layer of QDs with a thickness of ~55 nm is perfectly embedded between the two layers of SiN. The sidewall shows a continuously co-etched surface without distinct steps at the interfaces of the different layers, an important feature for guaranteeing high-Q WGMs in the disk.

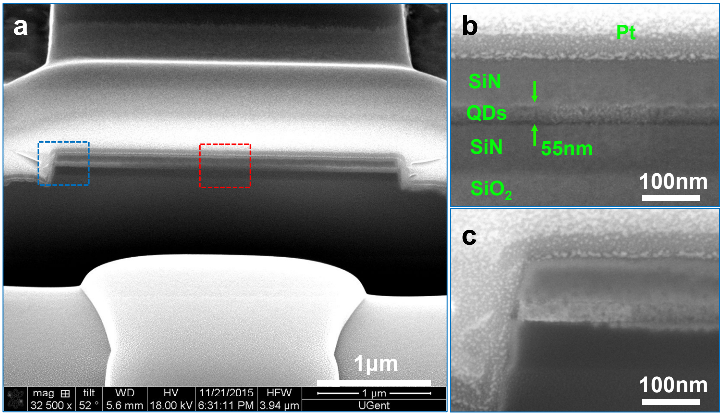

**Figure 5.5:** SEM images of the cross section of as-etched QD-SiN waveguide. (a) Overview of the waveguide. (b) Enlarged view of a selected area in the center of the waveguide as denoted by the red-dashed box in (a). (c) Enlarged view of the etched sidewall as denoted by the blue-dashed box in (a).

### 5.2.2 Emission properties

The emission of the QDs embedded in SiN waveguides is characterized on a micro-PL (μ-PL) setup using an optical fiber for collecting the signal from the cleaved facet of a waveguide defined on the chip. The waveguide was pumped by focusing light from a continuous-wave (CW) laser running at a wavelength of 400 nm to a rectangular pattern using a cylindrical lens. The PL spectrum, as presented in Figure 5.6, shows a peak centered at 625–630 nm and a ~30 nm FWHM, similar to the result measured in solution, demonstrating that the optical properties are well preserved after integration with SiN. Due to wavelength-dependent reabsorption dominating at the blue side of the emission band, the spectra exhibit an asymmetry and a redshift of the PL peak as a function of waveguide length. The latter can be seen in the inset of Figure 5.6. This effect will be also evident in PL from a disk and can significantly deteriorate the Q factors of WGMs at shorter wavelengths, as will be seen later.

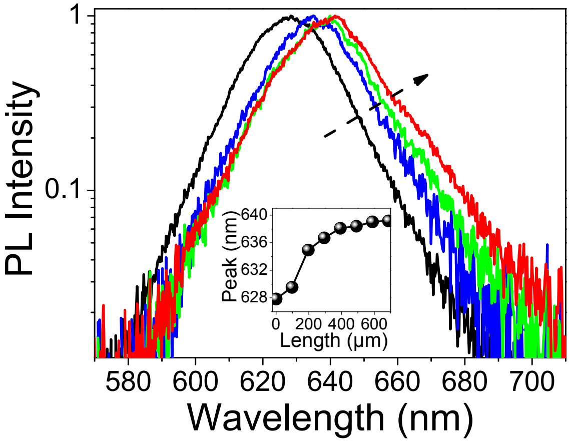

**Figure 5.6:** Normalized PL spectra of QD-SiN waveguides with length increasing from 0 to 700 μm. The arrow indicates increasing waveguide length. The inset shows the PL peak shift as function of the waveguide length. The pump profile is a stripe along the waveguide.

### 5.2.3 Optical gain measurement

The modal gain of QD-SiN waveguides can be determined using a variable stripe length method. Figure 5.7(a) shows the optical emission of a waveguide having dimensions of 600 μm in length and 5 μm in width. Upon pumping the waveguide using 400 nm femtosecond pulsed laser light focused by a cylindrical lens to a rectangular stripe, a broadband spontaneous emission spectrum is recorded from the cleaved edge of the waveguide. Increasing pump power results in a marked narrowing and amplification of the spontaneous emission (ASE). The superlinear intensity increase saturates at a pump power ≈1.8 times above threshold power $P_{\mathrm{ASE}}$ and the corresponding ASE spectrum is centered at ≈627 nm with a FWHM of ≈8 nm. Consequently, we conclude that our process flow for the SiN/QD/SiN stacks preserves the gain characteristics of the CdSe/CdS QDs.

In order to quantify this gain, we analyzed the emission from several SiN/QD/SiN waveguides with dissimilar lengths while maintaining a constant pump power density. Observation of Figure 5.7(b) reveals a sharp, superlinear rise in emission intensity for waveguides longer than ≈200 µm that saturates for lengths exceeding ≈400 µm. As seen in the microscope images, this ASE signal is perfectly guided by the waveguide without observable scattering, and thus corroborates the low intrinsic losses of the QD-SiN waveguides. We estimate the net modal gain $g$ by fitting the distance-dependent intensity to $I = A_0(e^{gl} - 1)/g$ [28] within the region of exponential intensity increase. Averaged over several sets of nominally identical waveguides, net modal gains of around 70 cm$^{-1}$ and 100-120 cm$^{-1}$ are obtained for pump powers of about 1.4×$P_{\mathrm{ASE}}$ and 2×$P_{\mathrm{ASE}}$, respectively. The resulting numbers are in line with expectations. Considering a modal confinement of 23% and QD volume filling factor of ≈53% (estimated from effective index), these correspond to a material gain of up to 980 cm$^{-1}$, which is comparable to the material gain as deduced from the transient absorption measurement.

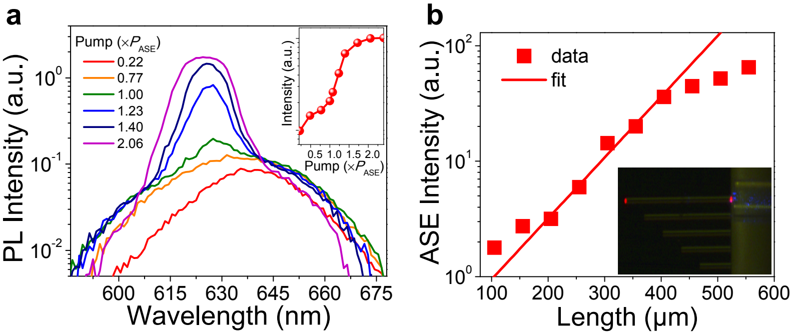

**Figure 5.7:** Optical gain in QD-SiN waveguide. (a) The evolution of ASE spectra for ≈600 µm long SiN/QD/SiN waveguide when increasing the pump power. The latter is normalized to the pump power for which ASE starts dominating SE, $P_{\mathrm{ASE}}$ (≈20 µJ·cm$^{-2}$). The integrated ASE intensity as a function of pump power is shown in the inset. (b) ASE intensity versus the length of the waveguide at an excitation level of ≈2$P_{\mathrm{ASE}}$. The inset shows an optical microscopic image where the ASE signal in the waveguide is well-guided and appears as red emission from the waveguide's left and right end facets.

## 5.3 On-chip QD-SiN microdisk laser

In this section, we design and fabricate a waveguide-coupled QD-SiN microdisk laser. The characterization of the WGMs in QD-SiN disk will be given in detail. In particular, the analysis of Q factors together with measured optical gain will allow for quantitative prediction of lasing in further measurement.

### 5.3.1 Design and simulation

Figure 5.8(a) depicts the schematics of the device configuration with a SiN-QD microdisk vertically coupled to a passive bus waveguide. The details of the design are similar to the waveguide-coupled microdisk device in Chapter 4, while for simplification of fabrication here the top SiN-QD disk is directly built on the $SiO_2$ planarized SiN waveguide layer with a vertical spacing as coupling gap. In the horizontal direction, the disk edge is aligned to the center of the waveguide with an offset as schematically depicted in Figure 5.8(b). The whole device is constructed on a Si wafer with a 3 μm thermal $SiO_2$ layer. From finite-difference time-domain simulations (FDTD), we adopt a height of ~125 nm for the bus waveguide, guaranteeing only fundamental transverse-electric (TE) and transverse-magnetic (TM) mode operation near the wavelength of ~625 nm, the central emission wavelength of the QDs to be integrated. It should be added that we focus preferably on TE mode operation whereas both low-loss TE and TM modes can be supported in such waveguide with oxide cladding. The thickness of the disk is chosen to be ~250 nm to ensure high-Q fundamental (1st radial order) quasi-TE (referred to as TE hereafter for simplicity) WGMs, for example, FDTD simulations indicate a 7 μm × 0.25 μm monolithic SiN disk supports fundamental TE WGM with a simulated Q factor of $\approx 5\times10^4$ at 625 nm. The main parameters for controlling the coupling strength include the coupling gap, the waveguide width, and the offset. In the experiment, the gap is fixed at ~300 nm. Both the waveguide width and the offset are varied to tune the coupling strength. The influence of these parameters on the device characteristics have been discussed in Chapter 4.

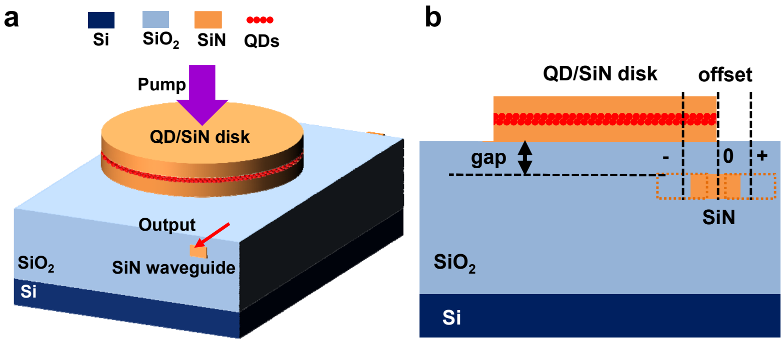

**Figure 5.8:** Design of the device. (a) Schematics of vertical coupling configuration of a QD-SiN disk and an access waveguide. A layer of QDs is embedded in the SiN disk (b) Cross-sectional view of the device.

In the 250 nm-thick SiN disk, both TE and TM WGMs at ~625 nm are supported and can be coupled to TE and TM waveguide modes, respectively. In Figure 5.9(a) we present the FDTD simulated cross-sectional field-intensity profiles of the typical 1st order TE/TM WGMs in the SiN disk with 7 µm diameter on a SiO$_2$ substrate. It is obvious that the field of the 1st order TE mode is well centered in the SiN layer. In Figure 5.9(b) we plot the field intensity profile along the vertical direction (**v**) of the disk for the 1st order TE mode. It is obvious that the maximum intensity is located at the center of the disk, and quantitatively there is more than two times enhancement of the optical confinement at the center compared to the disk top or bottom, integrated over a 50 nm-thick region. Since the effective index of the QD film and the deposited SiN are similar, thus the same enhancement is expected for the optical confinement in the QD layer of a SiN/QD/SiN sandwich and the embedding scheme ensures maximum overlap of the optical field with the QD layer providing gain. We also analyzed the Q factors (radiation loss limited $Q_{\text{rad}}$) of the 1st order TE/TM modes for disks with different diameters and show the result in Figure 5.9(c). Clearly, the 1st order TE WGMs have higher Q factors than the 1st order TM WGMs. Additionally, the 1st order TE WGMs exhibit a larger free spectral range (FSR) as shown in Figure 5.9(d). These properties, in addition to the later mentioned polarization analysis can be used to distinguish between the two sets of modes in the experiment.

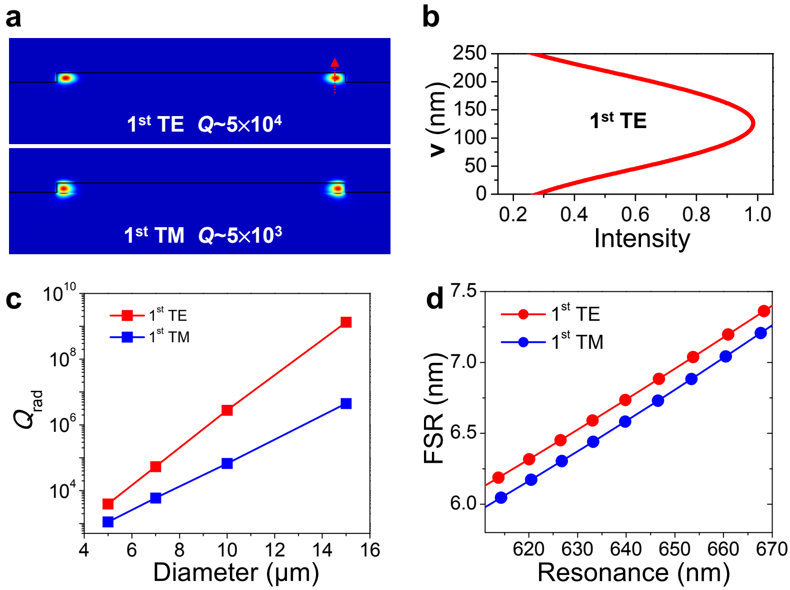

**Figure 5.9:** Simulation of WGMs in SiN disk. (a) Simulated cross-sectional electric field-intensity profiles of the 1st order TE/TM WGMs in a 7 μm-diameter and 250 nm-thick disk on oxide. (b) The electric field intensity distribution for the 1st order TE mode along the vertical direction of the disk, as indicated by the red arrow in (a). (c) Simulated Q factors for the 1st order TE/TM WGMs (resonance wavelength ~625 nm) as a function of disk diameter. (d) Calculated FSR for the 1st order TE/TM WGMs of a disk with 10 μm diameter.

### 5.3.2 Device fabrication

In Figure 5.10, we schematically show the fabrication flow of the designed device. First, we fabricate the SiN waveguide chip with planarized oxide cladding by $SiO_2$-based chemical mechanical planarization (CMP) process developed previously, starting from a low-frequency PECVD SiN layer on top of a 3 μm thermal oxide layer. Then the QD-SiN disks, aligned to the bottom bus waveguides, are defined in a uniform (~100/55/100 nm) SiN/QD/SiN layer stack prepared by the same procedure as used in QD-SiN waveguide fabrication, using a photoresist mask and the optimized RIE process.

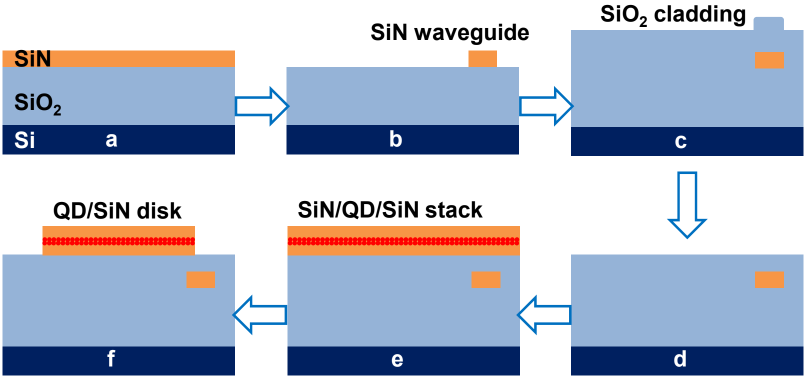

**Figure 5.10:** Schematics of device fabrication flow. (a, b) SiN deposition and waveguide definition. (c, d) $SiO_2$ deposition and CMP planarization. (e, f) Preparation of SiN/QD/SiN layers and QD-SiN disk definition.

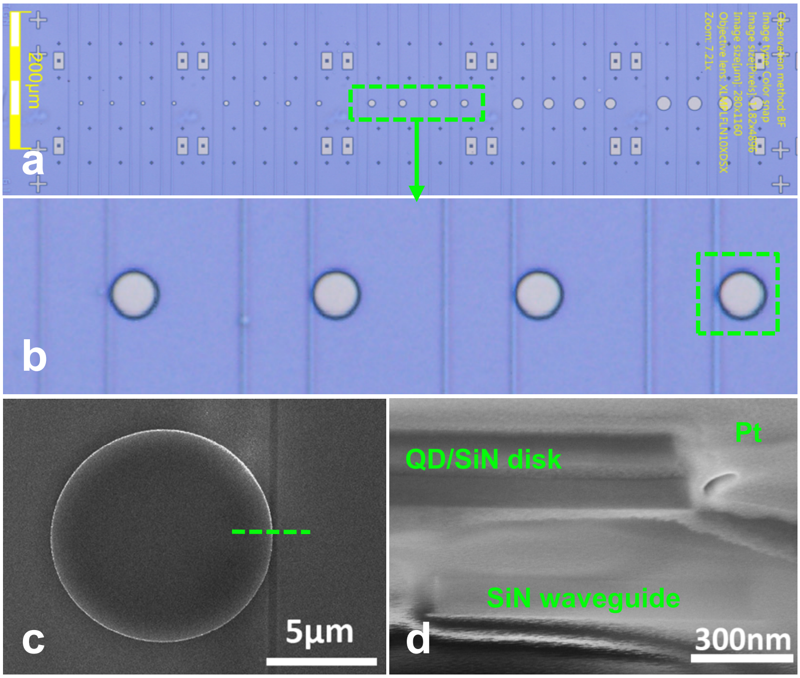

**Figure 5.11:** Optical microscope images and SEM images of a fabricated device. (a) Optical photography of an array of disks with diameters from 5 to 20 µm. (b) Enlarged view of 10 µm diameter disk array. (c) SEM image of a selected disk in (b) denoted by the dashed-green box. (d) FIB cross-sectional image of the waveguide-disk coupling region in (c) indicated by the dashed line.

Figure 5.11(a) and (b) show optical photography of a large area of one fabricated chip. It is obvious that the developed CMOS-like processes are capable of chip-scale fabrication of QD-SiN hybrid devices with high yields. We also show a close-up of a selected single disk in the SEM images of Figure 5.11(c) and (d), which clearly reveal the presence of a well-defined circular boundary and the flat top of the disk as well as the controlled position of the bus waveguide buried below the disk. Again, the sidewall of the etched SiN/QD/SiN layer stack shows a continuously co-etched surface at the interfaces of the different layers, a prerequisite for high-performance WGM disk resonators.

### 5.3.3 Characterization of disk WGMs

The WGMs in the QD-SiN disk are analyzed through their PL measured on a μ-PL setup. To excite the WGMs, we pump the disk from the top using a focused Gaussian beam spot of a 400 nm CW laser. PL signals are collected from the cleaved waveguide facet either with an optical fiber or using an objective and analyzed by a spectrometer. In this way, we can study the WGM properties such as resonance wavelength, polarization, FSR, and Q factors, which are important parameters for further analysis and understanding of the lasing operation. We characterized a set of disks with different diameters coupled to a ~500 nm wide bus waveguide, offset with respect to the disk edge by about +200 nm. Under these parameters, according to simulation the disk Q factor associated to waveguide-coupling loss is around $(3\text{-}6)\times10^4$.

Figure 5.12 represents PL spectra of 5, 7 and 10 μm diameter disks acquired with an optical fiber together with the background emission taken from the top of an unpatterned SiN/QD/SiN region. Whereas the latter aspect is in agreements with the featureless emission characteristic of the QD band-edge recombination, the spectra coupled out through the bus waveguides clearly show the WGMs of the disks with negligible background emission, thanks to preferential coupling of the QD emission into the disk resonator modes as a result of the QD layer being sandwiched centrally between the SiN layers and efficient out-coupling through the on-chip waveguide. This feature in WGM spectrum has also been observed in Chapter 4. The center of their envelope at ≈639 nm is redshifted by 15 nm with respect to the background emission spectrum. This shift is due to reabsorption of emitted light in the QD layer, which agrees with the result in Figure 5.6.

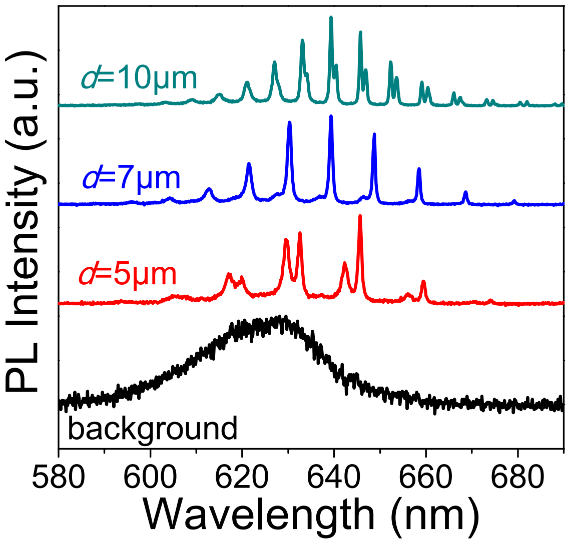

**Figure 5.12:** Measured PL spectra of disks with different diameters together with background emission, excited by a CW 400 nm laser.

Since both waveguide and disk can support them, the WGM spectra consist of a series of TE/TM modes. These mode families can be distinguished by their Q factors and FSR, with TE modes exhibiting the larger FSR and higher Q factors according to FDTD simulations. By fitting the WGM peaks to a Lorentzian function, we can extract the Q factors and FSR of these modes and classify them eventually. Moreover, a polarization analysis can offer another way of identifying TE/TM WGMs. As an example, for the disk of 10μm diameter we performed a detailed analysis of the WGMs in terms of Q factors, FSR, and polarization. In Figure 5.13 we show the whole WGM spectrum of a 10 μm diameter disk and selected modes resolved using a high-resolution (<0.05 nm) spectrometer. Using a multi-peak fit with Lorentzian functions we obtain the resonance wavelengths as well as the associated Q factors and FSR. By comparison to the simulation results in Figure 5.9, these modes are identified as the 1st order TE and 1st order TM mode families, as summarized in Figure 5.14. For analyzing the polarization of the WGM spectrum the PL signals from the bus waveguide are collected in free space using an objective and then analyzed by a polarizer. In Figure 5.15(a) we show the PL spectra versus polarizer angle. Cleary, the spectra consist of two sets of WGMs of different polarizations that are perpendicular to each other and correspond to dominantly TE and TM polarized light exiting from the waveguide. Since the TE and TM WGMs in the disk are coupled mainly to the respective TE and TM waveguide modes (according to simulations the TE-TM mode coupling is very weak), the polarization of the waveguide PL represents the WGM polarization in the disk.

Therefore, the two sets of modes can be attributed to the 1st order TE and 1st order TM WGMs of the disk, as shown in Figure 5.15(b). The polarization analysis is very useful to unambiguously identify WGM peaks when TE and TM modes accidently overlap with each other in some disks.

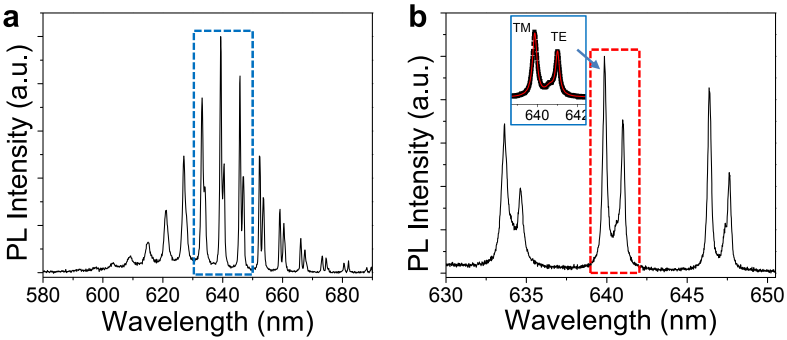

**Figure 5.13:** (a) Measured PL spectrum of a disk with 10 μm diameter. (b) The high-resolution spectrum for the selected region in (a) as indicated with the blue-dashed box. The inset shows the measured (black) and fitted (red) spectrum using a multi-peak fit with Lorentzian functions.

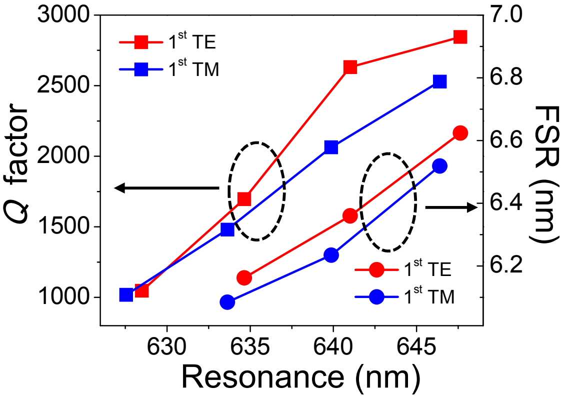

**Figure 5.14:** Extracted Q factors and FSR for several WGMs of a 10 μm-diameter disk. The 1st order TE WGMs have higher Q factors and larger FSR relative to the 1st order TM modes, in good agreement with simulated results in Figure 5.9.

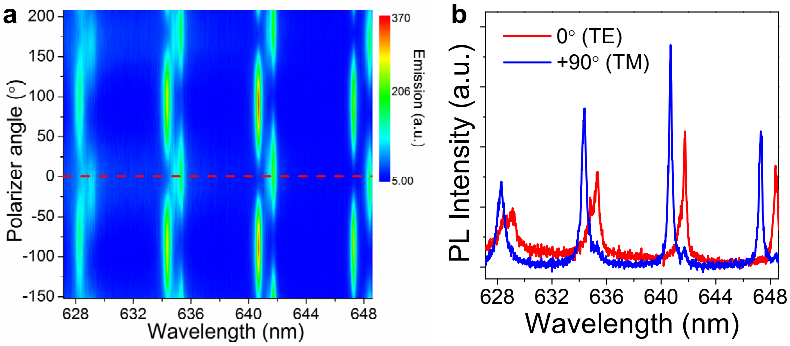

**Figure 5.15:** Polarization analysis of WGMs. (a) Plot of the PL spectra of a 10 μm-diameter disk for different polarizer angles. The red-dashed line indicates the position (0°) at which the light of horizontal polarization passes, corresponding to TE-polarized light from the waveguide. (b) PL spectra with the polarizer angle at 0° and 90°, respectively.

Finally, we extract Q factors of the 1st order TE WGMs at different resonance wavelengths for the disks with different diameters and compile the results in Figure 5.16(a). When increasing the diameter of the disk, the Q factors near the same resonance wavelength increase. For the ~630 nm resonance they saturate to ~1770 in a 15 μm-diameter disk. From the absorption measurement of the QD solution and film, we attribute this to absorption in the CdSe QD cores. This absorption starts below 650 nm and rises towards shorter wavelength. It is assumed to be negligible at longer wavelength, for example, at 660 nm where the Q factor in a 15 μm-diameter disk reaches 5800, over three times higher than that at 630 nm. The Q factors at 660 nm are mainly limited by scattering loss ($Q_{\mathrm{scat}}$) (the Q factors related to mode-radiation loss and waveguide-coupling loss as mentioned before are considerably larger) and hence, at this wavelength, we have $Q \approx Q_{\mathrm{scat}}$. On the other hand, Q factors at shorter wavelengths include two main contributions – QD absorption loss and scattering loss. In the lasing regime, the QD absorption loss is absent and the net optical gain only needs to compensate the scattering loss. Assuming Rayleigh scattering is dominant in our disk and $Q_{\mathrm{scat}}^{-1} \propto \lambda^{-4}$, we can obtain $Q_{\mathrm{scat}}$ at a given wavelength $\lambda$ as $Q_{\mathrm{scat},\lambda} = Q_{\mathrm{scat},\lambda_{660}}(\lambda/\lambda_{660})^4$, as shown in Figure 5.16(b). $Q_{\mathrm{scat}}$ can be then translated to an effective loss coefficient $\alpha_{\mathrm{scat}} = 2\pi n_{\mathrm{eff}}/\lambda Q_{\mathrm{scat}}$, where $n_{\mathrm{eff}}$ is the effective index of the lasing mode at the wavelength of $\lambda$, as plotted in Figure 5.16(b). We estimate at 630 nm the scattering loss decreases from 160 to 35 cm$^{-1}$ for a corresponding disk radius increasing from 5 to 15 μm diameter. Performance of the gain medium must be sufficient to overcome such losses if the disk is to support lasing modes. According to the measured modal gain of 100-120 cm$^{-1}$ in QD-SiN waveguide with the same thickness of QDs, lasing in QD-SiN microdisks should be feasible as the modal gain can exceed the cavity losses in the disks with diameters larger than 5 μm.

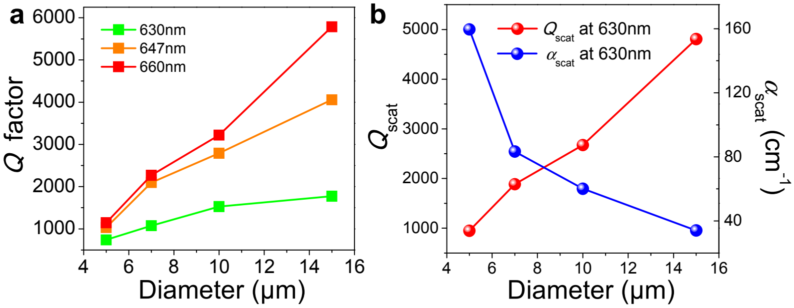

**Figure 5.16:** Q factor analysis. (a) Measured Q factors for the 1st order TE WGMs near three selected wavelengths in the disks of different diameters. (b) Extracted $Q_{\text{scat}}$ and $\alpha_{\text{scat}}$ for the 1st TE WGMs at 630 nm in different diameter disks.

## 5.4 Lasing characterization

In this section, we determine the lasing characteristics of QD-SiN microdisks in terms of threshold, emission lifetime, and temporal coherence on the same μ-PL setup[5]. We optically pump the disks with a pulsed laser at a wavelength of 400 nm provided by a frequency-doubled regenerative amplifier seeded with a mode-locked Ti:Sapphire laser, resulting in an initial pulse duration of 100 – 200 fs with a repetition rate of 1 kHz. The light is then coupled into a multi-mode optical fiber with 25 μm core diameter and 100 cm length, which stretches the pulse duration to ≈10 ps and leads to homogenization of the beam profile towards a flat top. The output facet of the pump fiber is demagnified and imaged at normal incidence onto the sample by microscope objectives, resulting in an approximately disk-shaped pump spot of 12 μm diameter. Its intensity is controlled by a movable gradient filter. For the spectroscopic detection with a high-resolution spectrograph and the time-resolved measurements with a time-correlated single-photon counting system, the emitted light is collected with a multi-mode fiber (200 μm core, numerical aperture NA=0.22) directly from the cleaved waveguide end facet. For the interferometer, streak camera and polarization-dependent measurements, the light is collected with a microscope objective (NA=0.3) from the waveguide facet. In the Michelson interferometer, the emitted light is split with a non-polarizing beam-splitter cube, controllably

---

[5] These measurements were carried out at the IBM-Zurich lab in collaboration with Thilo Stöferle, Gabriele Rainò, and Rainer F. Mahrt.

delayed in one arm by a hollow retroreflector, which is mounted on a motorized linear stage, then recombined and focused on a cooled CCD.

## 5.4.1 Laser threshold and emission lifetime

The emission spectra of a 7 μm diameter disk under different excitation conditions are represented in Figure 5.17(a) as an example result. Below the threshold ($0.89P_{\text{th}}$ – see below for a determination of $P_{\text{th}}$), the spectrum exhibits typical WGMs within the envelope of the broadband spontaneous emission of the colloidal QDs. By increasing the pump fluence above the threshold ($1.16P_{\text{th}}$), a sharp, 40-fold increase of the intensity for the WGM near 629 nm is observed. This is accompanied by line-narrowing from 0.58 nm to 0.14 nm FWHM, a distinct characteristic of the onset of lasing. Polarization analysis of the PL spectrum provides additional evidence that the lasing mode is a 1st order TE WGM, which will be discussed later. By further increasing the pump intensity to $1.8P_{\text{th}}$, a second lasing mode appears at shorter wavelength (near 620 nm), consistent with the blue-shift of the gain spectrum with increasing of pump power observed both in solution and in waveguide. The transition to lasing concurs with the emergence of scattered light of the WGMs in the PL image of the disk as seen in the insets of Figure 5.17(a). In Figure 5.17(b) we plot the total output intensity versus the pump fluence, also known as light-in-light-out (L-L) curve. The laser threshold $P_{\text{th}}$ is determined to be 27 ± 2 $\mu\text{J}\cdot\text{cm}^{-2}$. Additionally, the log-scale L-L results for two lasing modes presented in the inset in Figure 5.17(b) are well-defined S-shaped curves.

For modeling the laser emission, we employ a basic rate equation analysis for microcavity lasers [29-31]. As the duration of the pump pulse is significantly longer than the build-up time of the lasing emission, a simplistic single-mode model with static pump rate can capture the main emission intensity characteristics. The lasing photon intensity $S$ as a function of the pump rate $P$ is given by a static solution and can be expressed by

$$S = \frac{1}{2}\left[U + \left(V^2 + \frac{4\xi(\beta-1)P}{A\tau_s} + \frac{4\xi(1-\xi)}{A\tau_s}\right)^{1/2}\right], \qquad (5.1)$$

with

$$U = P - 1 - \left(\frac{1}{A\tau_s} - 1\right)\xi, \qquad (5.2)$$

$$V = U + \frac{2\xi}{A\tau_s}, \qquad (5.3)$$

where $(1 - \xi)$ denotes the fraction of the spontaneous emission lost from the open cavity, $A$ is the free-space spontaneous emission rate, $\tau_s$ is the exciton lifetime, and $\beta$ is the fraction of the spontaneous emission coupled into the lasing mode. We can neglect non-radiative recombination processes given the extremely fast stimulated emission, and hence, set $A\tau_s=1$, i.e. consider only radiative decay. For our disk, we calculate the transversal open-cavity losses $(1 - \xi) \sim 0.9$. We obtained the experimental L-L curve for a certain lasing mode by recording the output intensity $I$ as a function of pump fluence $p$, as shown in Figure 5.17(b). To fit the measured curve, we use the form $I(p) = a_3[S(a_1p) + a_2p]$, where $a_1$ is the linear scaling factor relating the excitation rate to the actual pump fluence, $a_2p$ represents the background signal which is approximately proportional to the pump flux, and $1/a_3$ is the linear factor scaling the output intensity to the detected counts in the spectrometer. Thus, $a_{i=1,2,3}$ and $\beta$ are obtained by fitting the measured data. The fit matches the measured data well as shown in Figure 5.17(b), and we find $\beta \sim 3\times10^{-3}$.

Stimulated emission is expected to shorten the luminescence decay time. We therefore performed time-resolved PL measurements, and Figure 5.17(c) shows the PL decay traces for different pump fluences. The extracted lifetimes dramatically decrease from a few nanoseconds below $P_{\mathrm{th}}$ to tens of picoseconds above $P_{\mathrm{th}}$, which is a value limited by the time resolution of the photon counter. Using a streak camera to precisely record the temporally and spectrally resolved dynamics, we find that the emission from the 7 μm disk lasts for about 7 ps and 11 ps (FWHM) for the short and long wavelength modes, respectively, see Figure 5.17(d).

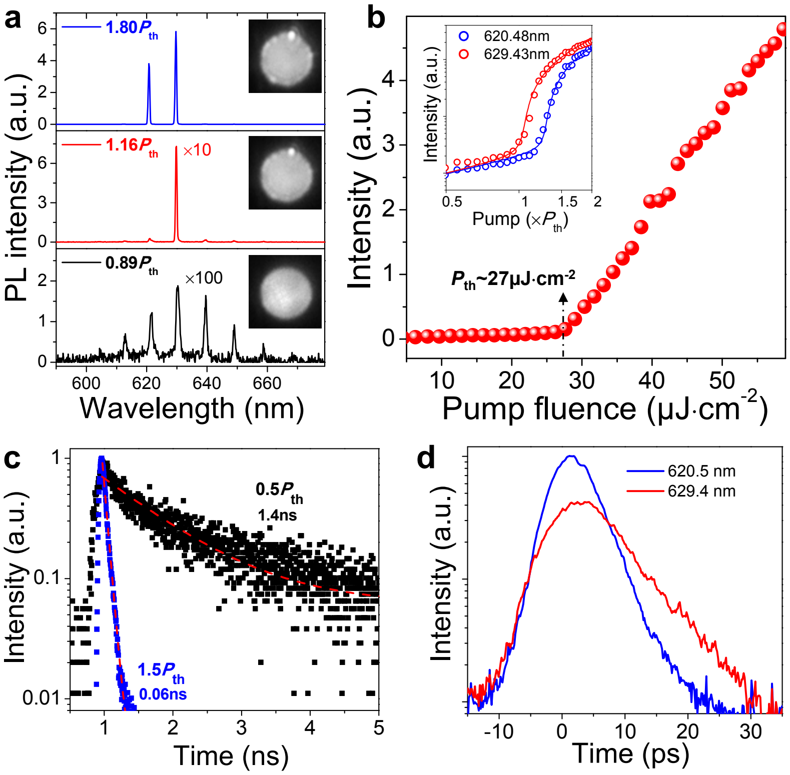

**Figure 5.17:** Laser threshold and lifetime characteristics. (a) PL spectra of a 7 μm diameter disk under different pump fluences below and above the threshold $P_{th}$. Insets: Corresponding camera-recorded PL images of the disk (intensity normalized), showing the emergence of scattering from the WGMs above the threshold. (b) Measured total PL intensity as a function of pump fluence, showing a clear threshold of 27 μJ·cm$^{-2}$. Inset: Log-scale L-L curves for two lasing modes. Symbols are measured data and solid lines are S-shaped curves obtained by a rate equation fit. (c) Spectrally integrated decay traces at different pump fluences, together with extracted lifetimes from fitting a single-exponential-decay function as indicated by the red-dashed line. d, Temporal behavior of the two lasing WGMs at pump fluence of ≈3$P_{th}$.

For the smallest disk with diameter of 5 μm, we didn't observe the occurrence of lasing, indicating its cavity loss exceeds the optical gain. All larger disks show lasing action. In Figure 5.18, we show the laser threshold and lifetime characteristics for a 10 μm diameter disk. Given its higher Q factor, the laser threshold $P_{th}$ = 21±3 μJ·cm$^{-2}$ is even lower for this disk. As seen in Figures 5.18(a) and (b), this larger disk exhibits multi-mode lasing directly above threshold and when increasing the pump power new lasing modes appear at shorter wavelength, consistent with the blue-shift of the gain spectrum. Similarly as for the 7 μm disk, the lifetime of the emission decreases from a few nanoseconds below $P_{\mathrm{th}}$ to a few picoseconds above $P_{\mathrm{th}}$ (about 6 ps to 12 ps FWHM for the short and long wavelength modes respectively), as shown in Figure 5.18(c) and (d).

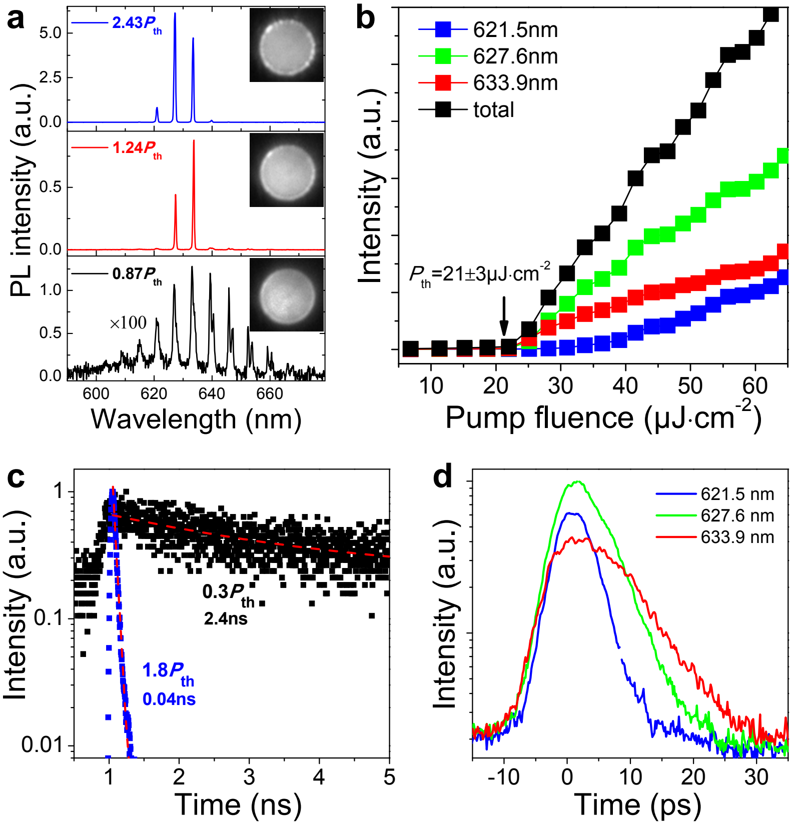

**Figure 5.18:** Laser threshold and lifetime characteristics. (a) PL spectra of a 10 μm diameter disk under different pump fluences below and above the threshold $P_{\mathrm{th}}$ = 21±3 μJ·cm$^{-2}$. Insets: Corresponding camera-recorded PL images of the disk (intensity normalized), showing the emergence of scattering from the WGMs above the threshold. (b) Measured PL intensity as a function of pump fluence for the integrated laser power (black) and for the individual laser modes (colors). (c) Spectrally integrated decay traces at different pump fluences, together with extracted lifetimes from fitting a single-exponential-decay function as indicated by the red-dashed line. (d) Temporal behavior of the three lasing WGMs at pump fluence of ~3$P_{\mathrm{th}}$, recorded by high-resolution streak camera.

To confirm which WGM is lasing in the disks, we carry out the same polarization analysis for the lasing spectrum as we did for the CW-pumped spectrum. In Figure 5.19, we show the spectra for the disks of 7 and 10 μm diameter pumped above lasing threshold. Clearly, each spectrum comprises a mode family mainly emitting in TE polarization and therefore can be ascribed to the 1st order TE WGMs. This can be understood by the fact that the fundamental TE WGMs have both the highest Q factor and largest optical confinement.

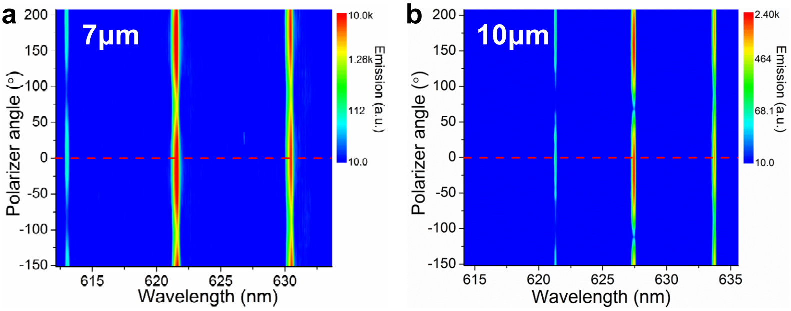

**Figure 5.19:** Polarization analysis of lasing WGMs. Plot of the lasing spectra above the lasing threshold (color scale is logarithmic) at different polarizer angles, for disks with diameters of 7 μm in a and 10 μm in b. The red-dashed line indicates the orientation of the TE polarization.

### 5.4.2 Temporal coherence of laser beam

A key signature of lasing is high and extended coherence of the emitted photons. The degree of temporal coherence of the laser light is characterized by the first order correlation $g^{(1)}(\tau)$. By sending the light emitted from the waveguide end facets through a Michelson interferometer, we determine $g^{(1)}(\tau)$ from the interference fringe visibility $\gamma = \left|g^{(1)}(\tau)\right|$, where $\tau$ is now the time delay between two interferometer arms.

We measure the interference pattern below and above threshold, and the results are reported in Figure 5.20 for a 7 μm diameter disk. Below the lasing threshold, the envelope of the visibility can be appropriately fitted with a single exponential decay, resulting in a 1/*e* coherence time of $\tau_c$= 0.33 ps. This very short coherence time equals the photon lifetime in the micro-resonator that can be calculated by $\tau_c$= $Q/\omega$, using the measured $Q$ of ≈1000 at 630 nm in 7 μm diameter disks. Above the lasing threshold, the coherence extends almost one order of magnitude to $\tau_c$ = 2.5 ps. This nearly equals the measured duration of the emitted laser pulse, but is slightly reduced due to a small temporal emission wavelength chirp from transients in the charge carrier density caused by the pulsed excitation scheme. The fringe pattern extends over the whole waveguide facet, see inset in Figure 5.20(b), as the single-transversal-mode design leads to perfect spatial coherence. A common feature both below and above threshold is that the multi-longitudinal-mode emission gives rise to a beat note where the peculiar ultrafast THz oscillation frequency corresponds to the frequency difference between the cavity modes, see inset in Figure 5.20(b). The almost Fourier-limited coherence, also in the multi-mode regime without noticeable mode competition, highlights the quality of the integrated QDs as excellent gain material.

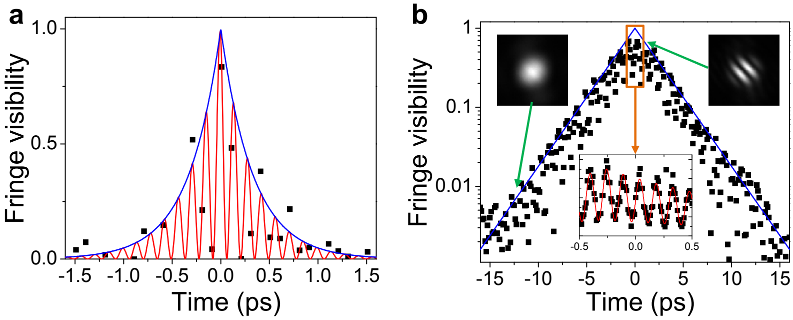

**Figure 5.20:** Temporal coherence of laser beam. (a) Visibility of the interference fringes in a Michelson interferometer obtained below the lasing threshold ($0.25P_{\text{th}}$) as a function of delay time $\tau$ between the interferometer arms. The black symbols represent the measured data, the blue line shows a fitted envelope exp $(-|\tau|/\tau_c)$ with $\tau_c = 0.33$ ps and the red curve shows a fit taking into account the beating pattern of the two emitting cavity modes (see bottom inset of (b)). (b) Above threshold ($2.75P_{\text{th}}$), the first order coherence lasts almost an order of magnitude longer, and a fit to the envelope yields $\tau_c = 2.5$ ps (blue line). The top insets show exemplary interferograms of the emission from the waveguide end facet. The spread of the measured black data points is not noise but a consequence of the beating effect of multiple lasing modes, which is resolved when measuring with very high time resolution (bottom inset). The sine fit (red line) of the time-resolved beating pattern finds a period of 0.147 ps, corresponding to the inverse frequency mode spacing of the two lasing modes.

The QD-SiN disk lasers preserve their properties over many weeks of measurements without significant degradation, wavelength drift or stability issues. This long-term stability is largely attributed to the efficient encapsulation of the colloidal QDs by the SiN matrix. Furthermore, the fabrication process is highly reproducible, allowing for a high device yield (>90%) while the operating wavelength has a variability of less than one nanometer for nominally identical devices.

## 5.5 Conclusion

We have created a versatile technology that enables hybrid integration of a whole class of solution-processable QDs with the SiN photonics platform. The quantitative analysis of the cavity and gain material allows for precise modeling and forecast of the actual device performance thanks to the stable fabrication process. Our device is the first waveguide-coupled colloidal QD laser and operates with an extremely low optical pump threshold of $P_{\mathrm{th}}$= 27 μJ·cm$^{-2}$ in only 7 μm diameter disk at room temperature. We show a comprehensive characterization covering spectroscopic, temporal and coherence properties of these ultra-compact lasers. These results constitute a clear demonstration that wavelength-tunable, colloidal QDs can pave the way not only for versatile, active SiN photonics for lab-on-a-chip, optofluidics, and sensing technologies, but also for on-chip cavity quantum electrodynamics and quantum optics based on QD emitters.

The achieved device stability together with excellent device-to-device and chip-to-chip reproducibility is critically important for high-volume fabrication and integration in practical applications. In future devices we expect that the threshold could be lowered even more by switching from a top-pump to a waveguide-coupled pump, which would allow for extremely efficient, fully-integrated excitation schemes [18]. Furthermore, the gain coefficient of QDs as well as the performance of the device can be improved by a further optimization of the core/shell QDs such as surface-passivation engineering [21]. All these benefits can be easily incorporated in our SiN photonics and hence micro- or even CW-pumped QD-SiN lasers are reasonably reachable yet needs to be demonstrated in near future.

Lastly, the current technology platform can be potentially applied to the whole class of solution-processable nanoscale materials and thereby a variety of studies and applications will be foreseen by bridging the wet-chemical material science and nanophotonics technology.

# References

[1] V. I. Klimov, A. A. Mikhailovsky, S. Xu, A. Malko, J. A. Hollingsworth, C. A. Leatherdale, H. J. Eisler, and M. G. Bawendi, “Optical gain and stimulated emission in nanocrystal quantum dots,” Science **290**(5490), 314-317 (2000).

[2] R. D. Schaller, M. A. Petruska, and V. I. Klimov, “Tunable near-infrared optical gain and amplified spontaneous emission using PbSe nanocrystals,” J. Phys. Chem. B **107**(50), 13765-13768 (2003).

[3] V. I. Klimov, S. A. Ivanov, J. Nanda, M. Achermann, I. Bezel, J. A. McGuire, and A. Piryatinski, “Single-exciton optical gain in semiconductor nanocrystals,” Nature **447**(7143), 441-446 (2007).

[4] I. Moreels, G. Raino, R. Gomes, Z. Hens, T. Stoferle, and R. F. Mahrt, “Nearly Temperature-Independent Threshold for Amplified Spontaneous Emission in Colloidal CdSe/CdS Quantum Dot-in-Rods,” Adv. Mater. **24**(35), Op231-Op235 (2012).

[5] C. Dang, J. Lee, C. Breen, J. S. Steckel, S. Coe-Sullivan, and A. Nurmikko, “Red, green and blue lasing enabled by single-exciton gain in colloidal quantum dot films,” Nat. Nanotechnol. **7**(5), 335-339 (2012).

[6] B. Guzelturk, Y. Kelestemur, M. Olutas, S. Delikanli, and H. V. Demir, “Amplified Spontaneous Emission and Lasing in Colloidal Nanoplatelets,” Acs Nano **8**(7), 6599-6605 (2014).

[7] J. Q. Grim, S. Christodoulou, F. Di Stasio, R. Krahne, R. Cingolani, L. Manna, and I. Moreels, “Continuous-wave biexciton lasing at room temperature using solution-processed quantum wells,” Nat. Nanotechnol. **9**(11), 891-895 (2014).

[8] C. X. She, I. Fedin, D. S. Dolzhnikov, A. Demortiere, R. D. Schaller, M. Pelton, and D. V. Talapin, “Low-Threshold Stimulated Emission Using Colloidal Quantum Wells,” Nano Lett. **14**(5), 2772-2777 (2014).

[9] C. X. She, I. Fedin, D. S. Dolzhnikov, P. D. Dahlberg, G. S. Engel, R. D. Schaller, and D. V. Talapin, “Red, Yellow, Green, and Blue Amplified Spontaneous Emission and Lasing Using Colloidal CdSe Nanoplatelets,” Acs Nano **9**(10), 9475-9485 (2015).

[10] Y. Wang, V. D. Ta, Y. Gao, T. C. He, R. Chen, E. Mutlugun, H. V. Demir, and H. D. Sun, “Stimulated Emission and Lasing from CdSe/CdS/ZnS Core-Multi-Shell Quantum Dots by Simultaneous Three-Photon Absorption,” Adv. Mater. **26**(18), 2954-2961 (2014).

[11] Y. S. Park, W. K. Bae, T. Baker, J. Lim, and V. I. Klimov, “Effect of Auger Recombination on Lasing in Heterostructured Quantum Dots with Engineered Core/Shell Interfaces,” Nano Lett. **15**(11), 7319-7328 (2015).

[12] B. Guzelturk, Y. Kelestemur, K. Gungor, A. Yeltik, M. Z. Akgul, Y. Wang, R. Chen, C. Dang, H. D. Sun, and H. V. Demir, “Stable and Low-Threshold Optical Gain in CdSe/CdS Quantum Dots: An All-Colloidal Frequency Up-Converted Laser,” Adv. Mater. **27**(17), 2741-2746 (2015).

[13] H. J. Eisler, V. C. Sundar, M. G. Bawendi, M. Walsh, H. I. Smith, and V. Klimov, “Color-selective semiconductor nanocrystal laser,” Appl. Phys. Lett. **80**(24), 4614-4616 (2002).

[14] A. V. Malko, A. A. Mikhailovsky, M. A. Petruska, J. A. Hollingsworth, H. Htoon, M. G. Bawendi, and V. I. Klimov, “From amplified spontaneous emission to microring lasing using nanocrystal quantum dot solids,” Appl. Phys. Lett. **81**(7), 1303-1305 (2002).

[15] M. Kazes, D. Y. Lewis, Y. Ebenstein, T. Mokari, and U. Banin, “Lasing from semiconductor quantum rods in a cylindrical microcavity,” Adv. Mater. **14**(4), 317-321 (2002).

[16] S. I. Shopova, G. Farca, A. T. Rosenberger, W. M. S. Wickramanayake, and N. A. Kotov, “Microsphere whispering-gallery-mode laser using HgTe quantum dots,” Appl. Phys. Lett. **85**(25), 6101-6103 (2004).

[17] P. T. Snee, Y. H. Chan, D. G. Nocera, and M. G. Bawendi, “Whispering-gallery-mode lasing from a semiconductor nanocrystal/microsphere resonator composite,” Adv. Mater. **17**(9), 1131-1136 (2005).

[18] B. Min, S. Kim, K. Okamoto, L. Yang, A. Scherer, H. Atwater, and K. Vahala, “Ultralow threshold on-chip microcavity nanocrystal quantum dot lasers,” Appl. Phys. Lett. **89**(19), 191124 (2006).

[19] J. Schafer, J. P. Mondia, R. Sharma, Z. H. Lu, A. S. Susha, A. L. Rogach, and L. J. Wang, “Quantum dot microdrop laser,” Nano Lett. **8**(6), 1709-1712 (2008).

[20] C. Grivas, C. Y. Li, P. Andreakou, P. F. Wang, M. Ding, G. Brambilla, L. Manna, and P. Lagoudakis, “Single-mode tunable laser emission in the single-exciton regime from colloidal nanocrystals,” Nature Communications **4** (2013).

[21] M. M. Adachi, F. J. Fan, D. P. Sellan, S. Hoogland, O. Voznyy, A. J. Houtepen, K. D. Parrish, P. Kanjanaboos, J. A. Malen, and E. H. Sargent, “Microsecond-sustained lasing from colloidal quantum dot solids,” Nature Communications **6** (2015).

[22] Y. Wang, K. E. Fong, S. C. Yang, V. D. Ta, Y. Gao, Z. Wang, V. Nalla, H. V. Demir, and H. D. Sun, “Unraveling the ultralow threshold stimulated emission from CdZnS/ZnS quantum dot and enabling high-Q microlasers,” Laser Photonics Rev. **9**(5), 507-516 (2015).

[23] M. Cirillo, T. Aubert, R. Gomes, R. Van Deun, P. Emplit, A. Biermann, H. Lange, C. Thomsen, E. Brainis, and Z. Hens, “"Flash" Synthesis of CdSe/CdS Core-Shell Quantum Dots,” Chem. Mater. **26**(2), 1154-1160 (2014).

[24] L. Carbone, C. Nobile, M. De Giorgi, F. D. Sala, G. Morello, P. Pompa, M. Hytch, E. Snoeck, A. Fiore, I. R. Franchini, M. Nadasan, A. F. Silvestre, L. Chiodo, S. Kudera, R. Cingolani, R. Krahne, and L. Manna, “Synthesis and micrometer-scale assembly of colloidal CdSe/CdS nanorods prepared by a seeded growth approach,” Nano Lett. **7**(10), 2942-2950 (2007).

[25] G. E. Cragg and A. L. Efros, “Suppression of Auger Processes in Confined Structures,” Nano Lett. **10**(1), 313-317 (2010).

[26] Y. S. Park, W. K. Bae, L. A. Padilha, J. M. Pietryga, and V. I. Klimov, “Effect of the Core/Shell Interface on Auger Recombination Evaluated by Single-Quantum-Dot Spectroscopy,” Nano Lett. **14**(2), 396-402 (2014).

[27] A. S. Ferlauto, G. M. Ferreira, J. M. Pearce, C. R. Wronski, R. W. Collins, X. M. Deng, and G. Ganguly, “Analytical model for the optical functions of amorphous semiconductors from the near-infrared to ultraviolet: Applications in thin film photovoltaics,” J. Appl. Phys. **92**(5), 2424-2436 (2002).

[28] K. Shaklee, R. Nahory, and R. Leheny, “Optical gain in semiconductors,” J. Lumin. **7**, 284-309 (1973).

[29] H. Yokoyama and S. D. Brorson, “Rate-Equation Analysis of Microcavity Lasers,” J. Appl. Phys. **66**(10), 4801-4805 (1989).

[30] K. A. Shore and M. Ogura, “Threshold Characteristics of Microcavity Semiconductor-Lasers,” Opt. Quantum Electron. **24**(2), S209-S213 (1992).

[31] T. Stöferle, N. Moll, T. Wahlbrink, J. Bolten, T. Mollenhauer, U. Scherf, and R. F. Mahrt, “Ultracompact Silicon/Polymer Laser with an Absorption-Insensitive Nanophotonic Resonator,” Nano Lett. **10**(9), 3675-3678 (2010).

# 6

# Conclusions and perspectives

## 6.1 Conclusions

In this thesis, we have focused on two parts − development of passive SiN photonic integrated circuits based on a plasma-enhanced chemical vapor deposition (PECVD) process and demonstration of integrated light sources on it by means of hybrid integration with colloidal quantum dots (QDs).

First, we developed a Lab-based SiN integrated photonics platform using processing steps compatible with those used in the nano-electronics industry. By thoroughly optimizing the fabrication processes, including optical contact lithography, planarization, and in particular the dry etching of SiN, we achieved low-loss waveguides of ~1 dB/cm for wavelengths ranging from 600 nm to 1360 nm in PECVD SiN deposited at relatively low-temperatures ranging from 120 °C to 270 °C. Thanks to a high-resolution contact lithography process capable of defining feature sizes down to 400 nm, single-mode waveguides with losses of 2~3 dB/cm were also demonstrated. On the basis of this platform, we further designed and realized vertically waveguide-coupled free-standing SiN microdisks. High quality (Q) factors ($2.5\times10^5$ at 1310 nm) and large finesses (2300 at 1310 nm) were achieved in these compact on-chip microresonators from the visible to telecom wavelengths, representing the state-of-the-art in integrated PECVD SiN resonators. Moreover, we demonstrated that our design scheme and fabrication technology for integrated free-standing SiN disks can be extended to films deposited by low-pressure chemical vapor deposition (LPCVD), thus potentially allowing for the realization of ultra-high-Q, ultra-high-finesse, and low-mode-volume integrated SiN microresonators operating over an even broader spectral range. The current processing techniques for SiN will certainly provide valuable and universal guidance for future development of SiN-based photonics. The demonstrated high-performance SiN-photonics building blocks can be readily used in practical applications such as optical interconnect, nonlinear optics, optomechanics, and on-chip optical sensing. The developed technologies also form the base for later development of active SiN devices with combination of QDs.

Before developing QD-SiN integrated devices, we demonstrated a patterning technique for solution-based QDs deposited on a planar substrate. Using high quality Langmuir–Blodgett deposition and a unique lift-off process, we experimentally demonstrated both nanoscale and single-dot patterning of colloidal QD-films. Feature sizes down to ~30 nm for a continuously uniform film of QDs and a yield up to 40% for single-QD positioning have been obtained. Furthermore, a theoretical model was proposed to describe the experimental processes. The good agreement between the experiment and the numerical model has revealed that the deposition behavior of QDs onto a substrate and the experimental distribution of QD counts can be described by a binomial distribution, providing valuable guidance in the realization of single-QD patterns with an expected yield. The presently developed patterning technology for QDs provides an efficient tool both for the fundamental study of the properties of stand-alone QDs and for the quantitative investigation of the interaction between QDs and their environment such as on-chip photonic or electronic devices. In particular, in our own case, this technique is carried out in an ongoing effort to realize single-QD emitters whereby a single QD can be localized in photonic components such as waveguides or cavities for exploring on-chip single-photon emission. Also, in the future we may employ this technique for integrating few or single QDs in optical resonators and studying lasing in such devices where both the QD number and position needs to be precisely controlled for deterministic optical coupling.

Furthermore, we have created a versatile technology that enables hybrid integration of a whole class of solution-processable QDs with the SiN photonics platform and demonstrated low-loss QD-SiN waveguides with the preservation of QD emission. On the basis of this platform and previous fabricating technology, we further designed and fabricated free-standing SiN microdisks integrated with embedded colloidal QDs, with those disks coupled to an on-chip access waveguide in a vertical coupling scheme. The detailed characterization of the fabricated devices revealed both high performance – high Q factors together with large free spectral ranges – and an efficient coupling of QD emission to disk resonant modes and eventually to the on-chip waveguide.

Relying on all the previous achievements, we then aimed to demonstrate on-chip QD-SiN microlasers. First, we studied the optical gain of QDs embedded in a SiN waveguide and obtained a net modal gain of more than 100 $cm^{-1}$ in (100/55/100 nm) SiN/QD/SiN layer stack. The same layer stack was then used to fabricate microdisks coupled to bus waveguides and a quantitative analysis of the disk modes indicated the possibility of lasing with the measured optical gain. Indeed, lasing action has been observed in these disks pumped with picosecond laser pulses at room temperature, revealing an extremely low optical pump threshold of 27 μJ·cm$^{-2}$ in a 7 μm diameter disk. We showed a comprehensive characterization covering spectroscopic, temporal and coherence properties of these ultra-compact microlasers. These results constitute a clear demonstration that wavelength-tunable, colloidal QDs can pave the way not only for versatile, active SiN photonics for lab-on-a-chip, optofluidics, and sensing technologies, but also for on-chip cavity quantum electrodynamics and quantum optics based on QD emitters. The achieved device stability together with excellent device-to-device and chip-to-chip reproducibility is critically important for high-volume fabrication and integration in practical applications. In future devices we expect that the threshold could be lowered even more by switching from a top-pump to a waveguide-coupled pump, which would allow for extremely efficient, fully-integrated excitation schemes. Furthermore, the gain coefficient of QDs as well as the performance of the device can be improved by a further optimization of the core/shell QDs. All these benefits can be easily incorporated in our SiN platform and hence it seems realistic QD-SiN lasers pumped with microsecond pulses or even continuous-wave (CW) are reachable in the near future.

## 6.2 Perspectives

In SiN photonics, there still remains room to improve in terms of waveguide losses and resonator Q factors. One path for exploration could be on the material loss of PECVD SiN film at 1550 nm. In this respect, deposition conditions and post-treatment of SiN may play important roles in reducing the intrinsic absorption at around 1550 nm. As an example recently $NH_3$-free processes with reduced loss have been demonstrated. On the other hand, LPCVD SiN can be employed, in particular, by using current technologies for the realization of ultra-high-Q waveguide-coupled free-standing SiN microresonators which will be of great interest in nonlinear optics and optomechanics that can be fully integrated on chip thereby allowing in depth of these effects in a stable environment.

For QD-SiN lasers, one of significant steps is to realize CW pumped lasers. Now we demonstrated picosecond pulse excitation and nano- or microsecond pulse pump on the present devices can be carried out to examine lasing action and calculate the threshold in power density. Furthermore, CW pumping could be tried, perhaps with implementing an improved cooling scheme for the dissipation of excess heat generated by pumping. Other approaches for reaching the CW pumping regime are further optimizing fabrication quality and improving gain performance of the QDs. For example, we can localize a perfect layer of QDs entirely encapsulated in a SiN microdisk or photonic crystal cavity using our patterning technology. In that case no etching through the QD-layer is needed which is expected to result in QD-SiN cavities with higher Q factors as well as lower thresholds. In the same way, devices with a few or even a single QD can be realized and lasing under such extreme circumstance could be investigated. Moreover, quantum emitting properties such as single-photon emission can be explored for realization of on-chip single-photon sources based on QDs.

Extending the laser wavelength from visible to infrared wavelengths is another goal for the QD-SiN platform. This study can be carried out with the current device design by using infrared emitting QDs such as colloidal PbS and HgTe. More generally, our hybrid integration technology can be applied to a variety of nanoscale materials that emerged in recent years for development of not only optical but also electrical devices on the SiN photonics platform, which will offer more prospects of high scientific and technological interest.